ANALYSIS AND OPTIMIZATION OF CRYSTALLINE SILICON WAFER BASED PHOTOVOLTAIC MODULES

GUO SIYU
(B.Sc., Southeast University, Nanjing, China)

A THESIS SUBMITTED

FOR THE DEGREE OF DOCTOR OF PHILOSOPHY

DEPARTMENT OF ELECTRICAL AND COMPUTER ENGINEERING

NATIONAL UNIVERSITY OF SINGAPORE

2015

DECLARATION

I hereby declare that the thesis is my original work and it has been written by me in its entirety. I have duly acknowledged all the sources of information which have been used in this thesis.

The thesis has also not been submitted for any degree in any university previously.

GUO Siyu

11 December 2015

Acknowledgement

Firstly, I would like to thank my supervisor Prof. Armin Gerhard Aberle for giving me the opportunity to pursue my PhD in the Solar Energy Research Institute of Singapore at NUS. I am grateful to him for his guidance, help and feedback on my research and publications. I would like to thank my co-supervisor Dr. Ian Marius Peters for his daily supervision and advice. Marius was a really good mentor to me and helped me grow step by step in my research area. I would like to thank my co-supervisor Dr. Timothy Michael Walsh for inspiring me with innovative ideas. I am indebted to him for all the discussions and advices on my research works.

I would like to thank my thesis advisory committee members Prof. Ganesh Samudra and A/Prof. Aaron Danner for giving me feedback and suggestions during my qualification exams.

I would like to thank Dr. Johnson Wong and Dr. Rolf Stangl for all the advice and help on my research works. I also would like to thank my colleagues Dr. Jai Prakash Singh and Dr. Jiaying Ye for exchanging ideas and helping me with the experimental works.

I would like to thank my friends Cangming Ke, Zhe Liu, Puqun Wang, Mengjie Li, Haohui Liu, Fajun Ma and all the other members of the SERIS Simulation Team for their help, having dinners together, and for exchanging ideas with me. I would also like to thank all SERIS colleagues who have given me some help. Without them, this journey would have been much harder.

I would like to thank NUS and its ECE Department for offering me the opportunity to pursue my PhD degree.

Last but not least, I would like to thank my parents for their endless love and support on my work and life. I would like to thank my husband Mr. Daming Xu for his unconditional love, understanding and encouragement over the past eight years.

Table of Contents

Summary

Nowadays, crystalline silicon (c-Si) wafer-based photovoltaic (PV) products have widespread applications, as evidenced by their dominant market share in the whole PV market. As a result, extensive efforts have been devoted to improve the c-Si solar cell efficiency. Meanwhile, the development of the PV module technology is equally significant, as the PV module-related issues are crucial to the final conversion efficiency of solar energy. In this thesis, both simulation and experimental methods are used to investigate various problems related to c-Si wafer based PV modules.

Firstly, the CTM resistive losses are analysed. CTM resistive loss, which is mainly caused by current transport through the ribbons, is compared between PV modules using full-size or halved cells, as well as modules using monofacial or bifacial solar cells. It is found that the cell metallization pattern has a strong influence on the cell interconnection resistive loss, and established calculation methods are improved according to this effect. Furthermore, a detailed quantitative analysis is done for PV modules using monofacial and bifacial halved cells, using both simulation and experimental methods.

Besides a resistive loss analysis, an optical analysis is also performed. The optical analysis focuses on the influence of the backsheet in the cell-gap region and other inactive areas of the PV module on its short-circuit current. Both simulations and experiments prove that the short-circuit current increase when going from full-cell PV modules to halved-cell PV modules is around 3% in the studied case. Furthermore, the analysis is extended to other inactive areas of a PV module and a full area-related loss analysis is achieved.

Besides PV module analysis under standard test conditions (STC), PV module behaviour under other operating conditions is also analysed, including partial shading condition, spectral response (SR) measurement condition and real environmental

condition. In the first step, the mismatch effect caused by partial shading is investigated by circuit modelling. It is found that the bypass diode configuration has a strong influence on the PV module power output considering the movement of the shadow. Based on real (i.e., measured) irradiance data, the bypass diode configuration causes a 20% difference in the PV module energy yield when regular inter-row shading happens. In the next step, the influence of spectral response (SR) mismatch of individual cells on the SR of the PV modules is investigated. It is concluded that the operating current of a PV module is not necessarily limited by the cell having the lowest current, but depends on the light intensity and the shunt resistance of the individual cells.

Moreover, PV module performance is also evaluated based on real (i.e., measured) irradiance data and environmental conditions. In the last study, a global comparison is made between conventionally mounted monofacial modules and vertically mounted bifacial modules. It is found that the difference on the energy yield for the two module configurations depend on three factors: geographic location, diffuse fraction and albedo.

List of Tables

List of Figures

List of symbols and abbreviations

PV	Photovoltaics
CTM	Cell-to-module
SR	Spectral response
EQE	External quantum efficiency
STC	Standard test condition
SCR	Space charge region
I-V	Current-voltage
AM	Air mass
DOY	Day of a year
DNI	Direct normal irradiance
EVA	Ethylene vinyl acetate
LBIC	Light beam induced current
CMMM	Conventionally mounted monofacial module
VMBM	Vertically mounted bifacial module
FEM	Finite element method
a	Absorption coefficient
E_{fn}	Quasi-Fermi level of electron
E_{fp}	Quasi-Fermi level of hole
E	Photon energy
k	Boltzmann constant
T	Temperature in Kelvin
j_r	Radiative recombination rate
j	Solar cell current density
j_{ph}	Solar cell photocurrent density
I_{ph}	Solar cell photocurrent
j_0	Reverse saturation current density
V	Solar cell voltage
R_{s}	Series resistance
R_{sh}	Shunt resistance
n	Ideality factor

q	Electronic charge (1.6×10^{-19} C)
I_{sc}	Short-circuit current
j_{sc}	Short-circuit current density
V_{oc}	Open-circuit voltage
p_{mpp}	Maximum power density
P_{mpp}	Maximum power
j_{mpp}	Current density at the maximum power point.
V_{mpp}	Voltage at the maximum power point.
p_{in}	Power density of external illumination
η	Solar cell efficiency
FF	Fill factor
I_{scM}	PV module short-circuit current
V_{ocM}	PV module open-circuit voltage
P_{mppM}	PV module maximum power
N_p	Number of strings connected in parallel
N_s	Number of cells connected in series
N	Number of cells within the PV module
I_{top}	Current flowing through the top ribbon
I_L	Current extracted at the end of the ribbon
L	Ribbon length
x	Position along the ribbon
r	Ribbon resistivity
R_r	Effective ribbon resistance of a solar cell
λ	Wavelength
h	Planck's constant
c	Light velocity
θ_z	Angle between surface normal and the incoming sunlight
I_0	Exterritorial radiation
τ	Transmission coefficient for direct solar radiation
H_{dir}	Horizontal direct radiation
H_{diff}	Horizontal diffuse radiation

k_{d}	Diffuse fraction
k_{t}	Clearness index
R_{emitter}	Emitter sheet resistance
R_{M}	Sheet resistance of fingers and busbars
ρ_{c}	Contact resistance of fingers and busbars
ρ_{r}	Ribbon resistivity
F_{pitch}	Finger pitch
W_{busbar}	Busbar width
W_{ribbon}	Ribbon width
h_{r}	Ribbon height
N_{bb}	Busbar number
P_{cell}	Radiant power reaches a solar cell
P_{total}	Total amount of radiant power received by a PV module
Inc	Relative increase in radiant power received by the solar cells
A_{cell}	Solar cell area
θ	Angle between the scattered ray direction and the surface normal (polar angle)
S_{n}	Normalized reflected radiant intensity
φ	Azimuthal angle
P_{b}	Total radiant power reflected from the backsheet area to the solar cell area
α	Critical angle
R	Backsheet reflectance
$\Phi_{\mathrm{n}}(\lambda)$	Photon flux
ΔI	Short-circuit current increase
β_{sun}	Sun altitude angle
γ	The angle between the normal of the module and the sunlight incident direction
S_{dir}	Direct-beam solar radiation received by a tilted surface
α_{d}	Difference between the sun's and the module's azimuth angles
α_{sun}	Sun azimuth angle
α_{t}	Azimuth angle of the tilted surface

S_{direct}	Direct radiation received by a tilted surface
R_{loss}	The reflection loss of the direct beam incidents to a tilted surface
svf	Sky-view-factor
gvf	Ground-view-factor
R_{ground}	Radiation reflected from the ground
S_{total}	Total radiation received by a tilted surface
A	Ground albedo
R_{mm}	Series resistance of a mini-module
R_{c}	Total series resistance of a solar cell
R_r	Series resistance of the ribbons cell
R_{rg}	Series resistance of the ribbons in the gap region
R_{rc}	Series resistance of the ribbons in the cell region
R_{m}	Effective resistance of the aluminium metal sheet
R_{Al}	Aluminium sheet resistance
$P_{\mathrm{loss\_top}}$	Power loss in the front ribbon
$P_{\mathrm{loss\_rear}}$	Power loss in the rear ribbon
$P_{\mathrm{loss-Al}}$	Power loss in the aluminium metal sheet
P_{relative}	Relative power loss reduction on ribbons
$R_{\mathrm{r-top}}$	Effective resistance of the front ribbons
$R_{\mathrm{r-rear}}$	Effective resistance of the rear ribbons
I_{n}	Normalized short-circuit current
I_{meas}	Measured LBIC current
I_{max}	Maximum LBIC current measured
F	Total percentage of the light reaches the inactive area and reflected to the active
A_{eff}	Effective percentage area
A_{p}	Actual percentage area
$\dot{A}_{\mathrm{shade}}$	Shading velocity
T^*	Shadow transmittance
P_0	PV module power output (no shading)
P_{s}	PV module power output (consider shading)

N_{shade}	Number of shaded strings
N_{total}	Total number of strings
R_{p}	Performance factor
G_{mono}^{ideal}	Solar radiation at single wavelength

1 Introduction

1.1 Crystalline silicon PV technology

Renewable energy can help solve problems caused by the continuous increasing worldwide demand of energy and the finite availability of fossil fuels. One of the most promising renewable technologies is photovoltaics (PV). Photovoltaic technology has many advantages: Its energy source, solar radiation, is available all over the world. It is environmental friendly and causes little air pollution or hazardous waste.

Among all kinds of PV products, crystalline silicon (c-Si) solar cells and modules have the largest market share [1]. Figure 1.1 shows the market share for different PV technologies in 2014 [2]. There are many obvious advantages for silicon wafer based solar cells. First, silicon is a safe and abundant material on Earth and makes up 27.7 % of the Earth's crust by mass [3]. Also, c-Si technology is a very mature technology in the microelectronic area, which offers a lot of benefits for the development of c-Si solar cells. And the development history of c-Si solar cells is also over 70 years [4]. What's more, c-Si solar cells have relatively high efficiency and low cost. On one hand, c-Si solar cell efficiency has reached 25.6 % for monocrystalline silicon and 20.4 % for multicrystalline silicon [5, 6]. Module efficiencies reached 22.9 % for mono-crystalline solar cells and 18.2 % for multicrystalline solar cells [5, 6]. The price of c-Si PV modules has dropped to levels of \$0.6/W_p in 2015 [7, 8]. The low price allows them to be widely applied in PV systems across the world. It appears that, among all existing types of solar cells, silicon wafer solar cells provide the best trade-off among efficiency, cost and lifespan, which allow them to occupy the largest market share [9].

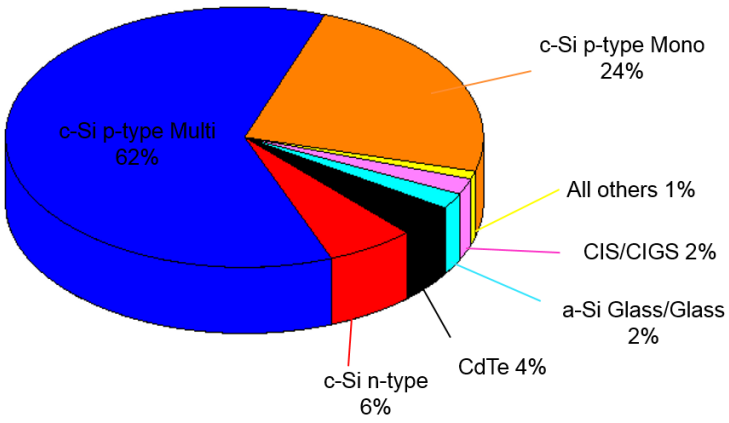

Figure 1.1: 2014 solar PV module productions by technology [2].

1.2 Development of crystalline silicon PV modules

The development of PV module technology has a 60 year history. The first silicon wafer PV module was fabricated by Bell Laboratories in 1955 [10]. The PV module efficiency was only 2%. Nowadays, the best industrial c-Si PV modules have an efficiency of over 21%. During these years, a lot of changes have happened to the PV module technology [10], for example: The cell size became larger and the batch properties become more uniform; Quasi-square crystalline wafers are applied in order to increase the cell packing density and reduce the resistive loss; low-iron glass is applied in PV modules to improve the glass transparency; EVA (ethylene vinyl acetate) is used as encapsulation material to improve the transparency of the encapsulation layer as well as the PV module durability.

Nowadays, many new PV module technologies come into the market, which help improve the PV module energy yield in different ways. For example, halved-cell PV modules have been applied by some companies like Mitsubishi [11] and Trina Solar [12]. This kind of PV module is made of half-size silicon wafer solar cells. The smaller current flowing through the ribbons strongly reduces the resistive loss. Also, the gaps between the cells in the module increase the module current via back-scattering of light. In 2014, Trina Solar reported a world-record PV module with an

output power of 335.2 W [12]. It is composed of half-size p-type monocrystalline silicon wafer solar cells with a batch efficiency of 21.4%.

Another example is the Smart Wire Connection Technology (SWCT) [13]. In order to further reduce the resistive loss and shading loss from the ribbons, SWCT has been applied in c-Si PV modules. This kind of PV module employs a foil-wire electrode instead of the conventional cell connectors (ribbons). The resulting energy yield of this PV module technology is around 3% higher than that of a conventional PV module.

Also, for building integrated PV (BIPV) applications, different PV module types appear. A good example is the bifacial PV module [14]. This kind of PV module uses bifacial c-Si wafer solar cells and applies a glass-glass construction. Thus they can make use of the sunlight coming from both sides, which makes them very good at converting the diffuse irradiance, both indoors and outdoors. Apart from making PV modules more efficient and more durable, researchers also work on beautifying them. For example, in 2015 a white PV module with an efficiency of more than 10% was developed by the CSEM institute [15]. The whole module is white, which is very attractive for BIPV applications.

1.3 Problems addressed in this thesis

Even though PV module technology has developed a lot over these years, many factors still affects their efficiency and haven't been solved. A lot of issues related to PV modules, such as mismatch effects, cell-to-module (CTM) losses, and also the installation method can have a strong influence on the PV system power generation [16]. A PV module which is composed of high-efficiency solar cells can have a relatively low efficiency if it has severe cell-to-module (CTM) losses. Figure 1.2 shows a summary of CTM losses and how they affect the PV module efficiency (reported by ISFH [17]). The different kinds of CTM losses have influence in various

degrees and the combined effects greatly influence the PV module efficiency. In today's PV market, when packaging 19% efficient c-Si solar cells into a PV module with 60 cells, the module efficiency can reduce to around 15-16.5% because of these CTM losses [18]. Also, even a high-efficiency PV module can have low energy yield if it is not installed in a suitable way. All these issues need to be considered and optimized in order to maintain the efficiency of the solar cells all the way up to the system level. Also, due to the development of new PV technologies such as bifacial solar cells and PV modules [19], it is very important for people to make choices among different kinds of PV modules and systems based on the real conditions of the PV power plant. Since these different kinds of systems have different strengths and weaknesses, it is necessary to choose the optimum system for a certain condition. As a consequence, PV module technology, which has a strong influence on the ultimate energy conversion efficiency of a PV system, is an important part in the PV area and should be investigated and improved continuously.

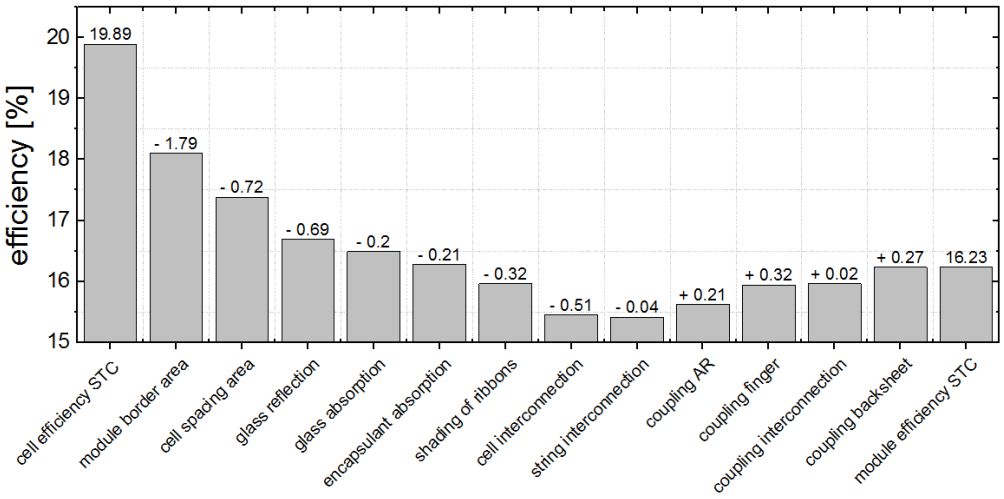

Figure 1.2: A summary of cell-to-module losses and gains and their influence on PV module efficiency cited from [17]. The influence of each loss/ gain mechanism on PV module efficiency is indicated on the top of each bar.

Thus in this thesis the author uses a set of simulations, experiments and measurements to explore and quantify different CTM losses of a c-Si PV module, to model the I-V characteristics of a c-Si PV module under different conditions, and to evaluate

the energy yield of a c-Si PV module over a long period. The CTM loss in this work refers to laboratory modules which haven't been installed in the field. Thus, the field degradation is not considered in this study. Also, rather than going into the details of each loss mechanism, the author focuses on the main factors that influence the PV module power output. For each factor, the author investigates new technologies like halved cells and bifacial PV modules in the case studies. By making comparisons with conventional PV modules, the author is able to quantify the benefits of the new technologies and make suggestions for further improvements. The following is a series of hypotheses that will be explained in this thesis:

1. Due to the two-dimensional current flow in the cell-area metal sheet, the CTM interconnection loss is different for finger-busbar "H" pattern and full-area metal

pattern, which further affects the fill factor of a c-Si PV module.

2. The cell-gap region and other inactive components of a c-Si PV module contribute significantly to the light received by solar cells, which further influences the short-circuit current of a c-Si PV module.

3. PV module bypass diode configuration greatly affects the output power when partial shading happens.

4. The spectral response (SR) of c-Si PV modules under low irradiance conditions is different from the SR under AM1.5 condition.

5. The difference of received power for monofacial and bifacial c-Si PV modules greatly depends on the installation and environmental factors. Under certain circumstances, vertically mounted bifacial PV modules receive more solar irradiance than conventionally mounted monofacial PV modules.

To address the above-mentioned problems, this thesis is structured as follows:

Chapter 1 gives the introduction of this thesis. The importance of c-Si PV technologies is emphasized and the motivations of this thesis are described.

Chapter 2 includes theories and background knowledge used in this thesis. The basic principles of c-Si solar cells and the one-diode equivalent circuit model are introduced. The basic principles of c-Si PV modules and different kinds of cell-to-module loss are described. Also, global and local irradiance conditions are introduced and the definitions of direct and diffuse radiation are given.

Chapter 3 introduces the methods used in this work, including fabrication methods, characterization methods and simulation methods. Regarding characterization methods, I-V measurement and SR measurement of c-Si PV modules are introduced. For the simulation methods, both electrical models and optical models used for c-Si PV module analysis and optimization are discussed.

In Chapters 4, 5, 6, 7 the main results of the thesis are presented. Chapter 4 and 5 focus on the investigation and optimization of c-Si PV modules under standard test conditions (STC). Chapters 6 and 7 investigate the c-Si PV module behaviour under other operating conditions.

Chapter 4 introduces a resistive loss analysis for c-Si wafer based PV modules. A rigorous method is used to compare the cell-interconnection resistive loss for PV modules using monofacial cells and bifacial c-Si cells. Based on this method, a quantitative analysis is performed for a c-Si PV module using halved cells by both simulation and experiment.

Chapter 5 focuses on optical analysis for c-Si wafer based PV modules. In this chapter, the influence of the backsheet (i.e., the cell-gap region) and other components on the short-circuit current of a c-Si wafer based PV module is investigated theoretically and experimentally.

In Chapter 6, electrical circuit modelling is used to investigate mismatch effects of c-Si PV modules. (Mismatch losses of a PV module refer to the power losses caused by the interconnection of solar cells which don't have identical properties or which experience different conditions from one another [20].) In the first part, taking the movement of the shadow into account, the c-Si PV module current-voltage (I-V) characteristics under partial shading conditions are investigated. The long-term influence of bypass diode configuration on the power output under inter-row shading condition is then studied. In the second part, the mismatch effect under spectral response conditions is investigated.

Chapter 7 mainly focuses on the outdoor analysis of c-Si PV modules with different configurations. In the analysis, a global comparison is made between conventionally mounted monofacial c-Si PV modules and vertically mounted bifacial c-Si PV modules. Factors influencing these two kinds of PV modules are investigated. Also, which kind of c-Si PV module is more suitable for a certain location is evaluated worldwide.

2 Theory and background

This chapter introduces the theories and background knowledge required in this thesis. First, the basics of silicon wafer solar cells are briefly introduced in Section 2.1. Subsequently, the one-diode model for solar cells is introduced. The one-diode model constitutes the fundamentals of circuit modelling, which are frequently used throughout this work (in Chapter 4 and Chapter 6). In Section 2.2, basic properties of c-Si wafer PV modules are introduced and the impact of solar cell interconnection on the PV module I-V characteristics is explained. Following this, the main cell-to-module loss mechanisms are categorized into resistive loss, optical loss and mismatch loss and are discussed. In Section 2.3, solar irradiance and its composition are discussed. Irradiance conditions are of great importance when estimating the power that can be harvested by a PV module in various locations.

2.1 Basics of c-Si wafer solar cells

Since c-Si solar cells are the basic units used in a c-Si PV module, in this section the theories describing silicon wafer solar cells are briefly introduced for a basic understanding of photovoltaic devices and their operating principles. Basic principles of solar cells are described in detail in the literature. Comprehensive overviews are, for example, given in [21-24].

Figure 2.1(a) shows the structure of a typical solar cell. A solar cell is usually made of semiconductor materials. Under illumination, an electron in the valence band can absorb the energy of a solar photon and be excited to the conduction band. In this way a free electron-hole pair is generated. In order to create a photovoltaic device, the generated free electrons and holes must be spatially separated [25], and this can be achieved by a p-n junction. A device with a single p-n junction is called a diode. The n-type material has a large density of free electrons, but a small hole density. Correspondingly, the p-type material has a large hole density but a small density of free

electrons. When the two types of materials are brought together, due to the diffusion of electrons from the n-type region to the p-type region and the diffusion of holes from the p-type region to the n-type region, a depletion region is formed and an electric field is set up within this region. Under thermal equilibrium condition, the Fermi levels of the two materials align and the p-n junction has one uniform Fermi-level (shown in Figure 2.1(b)). Assuming the metal forms ideal Ohmic contacts with the semiconductor, the electrons in the contact material can easily interact with the majority carriers within the semiconductor. In the n-type region, electrons can move easily across the semiconductor-metal interface. In the p-type region, electrons from the metal can also move easily to the semiconductor and recombine with the holes.

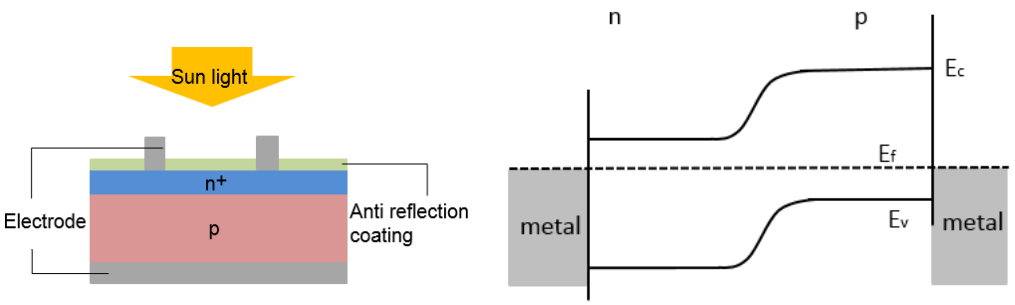

(a) (b)

Figure 2.1: (a) Structure of a p-n junction solar cell. (b) Band diagram of a p-n junction solar cell in the dark (thermal equilibrium).

Under illumination condition, the light-generated carriers change the initial distribution of electrons and holes, thus the Fermi energy splits into two Fermi energies (one for electrons and one for holes; "quasi-Fermi energies") [26]. Assuming the generation and recombination rate across the diode is uniform and there is no surface recombination, under open-circuit condition, the quasi-Fermi levels are two flat lines and have no gradient (shown in Figure 2.2). All light-generated carriers recombine internally and the open-circuit voltage between the two terminals is determined from the quasi-Fermi level splitting, as indicated in Figure 2.2.

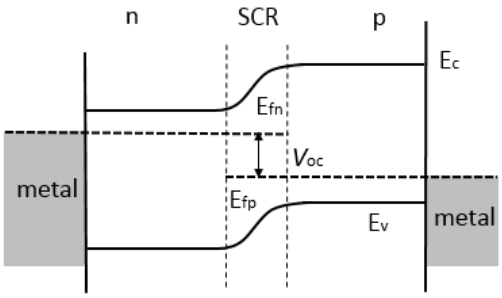

Figure 2.2: Band diagram of an illuminated p-n junction under open-circuit condition. E_{fn} and E_{fp} are the quasi-Fermi levels for electrons and holes. SCR is the space charge region of the p-n junction. This band diagram is based on the following assumptions: (1) the carrier generation and recombination rate across the diode is uniform; (2) surface recombination is not considered.

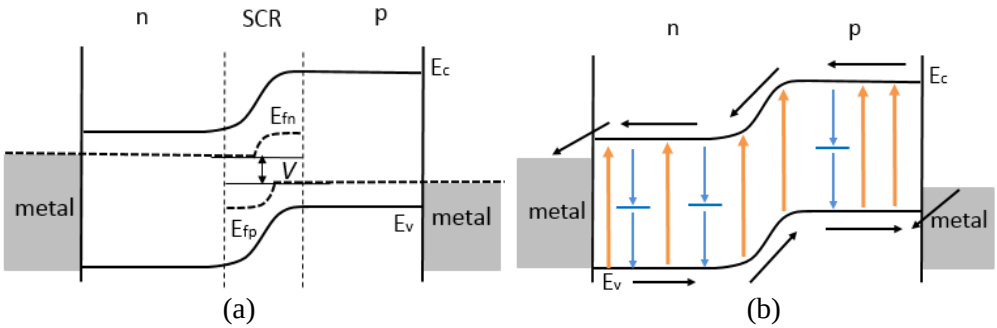

Figure 2.3: (a) Band diagram of an illuminated p-n junction under a forward bias that is less than the open-circuit voltage. (b) The corresponding free charge carrier generation (orange arrows), free charge carrier recombination (blue arrows) and electron and hole flow paths (black arrows). Diagram (a) is based on the following assumptions: (1) the carrier generation and recombination rate across the diode is uniform; (2) surface recombination is not considered.

Figure 2.3(a) shows the band diagram of the illuminated p-n junction when the operating voltage is lower than the open-circuit voltage. Under this condition, the quasi-Fermi levels for electrons and holes both have a gradient. The carriers then flow according to this gradient. The minority carriers generated within a certain distance of the p-n junction move towards, and then across, the junction and become majority carriers. Figure 2.3(b) shows the main processes involved: charge carrier generation (orange arrows), charge carrier recombination (blue arrows), and electron and hole flow paths (black arrows). In this whole process, electrons flow in the conduction band to the metal contact of the n-type region, and holes flow in the valence band to the metal contact of the p-type region. The electrons then flow from

the n-type contact through the external circuit and then return to the diode via the metal contact to the p-type region.

The optical generation process in the illuminated diode is countered by recombination mechanisms, including radiative recombination, Auger recombination and Shockley-Read-Hall recombination. Radiative recombination is the reverse of the optical e-h pair generation process, in which an electron in the conduction band recombines with a hole in the valance band and emits a photon. The radiative recombination rate can be deduced from the detailed balance theory and can be represented using the generalized Planck Radiation Law [27]:

$$j_r = a(E)\frac{2\pi}{h^3c^2}\int_{Eg}^{\infty}\frac{E^2}{\exp\left\{\frac{E-\left(E_{\mathrm{fn}}-E_{\mathrm{fp}}\right)}{kT}\right\}}\mathrm{d}E \tag{2.1}$$

Here, a is the absorption coefficient, which depends on the photon energy, c is the velocity of light, E is the photon energy, and $E_{\mathrm{fn}} - E_{\mathrm{fp}}$ is the difference of the quasi-Fermi levels across the p-n junction. This equation forms the basics of the one-diode equation describing a solar cell, which will be introduced in Section 2.1.1.

Solar cells can be fabricated from different semiconductor materials [21]. The most commonly fabricated solar cell today are silicon wafer solar cells which can be sub-divided into solar cells made from monocrystalline and multicrystalline material. C-Si wafer based solar cells have an ordered crystal structure and exhibit predicable and uniform behaviour. Their behaviour can be well described by existing models, which are used for modelling and simulation in various applications [28, 29].

2.1.1 Solar cell one-diode model

In order to describe the current-voltage behaviour of a solar cell, diode models are commonly used in the modelling and simulation of solar cells. Due to its p-n junction

nature, the one-diode model can be applied to model the I-V characteristics of a solar cell. The governing equation for the one-diode model is given by [30, 31]:

$$j(V) = j_{\mathrm{ph}} - j_0 \left\{ \exp\left[\frac{q(V + j(V)R_{\mathrm{s}})}{nkT} \right] - 1 \right\} - \frac{V + j(V)R_{\mathrm{s}}}{R_{\mathrm{sh}}} \tag{2.2}$$

where j is the output current density of a solar cell, V is its terminal voltage, j_{ph} is the photocurrent density, j_0 is the reverse saturation current density, n is the diode ideality factor, R_{s} is the lumped series resistance, R_{sh} is the shunt resistance, q is the electronic charge (1.6×10^{-19} C), k is the Boltzmann constant (1.38×10^{-23} J/K) and T is the cell temperature in Kelvin. Equation 2.2 is written in such a way that the solar cell's maximum power point lies in the first quadrant.

The equation is a simplification and extension of the generalized Planck Law in Equation 2.1. Based on the one-diode equation, the solar cell's I-V characteristics can be illustrated and some important quantities can be discussed. Figure 2.4(a) shows the equivalent circuit of the one-diode model. Figure 2.4(b) shows a comparison of a measured c-Si solar cell I-V curve and a fitted one, using the one-diode model. In the shown case, the one-diode model represents the solar cell I-V characteristics very well. The parameters describing the I-V behaviour of a solar cell are given in Table 2.1.

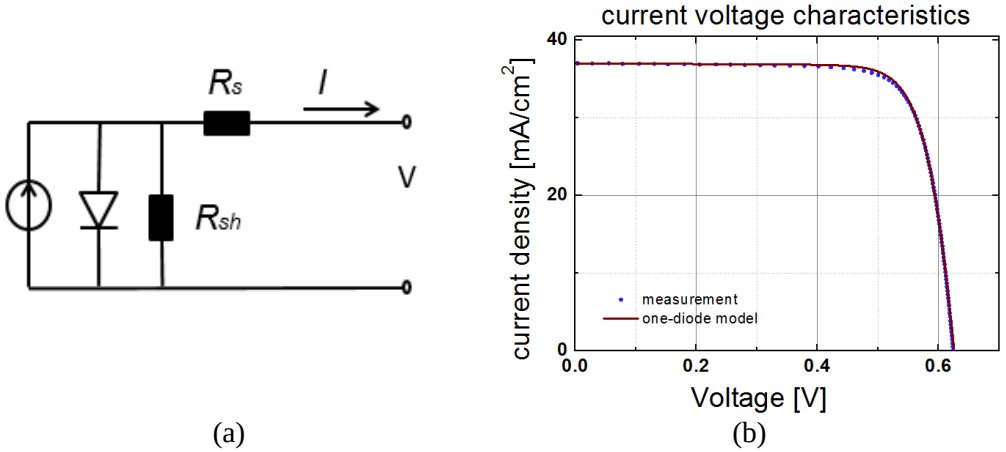

(a) (b)

Figure 2.4: (a) The equivalent circuit model of the one-diode model. (b) The measured solar cell current-voltage curve and the fitted one using one-diode model.

Table 2.1: The main parameters describing the I-V characteristics of solar cell.

I_{sc}	Short-circuit current, describing the current generated by the cell under short-circuit condition (i.e. zero external resistance and no applied voltage)
j_{sc}	Short-circuit current density, describing the current density generated by the cell under zero applied voltage.
V_{oc}	Open-circuit voltage, voltage at the terminals under open-circuit condition.
p_{mpp}	Maximum power density, describing the maximum power that can be delivered by the solar cell.
j_{mpp}	Current density at the maximum power point.
V_{mpp}	Voltage at the maximum power point.
η	Solar cell efficiency, which is the most important parameter of a solar cell.
FF	Fill factor, which, in conjunction with I_{sc} and V_{oc}, determines the efficiency of a solar cell.
R_s	Series resistance, describing the resistive loss due to the current transport within the solar cell.
R_{sh}	Shunt resistance, related to the leakage through defects and so on.

The efficiency of the solar cell is defined as:

$$\eta = \frac{p_{\mathrm{mpp}}}{p_{\mathrm{in}}} \tag{2.3}$$

Here, p_{in} is the power density of the external illumination.

The fill factor of the solar cell is defined as:

$$FF = \frac{p_{\mathrm{mpp}}}{j_{\mathrm{sc}} \times V_{\mathrm{oc}}} \tag{2.4}$$

The fill factor is usually affected by the parasitic resistances of a solar cell, which will be discussed in Section 2.1.2.

2.1.2 Effect of parasitic resistances

The parasitic resistances of a solar cell refer to the series resistance and shunt resistance, both of which have an influence on the fill factor of a solar cell. Series resistance is predominantly accumulated during lateral transport of current, which includes the resistances from [32]:

(1) emitter and base of the solar cell;

(2) the contact between metal and semiconductor;

(3) the metal electrodes on the front and the rear surfaces.

The (lumped) series resistance of a solar cell is usually influenced by the metallization design and the quality of the metallization. Problems like high contact resistance, broken fingers and busbars will make the solar cell series resistance higher. If the series resistance gets larger, there will be more power loss during current transport, thus the solar cell fill factor drops.

The shunt resistance of silicon wafer solar cells usually originates from manufacturing defects. Shunts can be caused by the residual emitter at the cell edge and the aluminium particles at the cell surface. Shunts can also be caused by cracks and holes [33]. The presence of these defects lead to leakage currents, which reduce the current flowing through the cell junction. Low shunt resistance of a solar cell reduces the fill factor as well as the open-circuit voltage of the solar cell. Figure 2.5 shows the influence of series resistance and shunt resistance on the I-V curve of a c-Si solar cell.

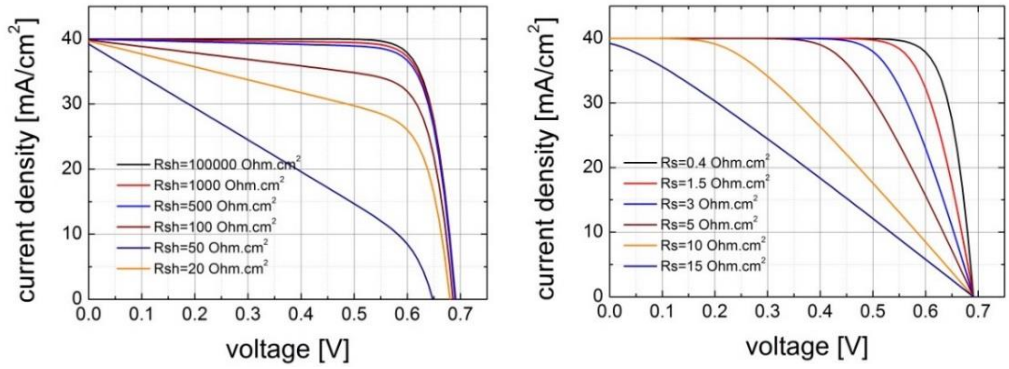

(a) (b)

Figure 2.5: (a) Influence of the shunt resistance on the I-V curve of a solar cell. (b) Influence of the series resistance on the I-V curve of a solar cell.

2.2 Basics of c-Si wafer PV modules

The basic principles of c-Si wafer solar cells were introduced in Section 2.1. The present section focuses on the fundamentals of c-Si wafer based PV modules, which is the background required for the studies presented in Chapters 4 to 7. In the first step, it is explained how c-Si PV module I-V characteristics are related to the I-V characteristics of individual cells. After that, the cell-to-module losses are introduced.

2.2.1 Interconnection of solar cells

For outdoor applications, solar cells are connected and packaged into a PV module, which, in turn, is the basic unit of a PV system. There are mainly two functions of a PV module: (1) it provides the current and voltage level required by a PV system by interconnecting the solar cells. (2) It is a mount for the solar cells and also protects the solar cells from the damage of the environment during operation.

Since the electrical output of a single solar cell usually cannot fulfil the demand of most applications, they have to be electrically connected within a PV module. For c-Si wafer PV modules, there are mainly two ways of connection: series connection and parallel connection (parallel connection is less often applied). A c-Si PV module is usually composed of a certain amount of solar cells connected in series and parallel.

Assuming the total number of cells connected in series is N_s and the total number of strings connected in parallel is N_p, the total number of cells within the PV module is N, and that the I-V characteristics of all the cells are identical and there is no CTM loss, then the I-V characteristics of the PV module becomes [35]:

$$I_{\mathrm{scM}} = N_{\mathrm{p}} \times I_{\mathrm{sc}} \tag{2.5}$$

$$V_{\mathrm{ocM}} = N_{\mathrm{s}} \times V_{\mathrm{oc}} \tag{2.6}$$

$$P_{\mathrm{mppM}} = N \times P_{\mathrm{mpp}} \tag{2.7}$$

Here, I_{scM}, V_{ocM} and P_{mppM} are the short-circuit current, open-circuit voltage and the maximum output power of the PV module.

Figure 2.6 shows a typical c-Si wafer-based PV module consisting of 60 solar cells connected in series. The current output of this PV module is equal to the current of an individual solar cell. The voltage output of the PV module is the sum of the voltages of all the cells. Typically, three bypass diodes are introduced into the circuit in order to prevent the solar cells from running in reverse-bias if one or more cells are shaded (for example by a bird), and also to avoid "hot spot" damage [36].

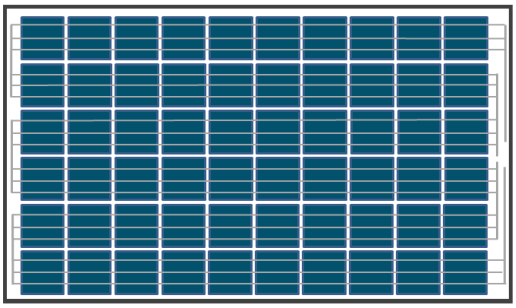

Figure 2.6: A c-Si PV module composed of 60 c-Si solar cells connected in series.

2.2.2 Cell-to-module loss

The efficiency of industrial c-Si wafer solar cells has increased significantly over the years. However, due to cell-to-module losses, improvements in cell efficiency cannot be fully transferred to the PV module efficiency. There are mainly two aspects for the cell-to module loss: optical loss and electrical loss. In this part, a review for each kind of CTM loss is presented.

2.2.2.1 Optical losses

The optical losses within a PV module have already been well investigated [37-40]. Optical losses within a PV module are caused by reflection and parasitic absorption. Reflection losses occur at the interfaces of different layers. Parasitic absorption losses occur within the glass and encapsulant layer and within the non-active components of the solar cell (e.g. fingers, busbars or anti-reflection coating). Figure 2.7 shows the main optical loss mechanisms for a c-Si PV module. Reflection of incident rays occurs at (1) the air-glass interface, (2) the glass-encapsulant interface, (3) the encapsulant-cell interface or encapsulant-metal finger interface, and (4) the encapsulant-backsheet interface. In processes (3) and (4), the reflected light is often diffuse, and a substantial amount of the diffuse light is total-internally reflected at the glass-air interface. Absorption of incident light happens within the glass (5), the encapsulant (6) and the backsheet (7).

It should be noted here that when solar cells are encapsulated into a PV module, the contribution of initial optical losses changes because of the encapsulation. When considering the contribution of different loss mechanisms, the optical losses at each interface and layer cannot be treated separately, since they are all optically inter-connected. The detailed optical assessment of a c-Si PV module can be achieved by ray-tracing, as shown in Ref. [41]. Apart from ray-tracing, which is usually time consuming, a holistic method is used in Ref. [42]. This method is based on a combination of measurements and analytical procedures, and is able to quantify and distinguish optical loss mechanisms.

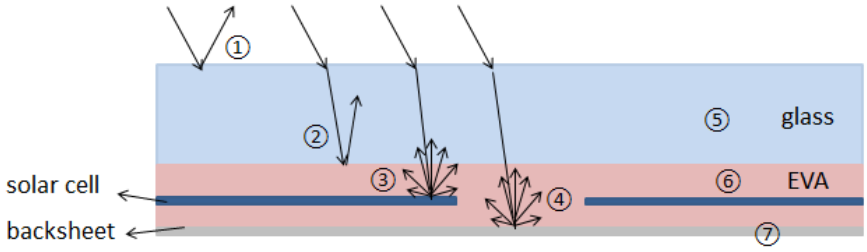

Figure 2.7: Cross section of a c-Si wafer based PV module and the optical loss mechanisms as introduced in the text.

2.2.2.2 Resistive losses caused by ribbons

Besides optical losses, c-Si PV modules also suffer from resistive losses [43], particularly in the ribbons connecting the solar cells. The ribbon resistive loss analysis presented in this part was derived by the author, which forms the basic theory of Chapter 4. As already mentioned in Section 2.2.1, series connection is often applied in a c-Si PV module. The series connection is realized by ribbons, including both ribbons for the interconnection of cells and the bussing ribbons for the connections of strings. CTM resistive loss is mainly caused by the ribbons, which is usually quantified as follows:

In a c-Si PV module, tin-coated copper ribbons are used to interconnect the silicon wafer solar cells. For each solar cell, there is at least one ribbon on the top and at least one ribbon at the bottom. The current flows from the bottom ribbon through the solar cell, and then flows out of the cell via the top ribbon. If the total current generated by one solar cell is I_L, the current along the top ribbon increases linearly from 0 to I_L, and the current in the bottom ribbon decreases linearly from I_L to 0 across the length of the cell (as shown in Figure 2.8).

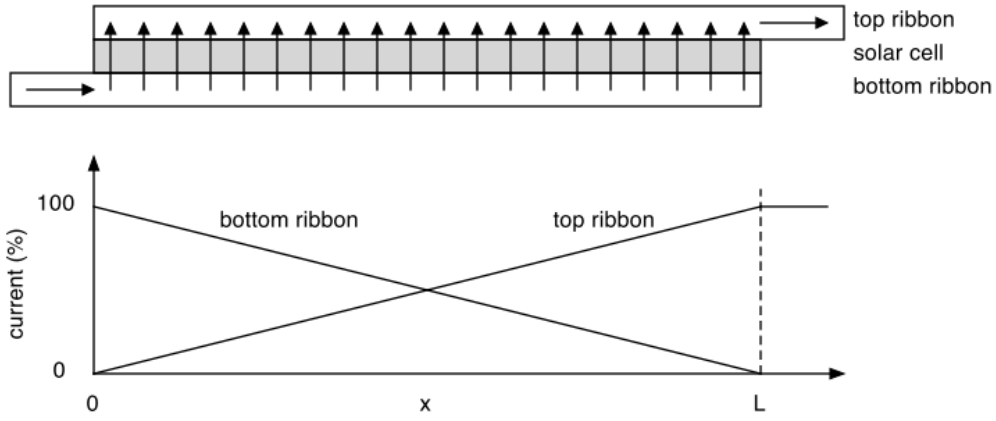

Figure 2.8: The current flow in a solar cell cross section with a metal ribbon on both sides.

From Figure 2.8, the current flowing through the top ribbon as a function of the position *x* is

$$I_{\text{top}} = I_{\text{L}} \frac{x}{L}, \tag{2.8}$$

where L is the ribbon length.

Similarly, the current flowing through the bottom ribbon is

$$I_{\text{bottom}} = I_{\text{L}} \left(1 - \frac{x}{L}\right). \tag{2.9}$$

Thus the power loss in the top ribbon is

$$P_{\text{loss\_top}} = \int_0^L (I_{\text{L}} \frac{x}{L})^2 r \mathrm{d}x = \frac{r L I_{\text{L}}^2}{3}, \tag{2.10}$$

where r is the ribbon resistance per unit length, with a unit of Ω/cm.

Similarly, the power loss of the bottom ribbon is also $\frac{rLI_{\text{L}}^2}{3}$, thus for each cell the total power loss caused by ribbon resistance is $\frac{2rLI_{\text{L}}^2}{3}$. Since $P = I^2 R$, the effective ribbon resistance R_{r} of one cell is

$$R_r = \frac{2rL_{\mathrm{bb}}}{3N_{\mathrm{bb}}}, \tag{2.11}$$

where L_{bb} is the busbar length, and N_{bb} is the number of busbars.

If the module is composed of *N* cells connected in series, the power loss on the ribbon within the cell area is:

$$P_{\mathrm{loss\_module}} = NI_{\mathrm{L}}{}^2 R_{\mathrm{r}} \tag{2.12}$$

Besides the resistive power loss on the ribbon in the cell area, there is also power loss on the ribbon in the gaps between the cells and on the bussing ribbons. Bussing ribbons are used for string interconnection within a c-Si PV module, which are wider than the ribbons for cell interconnection. These two resistive losses can be easily calculated with known gap size and bussing ribbon length. After calculating the resistive power loss on all the ribbons in a module, the total cell-to-module resistive loss can be obtained.

2.2.2.3 Mismatch loss

The mismatch loss is also an important factor that affects the power output of a c-Si PV module. Due to the series connection of the cells within a c-Si PV module, all cells must operate at the same current. The mismatch loss mainly includes two aspects:

(1) Solar cells within a PV module have different characteristics [44]. In a series connection, the solar cell with the lowest intrinsic current will force other cells to operate at the same current and limit the PV module power output.

(2) Under inhomogeneous illumination conditions (e.g. partial shading) [45]. Cells under lower illumination generate lower current and force the other cells to operate at the same current.

The mismatch effect resulting from partial shading usually makes some cells suffer from high reverse bias, which might further cause hotspot on the solar cells and induce PV module degradation. In order to prevent these potential damages, bypass diodes are introduced into a c-Si PV module. A bypass is connected in parallel to a string of solar cells, but with opposite polarity. Under normal operating condition, the solar cells are forward biased thus the bypass diode is reverse biased and acts as open circuit. However, under partial shading condition, the bypass diode is forward biased and allows the current to flow through it instead of reverse biasing the other cells.

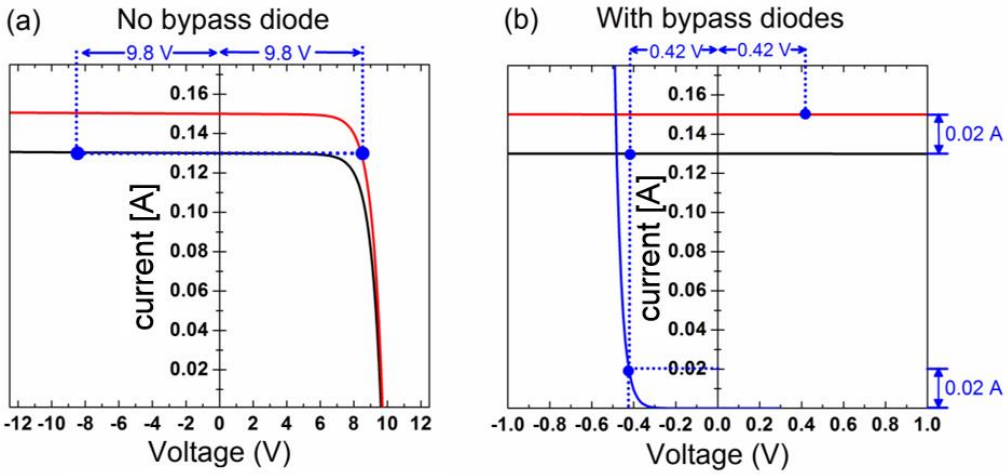

Figure 2.9: I-V curves and operating points of two solar cell strings generating different current and connected in series. Each of the strings is composed of 20 solar cells. The red curve shows the I-V characteristics for the string generating higher current; the black curve shows the I-V characteristics for the string generating lower current. (a) shows the case when there are no bypass diodes connected in the circuit; (b) shows the case when there is one bypass diode connected in parallel with each string.

Figure 2.9 shows the operating current-voltage points of two series connected strings under illumination simulated by the author. Each string is composed of 20 solar cells connected in series. Figure 2.9(a) shows if there are no bypass diodes connected, the reverse is 9.8 V for the string that produces the lower current. If there is one bypass diode connected in parallel with each string, the reverse bias decreases to 0.42 V (shown in Figure 2.9(b)). In this way, the bypass diode prevents the string with lower current from becoming seriously reverse biased.

2.3 Solar radiation and its composition

The characteristics of photovoltaic devices are usually evaluated by the I-V parameters measured under the standard test condition (STC). However, in the real operating condition, different factors affect the output power of the c-Si PV modules, including the PV module tilt angle, solar irradiance, diffuse fraction, ground albedo and so on. In Chapter 7 the output power is evaluated for different kinds of c-Si PV modules according to the environmental factors. Thus in this part, the basic theories about solar radiation and different radiation components are introduced.

2.3.1 Solar radiation

Solar energy is produced by the sun, which can be regarded as a "blackbody" radiator. A blackbody is an idealized physical body that absorbs all incident electro-magnetic radiation [27]. Under thermal equilibrium condition, a blackbody emits electromagnetic radiation according to Planck's Law, which states that the spectrum emitted by a blackbody is only determined by its temperature and can be expressed by the Planck equation [26]:

$$E(\lambda, T) = \frac{2\pi hc^2}{\lambda^5[\exp\left(\frac{hc}{\lambda kT}\right) - 1]} \tag{2.13}$$

Here, E has the dimension of power per unit area per unit wavelength, λ is the wavelength, T is the blackbody temperature in Kelvin, and h is Planck's constant.

The sun can approximately be described as a blackbody with a temperature of 5800 K. However, when sunlight passes through earth's atmosphere, it is scattered and absorbed by different atmospheric constituents. Thus the composition of the solar spectrum changes when it reaches the earth's surface. Under clear sky conditions, the radiation received by the earth depends on the path length of the sunlight through the atmosphere. The path length is usually referred to as air mass (AM) and approxi-mated by $1/\cos(\theta_z)$, where θ_z is the angle between the surface normal and the

incoming sunlight. When the sun is directly overhead, since the path length is the shortest (AM = 1), the earth's surface receives the highest amount of radiation. The standard spectrum for the temperate latitudes is the AM 1.5 spectrum, corresponding to an angle of elevation of 42^0 [25, 46] (shown in Figure 2.10). The AM 1.5 spectrum is also used as the standard spectrum operation condition for a PV device [47-49].

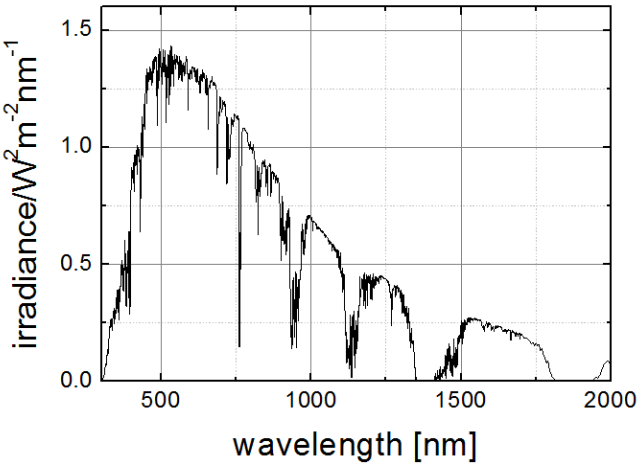

Figure 2.10: The standard terrestrial (AM 1.5) solar spectrum.

2.3.2 Direct and diffuse radiation

In terrestrial illumination conditions, there is a distinction between direct and diffuse radiation [50]. Direct radiation describes the solar radiation travelling on a straight line from the sun down to the surface of the earth. Diffuse radiation describes the sunlight that is scattered by the molecules and particles in the earth's atmosphere but still reaches the surface of the earth [51]. As a consequence, direct light comes from a specific direction, but diffuse light comes from all directions [52]. The sunlight outside earth's atmosphere is direct light. When sunlight passes through the atmosphere, atmospheric scattering happens, which results in a diffuse component of the sunlight [53-56]. There are mainly two scattering effects:

(1). Rayleigh scattering caused by molecules in the atmosphere, which mainly occurs at short wavelengths [57].

(2). Mie scattering caused by aerosols and dust particles [58].

The proportion of diffuse radiation depends on the weather condition (e.g. cloud cover). On a clear day, usually 10% of the total incident solar radiation is diffuse radiation [59]. Since the proportion of direct and diffuse radiation is very important information for many studies and is very hard to derive directly, different models have been developed [59-68]. In this work, the different irradiance components are calculated as follows:

The extraterrestrial radiation, which describes the intensity of solar radiation directly outside the earth's atmosphere on a horizontal surface, can be expressed by a yearly varying term [69]:

$$I_0 = 1367.7 \times [1 + 0.033 \times \cos\left(\frac{2\pi}{365} \times DOY\right)] \tag{2.14}$$

I_0: extraterrestrial radiation; *DOY*: day of a year, *DOY* = 1 if the date is January 1st.

Direct normal irradiance (*DNI*) is defined as the solar radiation incident on a surface oriented normal to the solar radiation. It can be calculated from the extraterrestrial radiation, which is a function of the transmission coefficient [70]. This relationship is based on a model developed by Liu and Jordan [71]. In this model, *DNI* is calculated as a function of air mass.

With a known air mass value, the direct normal incidence is calculated by:

$$DNI = I_0 \times \tau^{AM} \tag{2.15}$$

Here, τ is the transmission coefficient for direct solar radiation.

If *DNI* is known, horizontal direct radiation (H_{dir}), which refers to the direct radiation incident on a horizontal surface, can be obtained directly from:

$$H_{\mathrm{dir}} = DNI \times \cos(\theta_{\mathrm{z}}) \tag{2.16}$$

Another important irradiance component is called horizontal diffuse radiation (H_{diff}), which is defined as the amount of diffuse radiation incident on a horizontal surface. The commonly used method to calculate H_{diff} was developed by Campbell and Norman , which is based on Liu and Jordan's model and described by [72]:

$$H_{\text{diff}} = 0.3(1 - \tau^{AM}) I_0 \cos(\theta_z) \tag{2.17}$$

However, this equation is mostly used to model clear-sky conditions when the transmission coefficient τ is larger than 0.45 and might not be very suitable for overcast conditions. Under overcast conditions, there are no existing models that directly relate diffuse radiation to the transmittance coefficient τ. However, there are many models that relate diffuse fraction k_d to clearness index k_t. Here k_d and k_t are defined as follows:

$$k_{\text{d}} = \frac{H_{\text{diff}}}{H_{\text{dir}} + H_{\text{diff}}} \tag{2.18}$$

$$k_{\text{t}} = \frac{H_{\text{dir}} + H_{\text{diff}}}{I_0 \times \cos\theta_z} \tag{2.19}$$

$$k_{\text{b}} = \frac{H_{\text{dir}}}{I_0 \times \cos\theta_z} \tag{2.20}$$

Diffuse radiation can then be related to the transmittance coefficient by the relationship between k_d and k_t [73]. Normally, k_d can be expressed as a linear function of k_t, and the general expression is described as follows:

$$k_{\text{d}} = \text{A} + \text{B}k_{\text{t}} \tag{2.21}$$

A and B are the coefficients used in the model. Since

$$k_{\text{d}} \times k_{\text{t}} + k_{\text{b}} = k_{\text{t}} \tag{2.22}$$

and k_b can be obtained from (2.20), k_t and k_d can be obtained using (2.21) and (2.22):

$$k_{\mathrm{t}} = -\frac{(\mathrm{A}-1)+\sqrt{(\mathrm{A}-1)^2-4\mathrm{B}}}{2B} \tag{2.23}$$

$$k_{\mathrm{d}} = -\frac{(\mathrm{A}+1)-\sqrt{(A-1)^2-4\mathrm{B}}}{2} \tag{2.24}$$

In order to verify this method, different models describing the relationship between k_t and k_d are used in the calculation. A review of different models can be found in Ref. [74]. In this thesis, Reindl's model and Orgill and Hollands' model are used for comparison in Chapter 7. The difference of the two models are the values of the defined coefficients A and B under different clearness index ranges. Table 2.2 describes the different models used in this work.

Table 2.2: Description of different models used in calculation relating k_t and k_d.

Model	A	B	Range
Reindl et al. [75]	1.02	-0.248	$k_t \leq 0.3$
	1.45	-1.67	$0.3 < k_t < 0.78$
	0.147	0	$k_t \geq 0.78$
Orgill and Hollands [76]	1	-0.249	$k_t < 0.35$
	1.577	-1.84	$0.35 \leq k_t \leq 0.75$
	0.177	0	$k_t > 0.75$

With k_t and k_d, the horizontal diffuse radiation is calculated by:

$$H_{\mathrm{diff}} = I_0 \cos(\theta) \times k_{\mathrm{t}} \times k_{\mathrm{d}} \tag{2.25}$$

Finally, the average diffuse fraction for one year is calculated via:

$$\text{diffuse fraction} = \frac{H_{\mathrm{diff}}(for\ one\ year)}{H_{\mathrm{diff}}\ (for\ one\ year) + H_{\mathrm{dir}}(for\ one\ year)} \tag{2.26}$$

3 Methodology

This thesis mainly focuses on c-Si wafer based PV modules, whereby such PV modules were constructed, characterized and simulated. This chapter introduces the most important experimental and simulation methods used in this thesis. Section 3.1 describes the experimental methods used in this thesis, which are c-Si PV module fabrication methods. C-Si PV module characterization methods are then introduced in Section 3.2, in which the I-V measurement and spectral response measurement are introduced. Section 3.3 describes electrical and optical models used for computer-based simulation. In Section 3.3.1, the electrical network modelling tool "Griddler" for simulating large-area solar cells [77] is introduced. Section 3.3.2 introduces electrical circuit modelling for c-Si PV modules. In Section 3.3.3, analytical optical models for calculating backsheet induced optical gain are introduced. Section 3.3.4 describes the model for calculating the solar irradiance received by a tilted surface.

3.1 Experimental methods - c-Si PV module fabrication

In this thesis, several different types of c-Si PV modules were fabricated and investigated, including PV modules using standard c-Si solar cells, PV modules using halved c-Si cells, PV module with glass-backsheet construction and PV module with glass-glass construction. Also, both mini-modules for experimental use and industrial-size c-Si PV modules were fabricated and tested. In this part, the structure of a c-Si PV module and its fabrication process are described in detail.

3.1.1 C-Si wafer based PV module structure

In Section 2.2.1 the interconnection of c-Si solar cells within a PV module was introduced. When packaging the cells into a PV module, some important factors about the module structure need to be considered: 1. The module must protect the cell from detrimental influences of the environment. 2. The module should ensure that the cells perform optimally. Figure 3.1(a) shows the most commonly used structure for a

c-Si PV module. In a c-Si PV module, solar cells are connected with thin ribbons on their upper side. Normally, the cells are placed between a backsheet on the bottom and a transparent glass pane on the top. The glass pane is usually made of low-iron glass in order to provide high transmission of light in the wavelength range that can be used by the solar cell. Another method to reduce reflection is to use a textured glass pane [78]. However, textured glass surfaces tend to accumulate dust and other dirt, which blocks light from reaching the solar cells. Besides providing good optical characteristics, the glass pane should also be stable in the real environment, protecting the cells from water and offering high mechanical strength and low thermal resistivity. Besides glass, the front layer can also be made of acrylic and polymers. Low-iron glass is most commonly used, since it has relatively low cost, good stability, good optical properties and high mechanical strength.

Encapsulant is another component used in a c-Si PV module to provide adhesion between the front glass pane and the backsheet. The most commonly used encapsulant material for c-Si PV modules is ethylene vinyl acetate (EVA). This material must be stable against the UV photons transmitted through the front glass pane and tolerate a wide operational temperature range (say -50°C to +80°C). The bottom layer of a PV module should have low thermal resistance and prevent the penetration of water and water vapour at the same time. The most commonly used materials for the bottom layer are Tedlar®, PET and polyamide, which are thin polymer sheets.

Besides the commonly used glass-cell-backsheet construction for monofacial silicon wafer solar cells, there are also PV modules using bifacial solar cells which allow the module to receive sunlight from both sides. The configuration of a bifacial c-Si PV module is shown in Figure 3.1(b). For this type of PV module, instead of using a backsheet as the bottom layer, glass is used to allow the cell to receive sunlight also

from the rear. Also, glass-glass construction makes bifacial modules more advantageous in terms of durability.

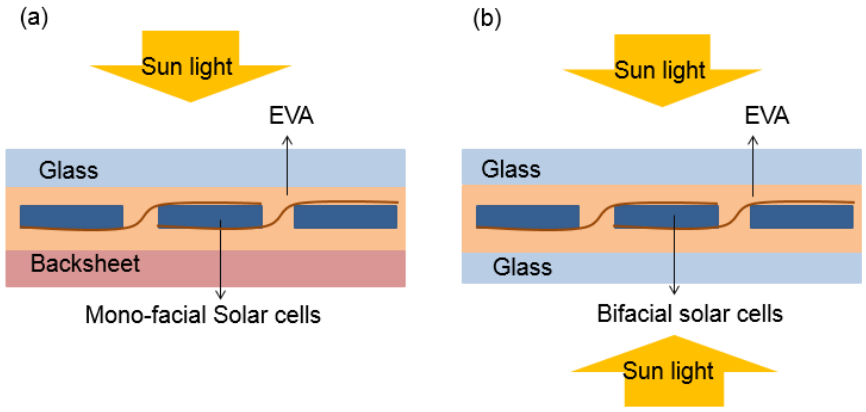

Figure 3.1: The setups of (a) a monofacial c-Si PV module and (b) a bifacial c-Si PV module. The directions of the incident light which can be utilized by the two kinds of modules are also included.

3.1.2 C-Si PV module fabrication

Figure 3.2 shows a flowchart describing the fabrication process of a c-Si PV module. In a first step, the solar cells are characterized and sorted for similar characteristics, since solar cells with similar I-V characteristics ensure minimal power losses when they are packed into a PV module.

In a second step, selected cells are connected into strings. The connection is done by soldering the ribbons to front and rear busbars of a solar cell. String size depends on the designed module current and voltage. For a standard industrial size c-Si PV module, normally ten solar cells are soldered into one string. For the mini-modules used in the experiment, they only include one standard full-size solar cell or two halved solar cell connected in one string.

In a third step, the strings are interconnected using bussing ribbons, so that all cells are connected within a whole circuit.

In a last step, the PV module is assembled using lamination [79]. During this process, the electrical-connected solar cells are placed between two sheets of encapsulant. This "sandwich" structure is placed on the glass and covered by the backsheet. Finally, this pre-laminated module is placed in the laminator. The temperature of the lamination process is usually around 150 ^{0}C, and during this process the encapsulant melts and forms a sealing for the cells. After that, a curing process is performed. The EVA resin polymerization occurs during this step. The PV module may then be further equipped with a frame and a junction box. These steps conclude the fabrication process. Figure 3.3 shows an example of the fabricated mini-modules used in this work.

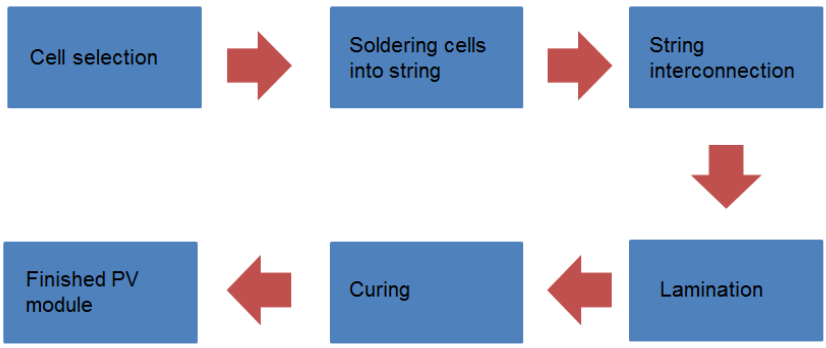

Figure 3.2: C-Si PV module fabrication process.

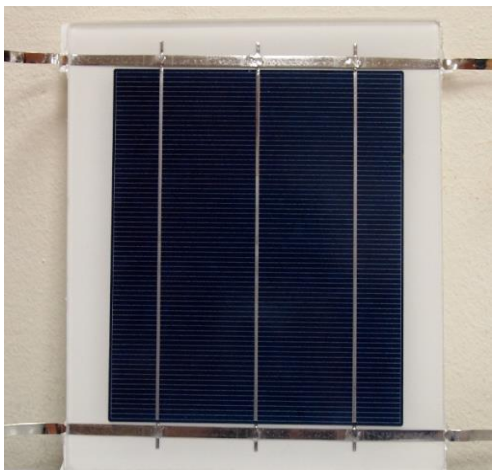

Figure 3.3: An example of a fabricated mini-module used in this thesis.

3.2 Characterization method

3.2.1 I-V measurement

I-V measurement is one of the most fundamental characterization techniques for solar cells and PV modules. Through this measurement, the current-voltage characteristics of a solar cell or a PV module can be obtained, including the short-circuit current, open-circuit voltage, fill factor and efficiency. The photovoltaic devices are required to be measured under following standard test conditions (STC) [80]:

1. Under AM1.5 spectrum
2. Under one-sun illumination condition, with light intensity of 1000 W/m^2
3. Under cell temperature of 25^0C

As indicated in Figure 3.4, an I-V tester uses a four-wire measurement in order to remove the influence of the probe contact resistance. The two source pins measure the operating current of the solar cell, and the sense pins measure the operating voltage. When measuring the I-V characteristics of a single solar cell, a chuck with many contact pins is used to make direct contact with the busbars of the solar cell. By this way, current does not need to travel a long way through the busbar. The measured results only indicate the solar cell I-V characteristics and do not include the influence of any current transport along the busbars. When measuring a c-Si PV module, the contact pins are connected directly to the ribbons. The resistive loss caused by current transporting through the ribbons will influence the measured fill factor, which is closer to the actual operating conditions of the solar cell in a PV system.

The photovoltaic device is then illuminated. Normally a variable resistor load is applied in the system. By changing the resistance value, the operating current and voltage of the device are changed and the whole I-V curve of a photovoltaic device can be obtained.

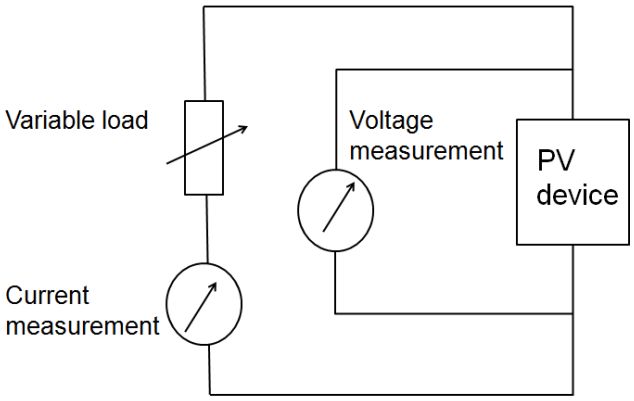

Figure 3.4: The equivalent circuit for the I-V measurement of PV devices.

3.2.2 Spectral response measurement of c-Si PV modules

Spectral response (SR) is a commonly used characterization method for PV devices. SR measurements provide spectrally resolved information about current generation and recombination, and can be used to deduce information about diffusion mechanisms in photovoltaic devices [81]. Typically, the spectral response of a PV device is measured by illuminating with a narrow-bandwidth light at a series of different wavelengths and bias light [82]. Since the solar cells are usually evaluated under STC condition, the intensity of a certain wavelength corresponds to the standard AM1.5 G spectrum. Monochromators and filters are commonly used for wavelength selection. The current of the device is then measured under short-circuit conditions. The spectral response of the device is calculated by dividing the measured current density by the current corresponding to the irradiance at each wavelength. The typical SR of a PV device decreases both at the short wavelength region and the long wavelength region. In the short wavelength region, the photon energy is much larger than the bandgap energy, and the exceeded energy cannot be utilized by the PV device but only generates heat. In the long wavelength region, photons with energy lower than the bandgap cannot be utilized by the semiconductor.

When measuring a large-size c-Si PV module, an ideal high-intensity large-area uniform monochromatic light source is required. However, this kind of light source is

not readily available. In this section, two different measurement methods are introduced: partial illumination and flash measurements [83]. The advantages and disadvantages of the two measurement methods will then be compared in Section 6.2.3.

3.3.2.1 Partial illumination method

In this method, the SR of a target cell within a c-Si PV module is measured. During the measurement, the whole module except the target cell is illuminated by a white bias light with an intensity of 100-300 W/m^2. A subpart of the target cell with an area of 5 cm × 5 cm is illuminated by both quasi-monochromatic light with an intensity of 50 μW/cm^2 and white bias light with an intensity of 700 W/m^2. The remaining part of the target cell is not illuminated, and the average irradiance received by the target cell is around 50 W/m^2. By this way, the irradiance received by the target cell is much lower than that of the other cells within the PV module, thus the target cell limits the operating current of the whole module [84, 85]. The measured module current is equal to the current produced by the target cell. By applying a bias on the whole module, the SR of the target cell can be measured under zero bias.

With the same procedure, the SRs of several target cells within the c-Si PV module are then measured. If the variation of the SRs of the target cells is small, the SR closest to the average of all the measured SR is reported as the SR of the module. If there is large variation of the measured SRs, more cells' SRs are measured. Instead of reporting an average SR of the PV module, the spatial distribution of the SR within the PV module is reported.

3.3.2.2 Full-area flash illumination method

In this method, a pulsed solar simulator (PASAN IIIB) is used to illuminate the whole PV module. The solar simulator is equipped with a filter box containing 15 quasi-monochromatic filters covering the wavelength range from 400 nm to 1100 nm. As a

consequence, a high-intensity quasi-monochromatic beam over a large area is achieved in the measurement [86, 87]. No bias light is required in this method, and the SR of the c-Si PV module can be directly obtained from the measured short-circuit current at each wavelength range. However, the bandwidths of the band filters have to be wide enough to ensure a sufficiently high intensity of the quasi-monochromatic radiation. This wide bandwidth can introduce errors to the measurement [2]. Also, this method requires large-area illumination; thus, the illumination uniformity is another challenge, since any non-uniform illumination can introduce errors to the measurement results. Thus the measurement is improved by using a reference solar cell, the SR of which is already known. Both SR of the PV module and SR of the reference solar cell are measured under the same illumination condition. The module SR is calibrated by the measured SR and the initial SR of the reference cell. The SR of the c-Si PV module is calculated by:

$$SR^{Test}(\lambda) = \frac{I_{sc}^{Test}(\lambda)/A^{Test}}{I_{sc}^{Ref}(\lambda)/A^{Ref}} \times SR^{Ref}(\lambda) \tag{3.1}$$

where $I_{sc}^{Test}(\lambda)$ and $I_{sc}^{Ref}(\lambda)$ are the measured short-circuit currents of the PV module and the reference cell under the quasi-monochromatic illumination. A^{Test} and A^{Ref} are the total cell area of the PV module and the area of the reference cell, and $SR^{Ref}(\lambda)$ is the calibrated SR of the reference cell

3.3 Simulation method

3.3.1 Network modelling for interconnected solar cells

The electrical performance of c-Si PV modules is affected by the interconnecting resistive loss of solar cells. In this thesis, the resistive loss analysis is done in Section 4.1, using a two-dimensional (2D) network model implemented in a simulator called Griddler [77]. This simulator is able to simulate the current flow distribution within metal electrodes for a solar cell that is integrated into a PV module. 2D circuit

simulation is an established method for solar cell modelling and SPICE related software is commonly used [88-90]. Figure 3.5 shows the typical circuit structure for the distributed circuit model of silicon wafer solar cells. It is based on the diode model describing a solar cell, which considers different regions of interest, including the metal contacts of solar cells, the metal-semiconductor contact regions and the emitter layer. Each unit element includes a current source, a diode, a shunt resistance and a series resistance. Additional elements represent the front metal grid and the contact resistance between grid and solar cell. Resistances both in direction perpendicular to fingers and in direction parallel to fingers are included in the model so that the current flowing in this 2D network can be simulated. The model parameters for each unit were assigned according to its position and the model geometry.

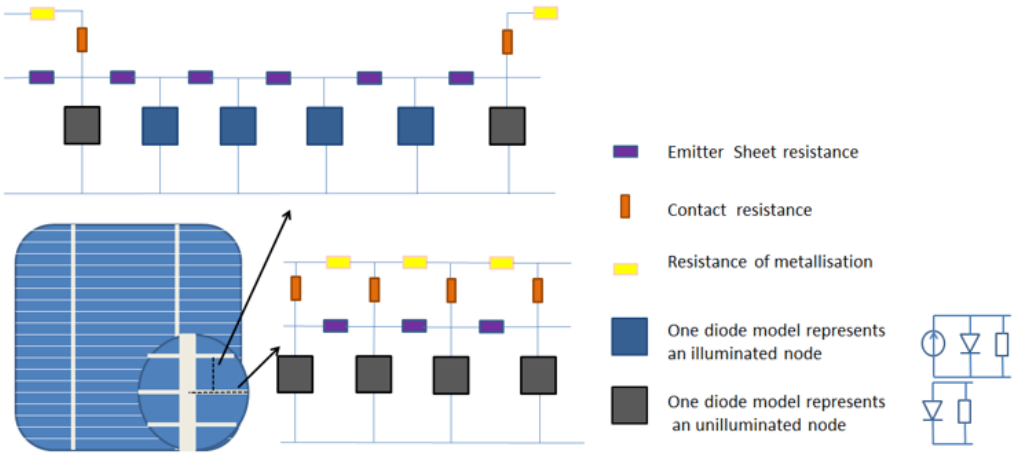

Figure 3.5: Structure of a typical two dimensional circuit model for a silicon wafer solar cell. The cross sections of the circuit model between two adjacent fingers and underneath the finger are shown.

The simulator (Griddler) used in this work uses similar approach as indicated in Figure 3.5. However, it gives a more accurate prediction of a cell's fill factor and power losses than the conventional approach of using simple equivalent-circuit models using SPICE related software. Besides, the ribbons on top of the busbars can also be included in Griddler. Figure 3.6 shows the main interface of Griddler in which all the simulation parameters can be defined. The main input parameters are:

photocurrent density (j_{ph}), open-circuit voltage (V_{oc}), cell shape, emitter sheet resistance ($R_{emitter}$), metallization pattern, the sheet resistance (R_M) and contact resistance (ρ_c) of the fingers and busbars, finger pitch (F_{pitch}), busbar number (N_{bb}), busbar width (W_{busbar}), ribbon width (W_{ribbon}), ribbon height (h_r) and the ribbon resistivity (ρ_r). The simulator solves the current-voltage characteristics of a mini-module using finite element method (FEM). The current flow within the ribbons can also be obtained. Furthermore, the current density and voltage distribution across the surface of the solar cell can be solved and the result is displayed in form of a map. Based on these results, the resistive power loss within the metal contacts and the ribbons can be calculated. More details of the calculation will be introduced in Section 4.1.1.

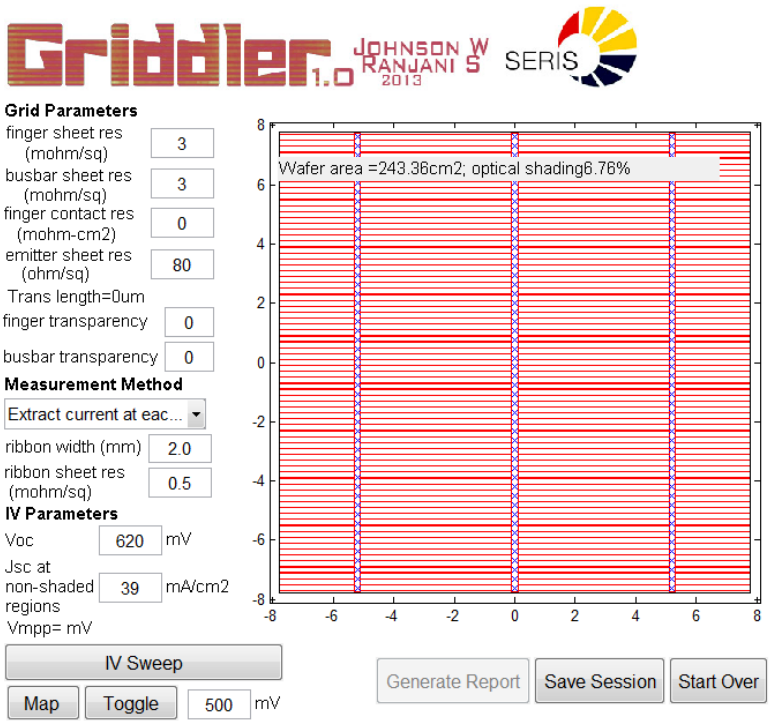

Figure 3.6: The main interface of Griddler. The left side of the interface includes all the required grid parameters. The right side of the interface indicates the defined metal pattern.

3.3.2 Electrical Circuit Modelling for c-Si PV modules

In Section 3.3.1, a c-Si solar cell was modelled by a 2D network model. The circuit model can also be applied to c-Si PV modules. The difference is that, for the circuit modelling of a c-Si PV module, each solar cell is only modelled by a single one-diode unit. Since a c-Si PV module is composed of a certain amount of solar cells connected in series and parallel, it can be modelled with a circuit that is composed of one-diode unit elements (as shown in Figure 3.7). A number of studies using different software (Matlab, SPICE, etc.) were carried out in the past to model the I-V characteristics of a c-Si PV module for different applications, especially for predicting the c-Si PV module behaviour under different conditions [91, 92]. Rosell and Ibanez [93] provided a numerical model that can accurately estimate the output power of a c-Si PV module in outdoor operating conditions. Mermoud and Lejeune [94] and Patel and Agarwal [95] used PVsyst and MATLAB based modelling to investigate c-Si PV module I-V characteristics under partial shading.

In this thesis, a SPICE simulator called LTSpice [96] is used for constructing the circuit model for a c-Si PV module. SPICE simulators were used before to simulate the behaviour of solar cells or PV modules [97-99]. LTSpice is a high-performance SPICE simulator which allows the users to build up the circuit and simulate the electrical behaviours. LTSpice provides a variety of electronic components, such as constant current sources, constant voltage sources, resistors, diodes and capacitors.

Figure 3.7 shows the equivalent circuit of a c-Si PV module used in this thesis. The parameters of each one-diode unit are obtained by fitting the one-diode equation with the measured current-voltage curve of the solar cell. The input parameters include the photocurrent (J_{ph}), diode reverse saturation current (J_0), diode ideality factor (n), series resistance (R_S) and shunt resistance (R_{sh}). There are two ways of building an electrical circuit in LTSpice. One way is to use the graphic interface and draw the whole circuit. Another way is to write a netlist in .txt format. For the modelling of a

c-Si PV module, which is usually composed of hundreds of electrical components, the easier way is to use a netlist. For all simulations done in this work, netlists were generated by an external software – Matlab. The parameters of each solar cell can then be assigned the same or a different value, depending on the investigated problem. In order to get the simulated I-V curve for a circuit shown in Figure 3.7, a variable voltage source or a variable resistor can be applied to the terminal of the circuit. If the variable voltage source is applied, the voltage should be swept from zero to the open-circuit voltage of the simulated PV module. If the variable resistor is applied, the resistance should be swept from zero to a very large value in order to cover both short-circuit condition and open-circuit condition. Usually, the variable voltage method is used due to its much shorter computation time. The I-V curve of a standard c-Si PV module with 60 solar cells connected in series is usually obtained within several seconds.

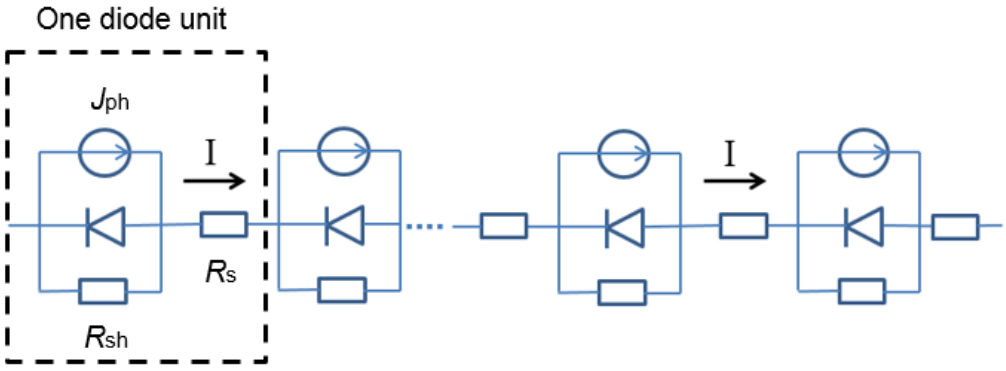

Figure 3.7: Equivalent circuit of a c-Si PV module built in LTSpice. The cells are connected in series, and each cell is represented by a one-diode model. In the one-diode model, J_{ph} is photo-current, R_{sh} is the shunt resistance and R_s is the series resistance.

3.3.3 Optical model for backsheet-induced current gain

Besides electrical modelling, optical modelling is also applied in in this thesis. Optical models used in this thesis were implemented in MATLAB [100], since MATLAB is a convenient choice when dealing with large matrices that were frequently used in the calculus. In this section, a ray-tracing model used to calculate

the amount of light scattered by the backsheet, and reflected back to the solar cell is introduced. The model is used to determine the short-circuit current reaction to a variation of spacing between the cells within a c-Si PV module in Section 5.1.

It is known that light scattered from the exposed backsheet of a c-Si PV module (see Figure 3.8) has an influence on the module's short-circuit current. In this section an optical model built in MATLAB is introduced to precisely determine this amount of light. By using this model, the amount of light that reaches the backsheet and is reflected back onto the area covered by solar cells can be compared with the amount of light that reaches the solar cells directly. An extended ray tracing approach, based on [101-103] is used here.

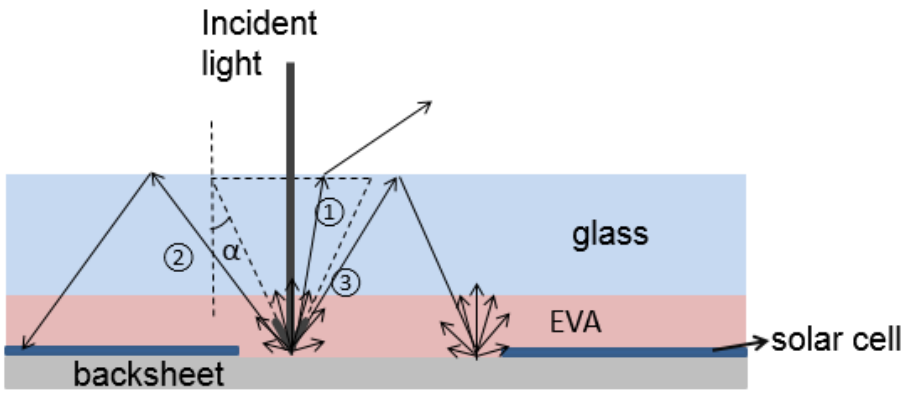

Figure 3.8: The scattering of light by the backsheet of a c-Si wafer PV module. The light paths within the PV module are described. Light incident on the backsheet area between the solar cells is randomly scattered. The scattered light within the escape cone (shown as path ①) will escape from the module and is lost. α refers to the critical angle. The scattered light outside the escape cone can either be reflected back towards the cell-covered area (②) or towards the backsheet area (③). The light that is reflected towards the backsheet area will be scattered once more.

This model uses the following assumptions:

1. The refractive indices of glass and EVA are assumed to be equal, a discussion of which is described in Ref. [42]. Ref. [13] shows that the reflection at glass-EVA interface is below 0.01 %, thus the assumption of equal refractive indices of the two materials is justified.

2. The thickness of the solar cell is ignored. Similar assumptions were used in Ref. [103]. For an industrial c-Si PV module, the thickness of the EVA layer is usually around 0.5 mm, thus there will be a certain amount of light scattered to the rear of the solar cell. We have briefly estimated the overestimation on the calculation result from this assumption. It is calculated that the EVA layer mainly affects the results for the backsheet area within 2 mm from the cell edge. The largest overestimation is around 1.6% relative. The height difference, therefore, is considered as a second order effect and has been neglected in the further study.
3. The quantum efficiency of the cells is independent from the incident angle of the radiation.
4. Due to the limit of the computation time, the reflections at the back sheet and the glass/air interface are calculated twice. After the second calculation, the remaining light on the backsheet area is considered lost. These losses account for around 0.6 % of the total incident light.

The radiant power that directly reaches the cell can be represented by:

$$P_{\text{cell}} = p_{\text{in}} A_{\text{cell}} \tag{3.2}$$

Here, A_{cell} is the cell area.

Ray tracing is used to calculate the radiant power that is reflected by the backsheet and reaches the solar cells. In the model, the full module is divided into unit elements, each with an area of 1 mm × 1 mm. Any unit element of the backsheet area scatters light into 3600 outgoing rays with a uniform separation of 6 degree azimuth angle and 3 degree polar angle.

The luminous flux of each ray is calculated by the following steps:

1.) The scattering angle (θ) and wavelength (λ) dependence of the normalized reflected radiant intensity $S_{\mathrm{n}}(\theta,\lambda)$ and the direct reflectance $r(\lambda)$ are determined experimentally, which will be described in Section 5.1.2.1. $S_{\mathrm{n}}(\theta,\lambda)$ is obtained from normalizing the measured signal at a certain angle to the largest measured signal value.

2.) The wave-length dependent irradiance at a certain direction and certain wavelength $S(\theta,\lambda)$ can be calculated by:

$$S(\theta,\lambda) = Ap_{\mathrm{in}}r(\lambda)\frac{S_{\mathrm{n}}(\theta,\lambda)}{\iint S_{\mathrm{n}}(\theta,\lambda)\sin(\theta)\,\mathrm{d}\varphi\mathrm{d}\theta} \tag{3.3}$$

Figure 3.9 shows a sketch of the situation described in equation 2. Here, A is the area of a unit element on the backsheet, θ is the angle between the scattered ray direction and the surface normal (polar angle) while φ is the azimuthal angle in the spherical coordinate system.

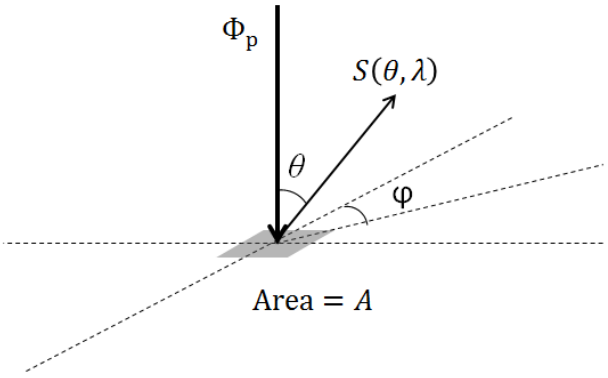

Figure 3.9: A sketch indicates the symbols in Equation 3.3.

The pathway of the scattered rays inside the module is described in Figure 3.10. If the incident angle of the ray is larger than the critical angle of total internal reflection, the ray is totally internally reflected. The refractive index of the PV module glass used in the experiments is kept fixed at 1.5 and independent of wavelength, thus the corres-

ponding critical angle is 41.8° [104]. If the incident angle is smaller than the critical angle, the reflectance and transmittance depend on the incident angle, and is calculated with Fresnel equations [104]. In this simulation light is regarded as unpolarised, containing an equal mix of the two polarization directions. Figure 3.10 shows a specific case in which one ray is scattered by the backsheet and reflected to the cell area. If the incident light reaches the module at a position (x_1, y_2), the coordinate (x_2, y_2) of the position where the reflected ray reaches is calculated by:

$$x_2 = x_1 + 2d\tan(\theta)\cos(\varphi) \tag{3.4}$$

$$y_2 = y_1 + 2d\tan(\theta)\sin(\varphi)$$

Here, d is the thickness of the front glass plus the front transparent lamination layer. The thickness of the rear lamination layer is assumed to be zero and cell and backsheet are at the same level.

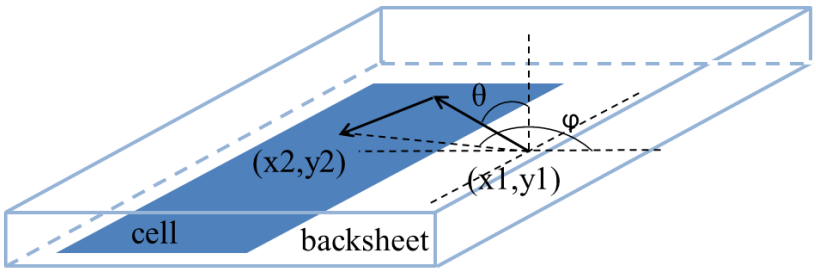

Figure 3.10: A 3D sketch of the light path within a c-Si PV module.

In the next step, the whole module is divided into 1 mm × 1 mm unit elements. If the backsheet area ranges from position (p_1, q_1) to (p_2, q_2), the total radiant power reflected from the backsheet area to the solar cell area P_b can be calculated as:

$$P_b = \int_{q_1}^{q_2}\int_{p_1}^{p_2}\int_0^{2\pi}\int_0^{\alpha} p_{\text{in}} R(\lambda) T(x_2, y_2) \frac{S_{\text{n}}(\theta,\lambda)\sin(\theta)}{\iint S_{\text{n}}(\theta,\lambda)\sin(\theta)\,\mathrm{d}\varphi\mathrm{d}\theta}\,\mathrm{d}\theta\,\mathrm{d}\varphi\,\mathrm{d}x\,\mathrm{d}y \tag{3.5}$$

Here, α is the critical angle, $R(\lambda)$ is the backsheet reflectance. Since only rays reaching the cell area add to the integration, a test function T is defined as a function of x_2, y_2 calculated from equation (3.5):

$T(x_2, y_2)$=1; when (x_2, y_2) is within area solar cell (3.6)

$T(x_2, y_2)$=0; when $(x_2, y_2)$is outside area solar cell

It should be noted that for a large-size c-Si PV module, $T(x_2, y_2)$ does not only consider one solar cell within the module. For the industrial size c-Si PV module composed of tens of solar cells, the test function is equal to 1 if (x_2, y_2) locates within any single solar cell of the module. As a consequence, Equation 3.4 can both be applied to a mini-module and an industrial size PV module.

In the next step, the short-circuit current contribution from the backsheet is calculated.

The total amount of radiant power received by a PV module can be written as:

$$P_{\text{total}} = P_{\text{cell}} + P_{\text{b}} \tag{3.7}$$

The relative increase in radiant power received by the solar cells due to reflection at the backsheet is:

$$Inc = \frac{P_{\text{b}}}{P_{\text{cell}}} \tag{3.8}$$

Since the solar cell does not utilize light of different wavelengths with the same efficiency, a better way to estimate the total increment on short-circuit current is to weight the result with the photon flux $\Phi_{\text{n}}(\lambda)$ of the solar spectrum and the external quantum efficiency $EQE(\lambda)$ of the used solar cell. The photon flux is defined as the number of photons incident on a surface per second and per unit area. Since the photon flux is linearly proportional to the radiation power at a single wavelength, and equation (3.7) can also be represented by

$$Inc(\lambda) = \frac{\phi_{\mathrm{n-backsheet}}(\lambda)}{\phi_{\mathrm{n-cell}}(\lambda)} \tag{3.9}$$

It follows that the collected carriers at a certain wavelength can be calculated by the product of the external quantum efficiency and the incident photon flux. Thus, the total short-circuit current increase ΔI can be calculated as follows:

$$\Delta I = \frac{\sum Inc(\lambda)\phi_{\mathrm{n}}(\lambda)EQE(\lambda)\Delta\lambda}{\sum \phi_{\mathrm{n}} EQE(\lambda)\,\Delta\lambda} \tag{3.10}$$

Here, $\phi_{\mathrm{n}}(\lambda)$ is the photon flux at a certain wavelength, which depends on the spectrum of the incident light. In this simulation, the AM 1.5 spectrum is used. Note that only the improved current generation due to scattering from the backsheet is taken into account. Other effects, like non-uniformity of insolation, are neglected in this work.

3.3.4 Optical model for calculating irradiance received by a tilted surface

In order to study the PV module behaviour under outdoor operating condition, it is important to evaluate the PV module performance on the system level. In order to calculate the radiation received by a PV module with arbitrary orientation, a method to calculate radiation received by a tilted surface is described. This method is not limited to c-Si PV modules but can be generalized to any kind of PV module. This method is used to evaluate different c-Si PV module configurations in Chapter 7. In the proposed method, both monofacial PV modules and bifacial-PV modules are considered. Similar methods have been used on bifacial modules [105, 106] and also PV modules with solar-tracking systems [107, 108].

The sun's position can be described by two angles: azimuth α_{sun} and altitude β_{sun}. These two angles of the sun during a whole year for any places in the world can be calculated by existing models [69]. The configuration of a tilted surface can also be described by two angles: tilting angle ω and azimuth angle α_{t}.

Assuming α_d is the difference between the azimuth angle of the sun and the azimuth angle of the surface: $\alpha_d = \alpha_{sun} - \alpha_t$, the solar incidence angle γ is the angle between the normal of the surface and the sun's rays, the amount of direct-beam solar radiation received by a tilted surface (S_{dir}) is calculated by:

$$S_{\mathrm{dir}} = DNI \times \cos(\gamma) \tag{3.11}$$

Since the angle between two vectors in a three dimensional space is calculated by:

$$\cos(\gamma) = \boldsymbol{a} \times \boldsymbol{b}/(|\boldsymbol{a}| \times |\boldsymbol{b}|) \tag{3.12}$$

The direct radiation received by the front side of the tilted surface can be calculated by:

$$S_{\mathrm{direct}}(front) = DNI \times \frac{-\cos(\alpha_d)\sin(\omega) + cos(\omega) \times \tan(\beta_{\mathrm{sun}})}{\sqrt{1 + \tan^2(\beta_{\mathrm{sun}})}} \tag{3.13}$$

Similarly, the direct radiation received by the rear side is calculated by:

$$S_{\mathrm{direct}}(rear) = DNI \times \frac{\cos(\alpha)\sin(\omega) - \cos(\omega) \times \tan(\beta_{sun})}{\sqrt{1 + \tan^2(\beta_{\mathrm{sun}})}} \tag{3.14}$$

Here, if the calculated radiation value is negative, the radiation received by that side is zero. At a certain time of a day, only one side of a tilted surface receives direct radiation.

In practice, reflection also has an influence on the radiation received by a tilted surface, which also needs to be taken into account. The reflection loss (R_{loss}) of the direct beam incidents to a tilted surface is a function of the incident angle γ [109]:

$$R_{loss}(\gamma) = 1 - [\frac{1 - \exp(-\cos\gamma\ /ar)}{1 - \exp(-1/ar)}] \tag{3.15}$$

ar is the angular loss coefficient. Typical ar values range from 0.16 to 0.17 for commercial c-Si wafer modules [109].

In the next step, radiation reflected from the sky and radiation reflected from the ground received by a tilted surface needs to be calculated, and a model by Tian *et al.* is used [110]. Diffuse radiation from the sky seen by a tilted surface is calculated by:

$$R_{\text{sky}} = H_{\text{diff}} \times svf \tag{3.16}$$

Here, *svf* is sky-view factor which is calculated by:

$$svf = (\pi - \omega)/\pi; \quad gvf = 1 - svf \tag{3.17}$$

Radiation reflected from the ground seen by a tilted surface is calculated by [105]:

$$R_{\text{ground}} = A \times (H_{\text{dir}} + H_{\text{diff}}) \times gvf \tag{3.18}$$

Here, *A* is ground albedo. Albedo is defined as the fraction of the solar irradiance reflected from the earth surface back into space, which depends on the reflectivity of the earth's surface. *gvf* is ground-view factor which is calculated by:

$$gvf = 1 - svf \tag{3.19}$$

At last, the total radiation received by a tilted surface (S_{total}) can be calculated based on Equations (3.10) to (3.19):

$$S_{\text{total}} = S_{\text{dir}} + H_{\text{diff}} \times svf + \text{A} \times (H_{\text{dir}} + H_{\text{diff}}) \times gvf - R_{loss} \tag{3.20}$$

.

4 Cell-interconnection resistive loss analysis for c-Si wafer based PV modules[1]

As described in Section 2.2.2, the cell-to-module loss is always a concern for c-Si wafer-based PV module manufacturers. The cell-interconnection resistive loss covers more than 90% of the total CTM resistive loss, which is very important for c-Si PV module optimization. This chapter focuses on the cell-interconnection resistive loss, and different problems related to this kind of loss are investigated.

Section 4.1 compares the interconnection resistive loss for solar cells with different metallization patterns. There are many existing reports focusing on the reduction of the cell-interconnection resistive loss [111-114]. However, established approaches assume an effectively one-dimensional (1D) current flow and do not take into account the 2D current flow on a fully metalized cell rear side. In Section 4.1 a refined method will be presented taking into account the 2D aspects of the current flow in the cells' metallization patterns. The commonly used 1D method for calculating the ribbon resistance is then corrected for 2D effects.

Section 4.2 compares the interconnection resistive loss for c-Si PV modules using full-size cells and halved cells. The method of calculating the output power increase from full-size cell PV module to halved-cell PV module is introduced.

Section 4.3 is based on the combination of the methods introduced in Section 4.1 and Section 4.2. A detailed comparison is made between I-V characteristics for full-size cell c-Si PV modules and halved-cell c-Si PV modules using monofacial and bifacial solar cells. Both simulation results and experimental results are provided for

[1] Section 4 is based on the publications: S. Guo, J.P. Singh, M. Peters, A.G. Aberle, T.M. Walsh, *"A quantitative analysis of photovoltaic modules using halved cells"*, International Journal of Photoenergy, 2013, 73937 and S. Guo, J.P. Singh, M. Peters, A.G. Aberle, J. Wong, "Two dimensional current flow in stringed PV cells and its influence on the cell-to-module resistive losses", *Solar Energy*, submitted.

verification. Further studies are extended to large-size c-Si PV modules regarding the influence of the short-circuit current of individual cells and the cell interconnection scheme.

4.1 Two-dimensional current flow for stringed solar cells

In a c-Si PV module, the current generated in a solar cell flows to the ribbons. The current transport through the ribbons causes resistive loss. Established methods for calculating this loss usually only consider the resistive loss on the ribbons and assume a linear increase or decrease in current flow [115-117]. However, in general, the current flow from cell to ribbon forms a 2D pattern, which depends on the metallization scheme of the solar cell front and rear surface. In this section a refined method is presented, taking into account the 2D aspects of the current flow in the cell's metallization patterns.

4.1.1 Influence of metallization pattern on the current flow through the ribbons

In this work, a network model implemented in Griddler [77] (introduced in Section 3.3.1) is used to simulate the current flow distribution within the metal pattern for a solar cell that is integrated into a PV module. Griddler was equipped to solve the voltage and current distributions in a solar cell with one resistive cell plane, instead of two coupled front and rear planes simultaneously. However, the simulator enables one to study the resistive losses in each cell plane as if they were independent. Thus two types of 6-inch-wide silicon wafer solar cell metallization patterns were simulated, one which featured an “H” pattern with 78 fingers which is representative of the front grid, and one which had full-area metal electrode which is representative of the rear cell plane. In the latter case, the solar cell sheet resistance was set equal to the aluminium sheet resistance (~10 mΩ/sq). Since in Griddler the shading from metal and optical generation can be decoupled, in all simulations the light-induced current density in the cell plane is set to be uniform and the integrated total is set

equal to the expected cell short-circuit current. In the simulation, mini-modules with either full-size cells or halved cells are modelled. All parameter values used in the simulation are listed in Table 4.1. The simulator solves the I-V characteristics of a mini-module. The current density and voltage distribution across the surface of the solar cell can also be obtained.

Table 4.1: The parameters used in the simulation of mini-modules using Griddler.

Parameter	Value
R_{emitter}	80 Ωcm^2
R_{M}	3 Ωcm^2
ρ_{c}	0.003 Ωcm^2
ρ_{r}	1.728×10^{-8} Ωm
F_{pitch}	1 mm
W_{busbar}	2 mm
W_{ribbon}	2 mm
h_{r}	20 μm
N_{bb}	3
J_{ph}	39.5 mA/cm^2

The surface potential distribution on the cell surface at maximum power point for a full-size cell mini-module is plotted in Figure 4.1. Figure 4.1(a) shows the surface potential for the cell with "H" metallization pattern, and Figure 4.1(b) shows the surface potential in the cell with full-area metallization pattern. The corresponding current flows inside the corresponding ribbon is plotted in Figure 4.2.

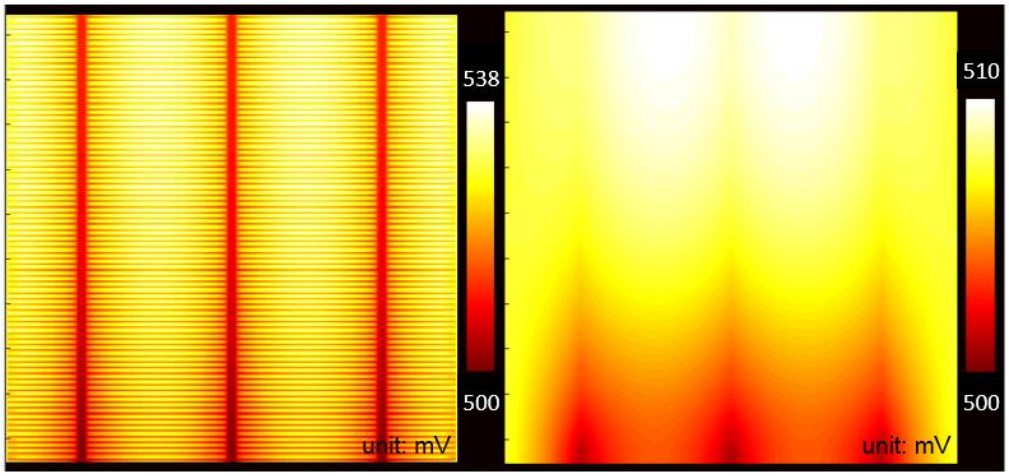

Figure 4.1: Surface potential distribution on the cell surface at maximum power point for solar cells with (a) finger-busbar metallization pattern and (b) full-area metallization pattern.

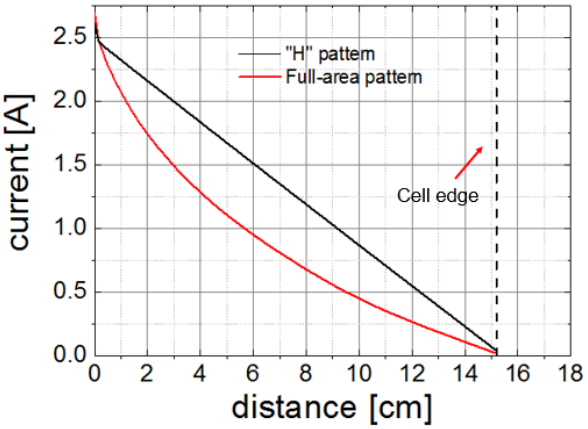

Figure 4.2: Current flow inside a ribbon at the maximum power point for solar cells with different front metallization patterns and ideal conductor on the rear side.

From Figure 4.1, the current flow in the solar cell can be inferred. Current flows according to the potential gradient, and for the "H" pattern the current flows mostly directly from the semiconductor to the nearest finger, then to the nearest busbar, and then along the corresponding front ribbon. As a consequence, the current flow along the ribbon increases linearly, as shown in Figure 4.2. In contrast, for the cell with full-area metal electrode, there is a significant component of current flowing along the high-conductance aluminium plane in parallel to the ribbons, which contributes in the ribbon current deviating from the simple linear dependence. However, the total current extracted from the end of each ribbon is the same for the two solar cells.

The simplified description by the conventional method for the full-area metal electrode leads to two major inaccuracies in the calculations of resistive power losses in the fully metallized cell rear plane. Firstly, the simplified picture overestimates the ribbon power loss and underestimates the rear aluminium metal power loss [6, 8], because it fails to capture the current division between these two conductors. Secondly, overall it overestimates the total power loss in the cell plane. The latter observation can be explained by the energy minimization principle: the correct current flow pattern must follow the "path of least resistance" and therefore leads to the minimum power loss, and conversely, any assumed current flow pattern must necessarily incur an overestimation in the dissipated power.

4.1.2 Corrected method for quantifying CTM resistive loss for monofacial cells

Based on the simulation results shown in 4.1.1, the metallization pattern affects the current flow within the ribbons. Thus, it can further influence the resistive power loss on ribbons. In this section, certain correction factors will be introduced to the conventional calculation method for monofacial cells, so that the influence of metallization pattern can be considered. Here, mini-modules are used for investigation. The behaviour of full-size PV modules can be extrapolated from the mini-module results, if string-interconnection is taken into account additionally. The mini-modules are composed either of one full-size solar cell (reference case) or two halved solar cells connected in series (shown in Figure 4.3. In this section, only the calculation method and the calculated correction factors will be shown. Further experimental results will be introduced in Section 4.2.3.

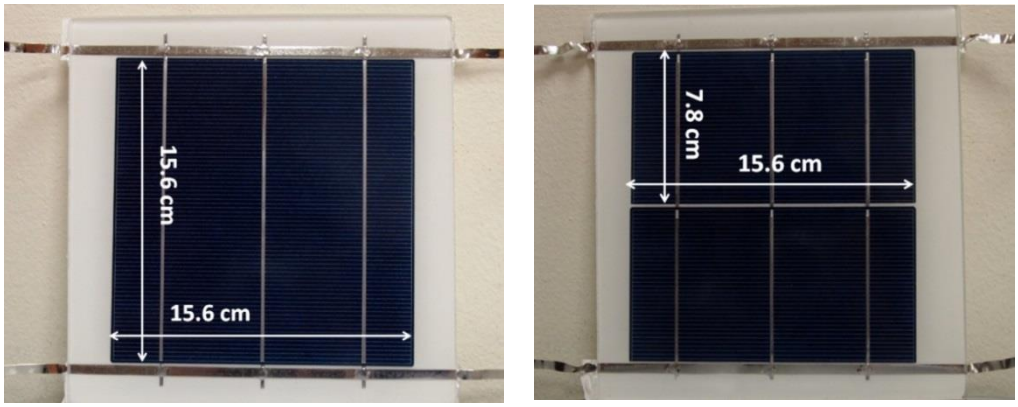

(a) (b)

Figure 4.3: Photographs of mini-modules using (a) full-size solar cells and (b) halved solar cells.

Based on [115], the total series resistance of a mini-module with a full-size cell $R_{mm(full)}$ is:

$$R_{\mathrm{mm}(full)} = R_{\mathrm{c}(full)} + R_{\mathrm{r}(full)}. \tag{4.1}$$

R_{c} is the total series resistance of the solar cell, and R_{r} is the series resistance of the ribbons, which is the sum of the front side and rear side ribbon resistance.

This equation can be well applied to bifacial solar cells. However, as already mentioned in 4.1.1, for a monofacial solar cell, the current transport through the aluminium sheet also induces additional resistive power loss, which is not considered in previous resistance calculation. In order to take this effect into account, the equation for monofacial cell needs to be corrected as follows:

$$R_{\mathrm{mm}(full)} = R_{\mathrm{c}(full)} + R_{\mathrm{r}(full)} + R_{\mathrm{m}(full)}. \tag{4.2}$$

Here, $R_{m(full)}$ refers to the effective resistance of the aluminium metal sheet on the rear side of the monofacial solar cell. As shown in [115], if the current flow through the ribbon increases or decreases linearly (as for the “H” pattern), the metal resistance can be calculated by:

$$R_{\mathrm{r}(full)} = R_{\mathrm{r-top}} + R_{\mathrm{r-rear}} = \frac{\rho L_{\mathrm{bb}}}{3N_{\mathrm{bb}}} + \frac{\rho L_{\mathrm{bb}}}{3N_{\mathrm{bb}}} = \frac{2\rho L_{\mathrm{bb}}}{3N_{\mathrm{bb}}}. \quad (4.3)$$

Here, $R_{\mathrm{r-front}}$ is the effective resistance of the front ribbons and $R_{\mathrm{r-rear}}$ is the effective resistance of the rear ribbons.

The metal sheet resistance, assuming the current flows in perpendicular to the ribbons, is given by:

$$R_{\mathrm{m}} = \frac{1}{3} R_{\mathrm{Al}} \left(\frac{L_{\mathrm{bb}}}{2N_{\mathrm{bb}}}\right)^2 \quad (4.4)$$

Here, R_{Al} is the sheet resistance of the aluminium sheet.

Both Equation 4.3 and 4.4 are based on the assumption that the current within the metal sheet takes the shortest path towards the ribbons. Based on the simulation result in 4.1.1, for a monofacial solar cell integrated into a PV module, the current within the rear ribbon doesn't decreases linearly. Also, the current doesn't flow perpendicularly towards the ribbons. Thus for a monofacial solar cell, in order to accommodate for the change in resistance of the full-area metallization, Equation 4.2 is suggested to be replaced by:

$$\begin{aligned} R_{\mathrm{mm}(full)} &= R_{\mathrm{c}(full)} + C_0 \cdot \left(R_{\mathrm{r}(full)} + R_{\mathrm{r}(metal\ sheet)}\right) \\ &= R_{\mathrm{c}(full)} + C_0 \cdot \left(\frac{2\rho L_{\mathrm{bb}}}{3N_{\mathrm{bb}}} + \frac{1}{3} R_{Al} \left(\frac{L_{\mathrm{bb}}}{2N_{\mathrm{bb}}}\right)^2\right) \end{aligned} \quad (4.5)$$

Here, C_0 is correction factor. To calculate this correction factor, it is noted that for a ribbon on the rear side, the total power loss is:

$$P_{\mathrm{loss-rear}} = \int_0^L (I(x))^2 r \mathrm{d}x, \quad (4.6)$$

where r is the ribbon resistance per unit length, with a unit of Ω/cm, L is the ribbon length (with unit of cm), and x is the current position along the ribbon, *I(x)* is the current at that position, which is obtained from the red line shown in Figure 4.2. C_0 is

then obtained by dividing the rigorous solution by the conventional solution for 1-sun maximum power point conditions:

$$C_0 = \frac{P_{\text{loss-top}} + P_{\text{loss-rear}} + P_{loss-Al}}{I_{\text{mpp}}^2\left(R_{\text{r}(full)} + R_{\text{m}}\right)} \tag{4.7}$$

Here, I_{mpp} is obtained from Griddler simulation, $P_{\text{loss-front}}$ is the power loss on the front side ribbon, which is calculated from $I_{\text{mpp}}^2 \times R_{\text{r-top}}$, $P_{\text{loss-rear}}$ is calculated using Griddler results and Equation 4.6, $P_{\text{loss-Al}}$ is the power loss on the rear aluminium metal sheet. Since the proportion of the power loss in the ribbons and power loss on the metal sheet can be calculated from Griddler, $P_{\text{loss-Al}}$ can be obtained.

Based on the results from Figure 4.2, for a 6 inch full-size monofacial solar cell with metal sheet resistance of 10 mΩ/sq and 3 busbars, the resistive power loss in the ribbons of a monofacial solar cell is 83% of the expected power loss calculated based on Equation 4.3.

Also from the network simulation, it is calculated that the resistive power loss on the aluminium metal sheet is 50% of the resistive power loss on the rear ribbons of this solar cell. The calculated power loss on the metal sheet is around 2.6 times the theoretical power loss calculated from Equation 4.4. The difference is mainly caused by the bending of the current flow path towards the end of the ribbons. The correction factor C_0 is calculated to be 0.94 for this solar cell. Furthermore, the same calculation is done for mini-module using corresponding halved cells. The percentages of the CTM resistive loss on each component (ribbons and metal sheet) are shown in Figure 4.4.

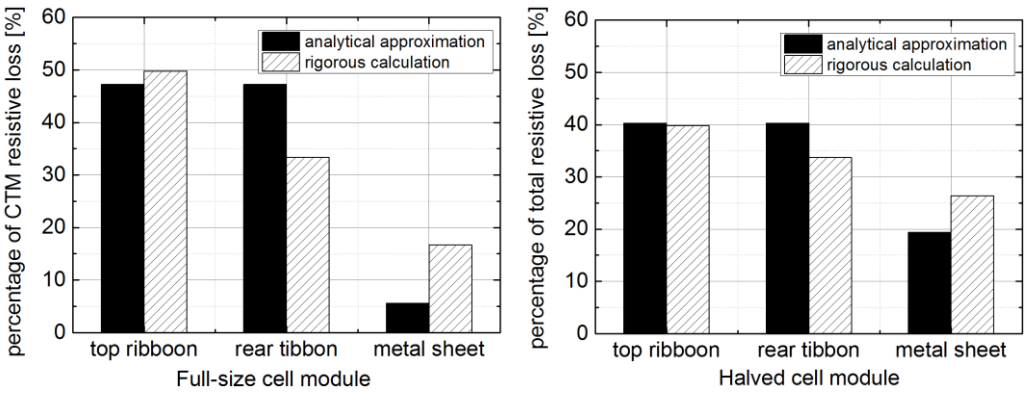

Figure 4.4: Percentages of CTM resistive loss on each component (ribbons and metal sheet) for a three-busbar solar cell with fully metallized rear side. The theoretical values refer to the percentage calculated from standard equations (Equations 4.3 and 4.4). The corrected values refer to the percentage calculated from the network simulation.

It can be seen from Figure 4.4 that the resistive loss in the rear ribbons is much less than the analytical approximation for a full-size cell module, and the resistive loss in the rear metal sheet is much higher than the analytical approximation. For the module with halved cells, the difference between the theoretical and corrected values gets smaller. In the next step, two factors' influence on the correction factor C_0 are investigated: (1) busbar number, (2) metal sheet resistance.

4.1.2.1 Influence of metal sheet resistance on correction factor C_0

In Section 4.1.1 a six inch solar cell with a rear metal sheet resistance of 10 mΩ/sq is taken as an as example. In the following it will be show how the correction factor changes for different metal sheet resistance. The results of the corresponding calculations is shown in Figure 4.5.

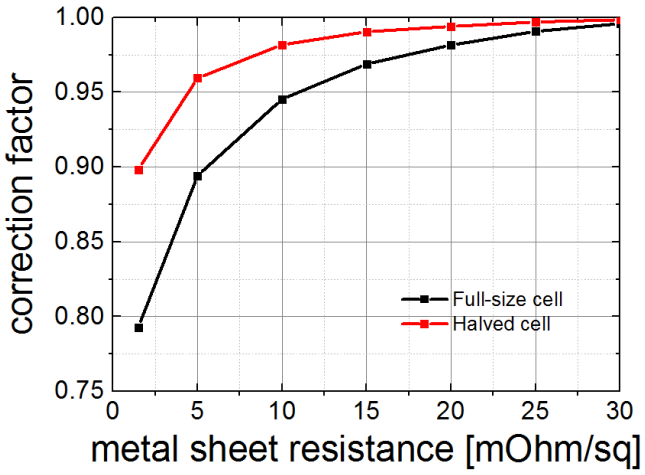

Figure 4.5: Influence of metal sheet resistance on the correction factor C_0 for full-size monofacial solar cell (6 inch) and halved cell with three busbars.

In Figure 4.5 it can be observed that the correction factor for the full-size cell is always smaller than the correction factor for the halved cell, i.e. the impact for the correction is always greater for full-size cells. Also, as the metal sheet resistance increases, the correction converges to one, which means that the current transport approaches the one assumed in the conventional model; i.e. current flow is predominantly perpendicular to the busbars. The correction factors shown in Figure 4.5 can then be used to accurately calculate the effective resistance. Using this approach, the network simulation is not necessary for simulating the I-V characteristics of mini-modules. In other words, by including the correction factors in the conventional analytical model, more accurate I-V characteristics of the mini-modules are easily obtained.

4.1.2.2 Influence of busbar number

In the next step the influence of the number of busbars on the correction factor and the power generation is investigated. Figure 4.6 shows the calculated correction factor C_0 for full-size and halved cells when the cell has two, three and four busbars. From Figure 4.6, it can be observed that the largest correction is required for a 2-busbar cell. For the 4-busbar cell, the correction factor is already very close to one, which means that nearly no correction is required for the analytical method. The correction factor

would rapidly converge to one if the busbar number is increased further. It should be noted that the theoretical value is based on the worst-case assumption that current flows perpendicularly to the busbars. Griddler simulations allow the free flow of the current in the whole surface plane, which reduces the effective resistance. Thus the correction factors are always smaller than one.

The simulations also showed that the power gain of a halved cell mini-module over a full-size cell mini-module is around 17% lower than the expected power gain calculated from the conventional method. For the 3-busbar case this number becomes 9%, and 3% for the 4-busbar case.

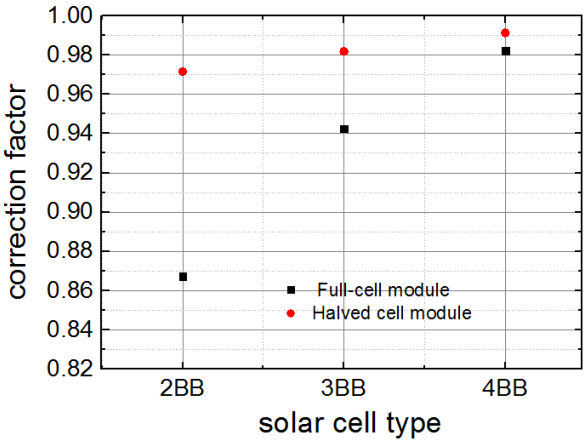

Figure 4.6: The calculated correction factor C_0 for full-size cell and halved cell when the cell has two busbars (2 BB), three busbars (3 BB) and four busbars (4 BB). The metal sheet resistance is fixed at 10 mΩ/sq in all cases.

4.2 Resistive loss analysis for full-size and halved-cell c-Si PV modules

In Section 4.1 the resistive loss analysis is done for c-Si PV modules using solar cells with different metallization patterns (monofacial and bifacial cells). In this section, resistive loss analysis is done for c-Si PV modules using full-size cells and halved cells. It is already known that using halved cells in a PV module is an effective method to reduce the CTM resistive loss, and this method has already been applied by some major PV manufacturers (Mitsubishi, BP Solar) in their commercial available

c-Si PV modules [11, 118]. In this section, the theory behind the output power increase for c-Si PV module using halved cells is explained.

In this analysis, still mini-module is used as an example to compare the full-size cell mini-module and the cut-cell mini module. The full-size cell mini-module is composed of one full-size cell. The cut cell mini-module is made by cutting the full-size cell into *n* pieces and connecting them in series. Since the resistivity of the bussing ribbons for string interconnection is very small, it makes no difference between mini-modules and large-size modules if the resistance of the bussing ribbons is neglected. Also, in this analysis it is assumed that the contact resistance between the busbars of the cell and the ribbons is negligible. Equation 4.2 represents the effective series resistance of a mini-module, however, the equation focuses on the series resistance within the cell region. Here the series resistance of the ribbons in the gap region (R_{rg}) is added to Equation 4.2, and the total series resistance of the mini-module (R_{mm}) with a full-size cell is then become

$$R_{\mathrm{mm}(full)} = R_{\mathrm{c}(full)} + R_{\mathrm{rc}(full)} + R_{\mathrm{rg}(full)}. \tag{4.8}$$

For the mini-module containing *n* cut cells connected in series, the series resistance can be calculated as follows:

Since the lumped series resistance of a solar cell is inversely proportional to the cell area, we have

$$R_{\mathrm{c}(cut)} = nR_{\mathrm{c}(full)}. \tag{4.9}$$

In the mini-module with n cut pieces of cells in series, the series resistances of the cells and ribbon add up, therefore

$$\begin{aligned} R_{\mathrm{mm}(cut)} &= n(R_{\mathrm{c}(cut)} + R_{\mathrm{rc}(cut)} + R_{\mathrm{rg}(cut)}) \\ &= n\left(nR_{\mathrm{c}(full)} + R_{\mathrm{rc}(cut)} + R_{\mathrm{rg}(cut)}\right) \\ &= n^2R_{\mathrm{c}(full)} + nR_{\mathrm{rc}(cut)} + nR_{\mathrm{rg}(cut)}. \end{aligned} \tag{4.10}$$

Here, $nR_{\mathrm{rg}(cut)}$ is the ribbon resistance of the gap averaged to each cut cell.

The effective current flowing through the mini-module with n pieces cells is 1/n times of that through the mini-module with full-size cells (*I*). Since the resistive power losses (P_{loss}) are equal to the square of the current multiplied by the total series resistance,

$$P_{\mathrm{loss}(full)} = I^2(R_{\mathrm{c}(full)} + R_{\mathrm{rc}(full)} + R_{\mathrm{rg}(full)}) \tag{4.11}$$

and

$$\begin{aligned} P_{\mathrm{loss}(cut)} &= \left(\frac{I}{n}\right)^2 (n^2 R_{\mathrm{c}(cut)} + nR_{\mathrm{rc}(cut)} + nR_{\mathrm{rg}(cut)}) \\ &= I^2(R_{\mathrm{c}(full)} + \frac{1}{n}R_{\mathrm{rc}(cut)} + \frac{1}{n}R_{\mathrm{rg}(cut)}) \end{aligned}. \tag{4.12}$$

It can be observed that for cut-cell modules, the cell resistive loss remains the same, and power gain is due to the reduced ribbon resistive loss. Thus, the power gain from full-size cell module to the cut-cell module can be calculated:

$$\begin{aligned} P_{\mathrm{gain}} &= P_{\mathrm{loss}(full)} - P_{\mathrm{loss}(cut)} \\ &= I^2\left(R_{\mathrm{r}(full)} - \frac{1}{n}R_{\mathrm{r}(cut)} + R_{\mathrm{rg}(full)} - \frac{1}{n}R_{\mathrm{rg}(cut)}\right). \end{aligned} \tag{4.13}$$

In the next step the relative power gain can be roughly estimated. If ignoring the resistance from the gaps for the two modules (which is relatively small) and assuming the effective ribbon resistance to be directly proportional to the ribbon length, the relation between the ribbon resistances for the two cells becomes:

$$R_{\mathrm{r}(cut)} = \frac{1}{n}R_{\mathrm{r}(full)}. \tag{4.14}$$

And the relative power loss reduction on ribbon can be calculated as:

$$P_{\text{relative}} = \frac{P_{\text{ribbon loss}(full)} - P_{\text{ribbon loss}(cut)}}{P_{\text{ribbon loss}(full)}} = 1 - \frac{1}{n^2} \quad (4.15)$$

Equation 4.15 shows that if the solar cell is cut into *n* stripes, the power loss in the ribbon scales with a factor $1/n^2$. Thus for a halved-cell PV module, the resistive power loss on ribbons will scale as 1/4 i.e. (75% reduction). It also shows that the power loss on ribbon can be further reduced if a cell is cut into more pieces. However, the benefit of power loss reduction gets smaller when *n* becomes larger. Also, cutting cells into more pieces might introduce more problems (mismatch effect and more additional gaps between the cells).

4.3 Combining the results: c-Si PV modules using full-size/halved monofacial/ bifacial silicon wafer solar cells

Based on the analysis introduced in Section 4.1 and Section 4.2, in this part the methods are used to compare the I-V characteristics for full-size cell c-Si PV modules and halved-cell c-Si PV modules using monofacial and bifacial solar cells. Due to the difference in metallization patterns, the power gain from replacing full-size solar cells by halved cells in a c-Si PV module is also different for PV modules using mono-facial cells and bifacial cells. In this section both simulation results and experimental results will be shown to investigate these problems.

4.3.1 Simulation results

Based on the calculated "correction factors" in Section 4.1.2, the effective ribbon resistance can be calculated for each type of mini-modules, and the corresponding I-V characteristics can be solved. The simulation is based on the circuit model for c-Si PV modules introduced in Section 3.3.2. Since the comparison is purely based on simulation, the I-V characteristics of both types of full-size cell mini-modules are set to be the same by adjusting the cell series resistance. The I-V characteristics of the

full-cell and halved-cell mini-modules with monofacial/bifacial solar cells are shown as Table 4.2.

From the simulation results, for both types of halved-cell mini-module, the short-circuit current is half of the full-size cell mini-module and the open-circuit voltage is twice of the full-size cell mini-module. PV modules using halved cells generally result in an increase in module fill factor and output power due to the reduced resistive losses. However, due to the different 2D current flow in different cell types, this increase is around 10% higher for PV modules using bifacial solar cells. This result shows the significance of my hypothesis.

Table 4.2: The simulated I-V characteristics and the used correction factors for full-size cell and halved-cell mini-modules using monofacial/bifacial cells.

	Mini-module with mono-facial cells			Mini-module with bifacial cells		
	Full-cell	Halved cell	Δ	Full-cell	Halved cell	Δ
Correction factor	0.945	0.998	N.A.	1.00	1.00	N.A.
I_{SC} [A]	9.00	4.50	0	9.00	4.50	0
V_{OC} [V]	0.63	1.26	0	0.63	1.26	0
FF [%]	76.9	78.6	+2.3%	76.9	78.9	+2.6%
P [W]	4.48	4.62	+2.3%	4.48	4.64	+2.6%

4.3.2 Experimental verification

In order to verify the simulation method, different types of mini-modules are fabricated experimentally. In this part, the simulation results are compared with experimental results for mini-modules using both monofacial and bifacial solar cells.

For mini-modules using monofacial solar cells, four samples of each type of modules are produced. The multi-Si wafer solar cells used to fabricate these modules were chosen from the same batch with cell efficiencies in the range of 17.2-17.4%. For

mini-modules using bifacial solar cells, the cell used were chosen from the same batch of n-type bifacial solar cells with cells with an efficiency of 18.8% and bifaciality of 0.96. A Q-switched, picosecond, frequency doubled Nd:YAG laser was used to cut the cells into half (Lumera SUPER RAPID, Lumera Laser, Germany). For both types of mini-modules, glass-cell-backsheet construction was used for better comparison. The equipment, materials and soldering conditions were the same for all samples during soldering and busbar connection processes. After that, all samples were laminated at the same time and under the same temperature conditions. The arrangement of half cells used generates an open-circuit voltage approximately equal to twice the full-size cell mini-module and a short-circuit current approximately equal to half of the full-size cell mini-module. To compare the halved-cell mini-modules and full-size cell mini-modules, all fabricated module samples were measured under standard test conditions (STC) using a steady-state super-class-A, solar simulator (SolSim 210, Aescusoft, Germany).

The photos of the produced mini-modules using monofacial solar cells have already been shown in Figure 4.3. Since the produced PV modules using bifacial solar cells also use glass-cell-backsheet construction, they look similar as PV modules using monofacial solar cells. The average I-V characteristics for each type of mini-modules are shown in Table 4.3 and Table 4.4. The simulation results are also included here for comparison. Since the halved-cell module contains two halved cells connected in series, its short-circuit current should be half and its open-circuit voltage should be double as compared to the mini-modules with full-size cell. In order to make the comparison clearer, in the table the scaled current and voltage values are shown for the halved-cell mini-modules. The simulation results are also included here for comparison.

Table 4.3: The simulated and measured current voltage characteristics of full-size cell and halved-cell mini-modules using monofacial solar cells.

Parameter	Simulation			Experiment		
	Full-cell module	Halved-cell module	Δ	Full-cell module	Halved-cell module	Δ Av.
I_{SC} [A] (scaled)	8.35	8.35	0	8.35±0.02	8.35±0.04	0
V_{OC} [V] (scaled)	0.620	0.620	0	0.620	0.620	0
FF [%]	77.5	78.9	+1.8%	77.6±0.3	78.9±0.2	+1.7%
P [W]	4.02	4.08	+1.8%	4.02±0.02	4.08±0.02	+1.7%

Table 4.4: The simulated and measured current voltage characteristics of full-size cell and halved-cell mini-modules using bifacial solar cells.

Parameter	Simulation			Experiment		
	Full-cell module	Halved-cell module	Δ	Full-cell module	Halved-cell module	Δ Av.
I_{sc} [A] (scaled)	9.77	9.77	0	9.77±0.01	9.78±0.01	+0.1 %
V_{oc} [V] (scaled)	0.640	0.640	0	0.640±0.00	0.640±0.005	0
Fill Factor [%]	74.3	76.0	+2.2 %	74.3±0.1	75.8±0.1	+2.0 %
Power [W]	4.65	4.75	+2.2 %	4.64±0.02	4.74±0.01	+2.2 %

From Table 4.3, for *monofacial* cells, both experiment and simulation show that the short-circuit current of halved-cell mini-modules is exactly half of that of the full-cell mini-modules, while the open-circuit voltage is exactly two times that of the full-cell mini-modules. The fill factor gain calculated from the analytical 1D model is 2.1% (relative). However, this value is calculated to be 1.8% (relative) based on the improved model, which is much closer to the experimental results.

For mini-modules using *bifacial* halved cells (shown in Table4.4), the open-circuit voltage is still exactly two times that of the full-cell mini-modules, while the short-circuit current is slightly (0.1%) higher than half of that of the full-cell mini-modules. This is most likely due to the wide gap region between the two halved cells, which leads to extra current due to scattering of light from the gap region towards the solar cells [119]. The simulated fill factor increase is 2.2%, which is also very close to the experimental result (2.0%).

It can be observed that the simulation results agree very well with the measurement results. The comparison between the simulation and measurement results proves the validity of the simulation method and the validation of the theory described in Section 4.1 and 4.2.

4.3.3 Extension to large-size modules by simulation

In Section 4.2.2, mini-modules are investigated as examples. Though the features of the large-size c-Si PV modules can be represented by mini-modules, there is still a need to investigate the industrial size c-Si PV modules in terms of the interconnection schemes and real PV module characteristics. In this part, two problems related to large-size c-Si PV modules are investigated. In part 4.2.3.1, the influence of the cell short-circuit current on the benefits for c-Si PV module using halved cells is investigated. In part 4.2.3.2, the different interconnection schemes for the industrial size c-Si PV modules using halved cells are investigate and compared. Since the basic features are all the same for c-Si PV module using bifacial cells and monofacial cells, in this part c-Si PV modules using monofacial cells are investigated as an example.

4.3.3.1 Influence of cell short-circuit current on the benefits for halved-cell c-Si PV modules

In Section 4.3.2, monofacial solar cells within the same batch of efficiencies are used in the experiment. However, in today's PV market, the properties for solar cells of

different types and brands have large variation. For some high-efficiency solar cells, the short-circuit current can easily reach to more than 40 mA/cm^2. Since the resistive loss on ribbons for c-Si PV modules depends largely on the cell operating current, in this part the simulation is extended to large-size modules. The influence of cell short-circuit current on the resistive loss for full-size and halved-cell large-size modules is investigated. In this investigation, a large-size module is composed of solar cells connected in series, and monofacial cells are taken as example. In Figure 4.7 the power loss on ribbon for halved and full-size cell large-size PV modules with various cell short-circuit current density values is plotted. The ribbon size and sheet resistance are the same as the parameters provided in Table 4.1.

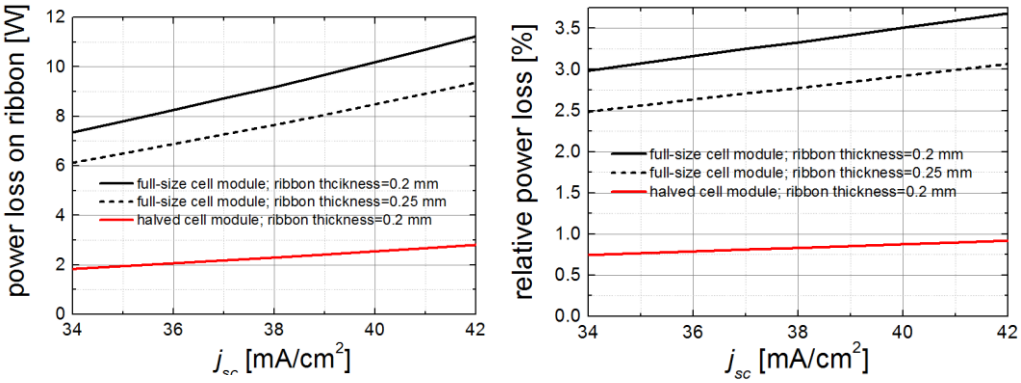

(a) (b)

Figure 4.7: (a) Power loss on ribbon for halved and full-size cell large-size c-Si PV modules with various short-circuit current density values. (b) The relative power loss is the percentage of resistive power loss on ribbon among the total output power. Two values of ribbon thickness are considered.

From Figure 4.7 it can be observed that when the short-circuit current density increases, the power loss on ribbon also increases. However, the increase on power loss is much larger for full-size cell module than for halved-cell modules. This means that using halved-cell PV modules instead of full-size cell PV modules can help in keeping the power loss on ribbon within a small range for solar cells with higher short-circuit current density. In Figure 4.7, this method is also compared with another method -reducing the resistive loss by increasing the ribbon thickness. The dashed

line shows the power loss when the ribbon thickness is increased from 0.2 to 0.25 mm. Since resistive loss varies linearly with ribbon thickness for particular cell j_{sc}, the reduction in power loss on ribbon is much lower as compared with using halved-cell modules. Also, increasing the thickness of the ribbons leads to increase in cell breakage during manufacturing. Thus compared with increasing the ribbon thickness, using halved cells is a more effective method to reduce cell-to-module resistive loss for high j_{sc} (high efficiency) solar cells.

4.3.3.2 Influence of interconnection scheme on the halved-cell c-Si PV modules

In order to take configurations of large-size modules into account, further investigations for large-size c-Si PV modules are performed. The investigated module structures are shown in Figure 4.8:

(a) shows the structure of a traditional large-size module composed of 60 full-size cells,

(b) shows the structure of a large-size module composed of 120 halved cells connected in series and

(c) shows the structure of a large-size module composed of 144 halved cells connected in both parallel and series.

Among all three module configurations, Type-c is similar to the commercially available c-Si PV modules of Mitsubishi. Type-b and type-c represent two different methods to connect halved cells in a module. For the type-b module, all cells are connected in series, thus the current of this module is half of the current of the type-a module, and the voltage is two times of the voltage of the type-a module. The type-c module contains 12 strings and each string contains 12 halved cells. Each two strings are connected in parallel first, and then pairs of strings are connected in series. The short-circuit current of this module is the same as the short-circuit current of the type-a module.

Simulations were performed to compare the three module types. The main differences between the different module types are the total length of bussing ribbons and the current flowing through these ribbons. For this reason, the power loss caused by bussing ribbons has to be taken into consideration. In the simulations, the relationship of fill factor and effective series resistance were calculated from the diode equation. Then the effective series resistance of each type of module was calculated. After that, the fill factor of each type of module corresponding to its effective series resistance was obtained from the fill factor - effective resistance relationship. The resistance of the ribbon in the gaps between the two halves of a halved solar cell was also taken into account.

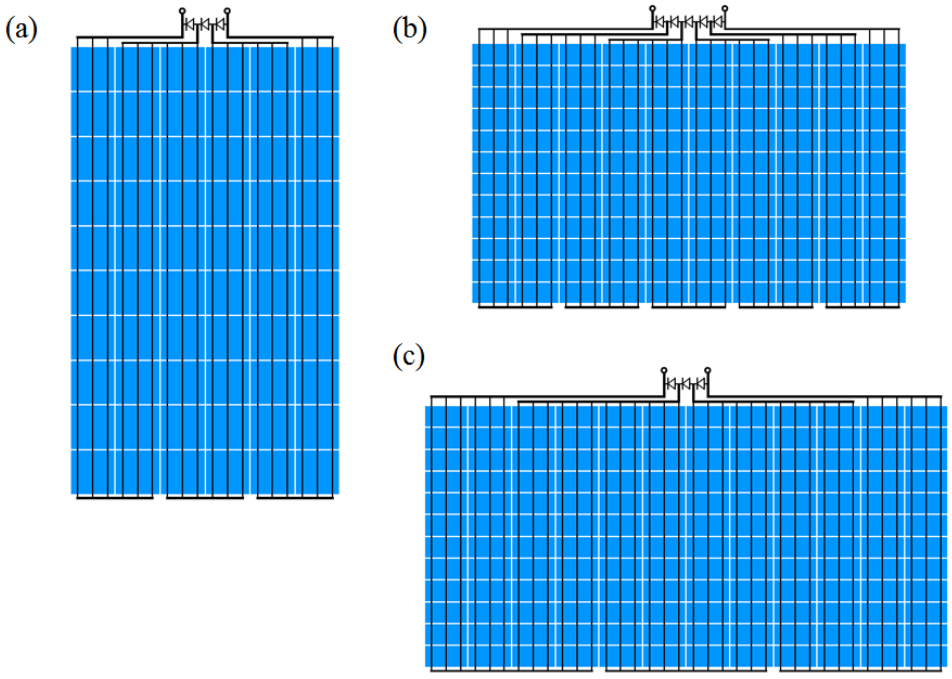

Figure 4.8: (a) Traditional large-size module composed of 60 full-size cells connected in series; (b) Large-size module composed of 120 halved cells connected in series; (c) Large-size module composed of 144 halved cells connected both in parallel and in series.

The fill factors corresponding to each type of PV module were calculated according to their effective series resistance which includes effective cell resistance, ribbon resistance, bussing ribbon resistance and junction-box cable resistance. The simulation results are shown in Table 4.5. The parameters used are: bussing ribbon

width: 5 mm; bussing ribbon thickness: 0.3 mm; cable cross-section area: 4 mm^2; cable length: 1 m. All parameters were obtained experimentally.

From the simulation results it can be observed that the fill factors of the two types of halved-cell modules [(b) and (c)] are both higher than the traditional full-size cell module (a). The fill factors of the type-b and type-c modules are different because of the different interconnection schemes. There are mainly two reasons: Firstly, the total length of bussing ribbons of a type-c module is longer than that of a type-b module. Secondly, for a type-b module, the current flowing through all the ribbons is half of the current of the traditional full-size type-a module.

Table 4.5: Fill factors and total length of bussing ribbon of the three types of large-size PV modules.

Module type	(a) Full-size cell module	(b) Halved-cell module	(c) Halved-cell module
Total effective series resistance [Ωcm^2]	1.15	0.75	0.80
Fill Factor [%]	77.1	79.1	78.8
Total length of bussing ribbon [cm]	218.4	384.8	468
Ribbon length per full size wafer [cm]	3.64	6.41	6.50

However, type-c module includes parallel connection of strings, some bussing ribbons have the same current as the type-a module, and the higher current causes a higher power loss. Thus in real application, type-b modules might be a better choice, since the series resistance loss at the module level for this type of module is the lowest. What's more, from the system level, type-b module will always result in lower resistive losses in all the cable connections, since this kind of module has less current output than the traditional full-size cell module at the same power level. Parallel connection among module strings can be realised at the system level to achieve the required current and voltage for a standard inverter.

In all, if taking all the reduction of resistive loss from ribbons, the power generation efficiency can be improved by 2.1 % relative for type-b module and 2.6 % relative for type-c module. This means that, for a standard 240 W industrial c-Si PV module with full-size solar cells, the power increase can be as much as 6.3 W if it is made into a halved-cell module. For high-efficiency solar cells, the output power improvement is even larger.

4.4 Conclusions for Chapter 4

This chapter provides detailed theoretical and experimental analysis of cell-interconnection resistive loss for c-Si PV modules. Section 4.1 introduced detailed resistive loss analysis considering the 2D current flow for the cell connected within a c-Si PV module. When analysing the CTM resistive loss for c-Si PV modules, pervious methods were mainly based on 1D model and only consider the resistive loss in the ribbons. However, from this work it was found that the previous models are not enough to describe the resistive loss for PV module using monofacial solar cells. Results from 2D network simulation showed that the resistive power loss within the ribbon on the rear side is only around 67% of the value calculated from the analytical model for a standard solar cell with three busbars. The power loss on the rear metal sheet, which is usually ignored in the calculation, covers around 17% of the total CTM resistive loss, which cannot really be ignored. In order to improve the existing models, certain correction factors are added to the existing equations calculating the effective cell-to-module resistance for monofacial cells.

Section 4.2 compared the interconnection resistive loss for c-Si PV modules using full-size cells and halved cells. The method of calculating the output power increase from full-size cell PV module to halved-cell PV module was introduced. It was found that if each solar cell within a c-Si PV module is cut into *n* stripes, the power loss in the ribbon scales with a factor $1/n^2$. Thus halved-cell c-Si PV module generally reduce the resistive power loss by 75%.

Section 4.3 presented a combination effect of the results shown in Section 4.1 and 4.2. In Section 4.2, a detailed comparison was made between I-V characteristics for full-size cell c-Si PV modules and halved-cell c-Si PV modules using monofacial and bifacial solar cells. It was shown that halved-cell mini-modules using bifacial and monofacial cells have an average FF increase of 2.0% and 1.7 % respectively, compared to the full-size cell mini-modules. Simulation results agree quite well with experimental results for both types of mini-modules, and the results get much closer to the experimental results than the results obtained from the commonly used analytical model. At last, the investigation was extended to industrial size c-Si PV modules. It was found that comparing with increasing ribbon thickness, c-Si PV modules using halved cells are more effective in keeping the CTM resistive loss within a small range for high j_{sc} (high efficiency) solar cells. Also, by comparing the different PV module configurations, it is better to only include series connection in the halved-cell PV module, since this configuration induces the minimum resistive loss.

In all, this chapter provides a detailed resistive loss analysis of interconnected solar cells in c-Si PV module from different aspects. The method provided in this work can be very useful for design and optimization for different kinds of c-Si PV modules.

5 Optical analysis of c-Si wafer based PV modules[2]

Chapter 4 focused mainly on the resistive power loss analysis and corresponding optimization for a c-Si PV module. Besides reducing the resistive loss, a c-Si PV module can also be optimized by reducing the optical loss and increasing the optical gain. One important factor that affects the total amount of light received by the solar cells is the light scattering effect in the inactive areas of a PV module (such as the backsheet region in the gaps between neighbouring solar cells). In this chapter the influence of the backsheet and other components on the short-circuit current of a c-Si wafer based PV module is investigated theoretically and experimentally.

In Section 5.1, an investigation is presented about the optical gain from light which is first scattered at the backsheet area and then reflected at the glass-air interface of the front cover. Different characterization methods are used to quantitatively predict the influence of the backsheet on the short-circuit current of a c-Si PV module based on the method introduced in Section 3.3.3. Both specular and angular dependent scattering properties of the backsheet are included and studied. In Section 5.2, it is shown in a case study that c-Si PV modules using halved cells generate a higher current than c-Si PV modules using full-size cells, due to light reflected by the increased backsheet area close to the cells. Simulation results are verified with experimental results in this section. Section 5.3 provides an analysis of area-related losses in an industrial-size c-Si PV module based on the method introduced in Section 5.1. The concept of "effective area coverage" is introduced. The effective area analysis is done for different components of a c-Si PV module, including the backsheet, fingers, ribbons

[2] Sections 5.1 and 5.2 are based on the publication: S. Guo, J. Schneider, F. Lu, H. Hanifi, M. Turek, M. Dyrba, I.M. Peters, T.M. Walsh, *"Investigation of the short-circuit current increase for PV modules using halved silicon wafer solar cells"*, Solar Energy Materials and Solar Cells **133**, 240-247 (2015).

Section 5.3 is based on the publication: M. Peters, S. Guo, Z. Liu, *"Full loss analysis for a multicrystalline silicon wafer solar cell PV module at short-circuit conditions"*, Progress in Photovoltaics: Research and Applications, 2015, DOI: 10.1002/pip.2593.

and frame. Through this analysis, the optical loss on different parts of a c-Si PV module is quantitatively determined. Also, further strategies of improving the optical performance of a c-Si PV module are proposed.

5.1 Influence of backsheet region on short-circuit current of a c-Si PV module

5.1.1 Introduction

In this chapter, optical simulation is used to study the optical characteristics of a c-Si PV module. Optical studies for c-Si PV modules have also been done before to solve different problems [37, 120, 121]. The present work mainly focuses on the amount of light that is scattered by the cell-free backsheet area and reflected to the solar cell area, that is the light trapping effect induced by the backsheet area (as shown in Figure 5.1). The influence of the exposed backsheet area on the short-circuit current of a c-Si PV module was investigated before [101-103, 122, 123]. Experimental results, however, were only provided in Refs. [122, 123]. Ray tracing simulation was used in Refs. [101, 102], however, the light spectrum and the angular dependent scattering properties were not considered in those papers, and only mini-modules were investigated in Ref. [101]. References [103, 124] include the wavelength dependent reflectance of the backsheet in the model, and they also indicate that merely considering the spectral dependence is not sufficient for a complete description.

The present work is based on the methods introduced in Section 3.3.3. Since most of the previous works only considered mini-modules, in this work both mini-modules and large-size modules are investigated. Also, both specular and angular scattering properties for the backsheet are considered, which is an improvement of the existing models. From the obtained results it is found that mainly three factors influence the light-trapping effect of the exposed backsheet area:

- the geometry of the exposed backsheet area,
- the spectral backscattering properties of the backsheet,
- the angular backscattering properties of the backsheet.

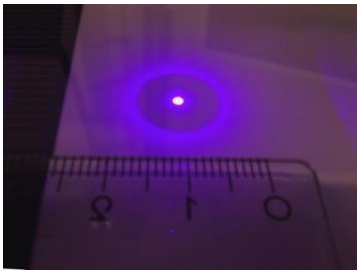

(a)

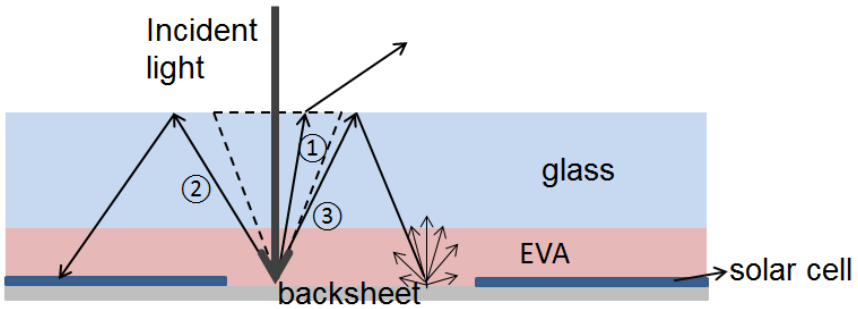

(b)

Figure 5.1: (a) A photograph showing the scattering of light by the exposed backsheet of a c-Si wafer PV module. (b) Light paths within a PV module. Light incident on the exposed backsheet area between two neighbouring solar cells is randomly scattered. ①②③ are three paths taken as examples from all the scattered light paths. The scattered light within the escape cone (shown as path ①) will escape from the module and is lost. The scattered light outside the escape cone can either be reflected back towards the cell-covered area (②) or towards the backsheet area (③). The light that is reflected towards the backsheet area will be scattered once more.

To verify and test the proposed method, light beam induced current (LBIC) measurements are used to characterize the amount of light scattered at the exposed backsheet and utilized by the solar cells. The spectral and angular backscattering properties of the exposed backsheet are taken into account by fitting the LBIC measurement results at different wavelengths.

5.1.2 Measured scattering properties of the exposed backsheet

According to Section 3.3.3, in order to make an accurate prediction of the amount of the trapped light, the properties of the exposed backsheet need to be taken into account. An ideal diffuse reflecting surface shows the same brightness, independent of the angle from which it is seen. This behaviour is commonly referred to as Lambertian scattering [125] and corresponds to a cosine dependence of the scattering irradiance and the scattering angle. However, for a non-ideal diffusely reflecting

surface, like backsheets used in PV modules, the irradiance of the reflected radiation can have an almost arbitrary angular dependence that can significantly deviate from that of a Lambertian scatterer. In order to make accurate predictions, the actual angular scattering properties of the backsheet are taken into account. The scattering properties can be characterized in two ways: (1) Measuring the backsheet reflectance and angular-dependent scattering intensity. (2) Measuring the LBIC signal of the backsheet area. In this part, both methods are used in the calculation. The methods will be described in detail later in this chapter.

5.1.2.1 Reflectance and angular-dependent scattering intensity measurement

In Section 3.3.3, $r(\lambda)$ and $S_{\mathrm{n}}(\theta,\lambda)$ were used to calculate the wavelength dependent irradiance reflected into a certain direction (Equation 3.5). For the measurement of $r(\lambda)$, the hemispheric reflection spectra of the backsheet against air and in a mini-module are recorded with a UV/Vis/NIR spectrophotometer (Perkin Elmer, Lambda 1050) coupled to a 150 mm integrating sphere, using a tungsten halogen lamp and a deuterium lamp as light sources and a photomultiplier (Hamamatsu, R6872) and a Peltier-cooled InGaAs detector for signal detection. The reflectance of the backsheet in air is higher than the reflectance of the backsheet in a mini-module, as shown in Figure 5.3(b). Based on the diffuse reflection of the backsheet, a large amount of light scattered/reflected under large angles is trapped inside the mini-module by total internal reflection. The backscattering properties of the backsheet $S_{\mathrm{n}}(\theta,\lambda)$ can be quantified by measuring the angle-dependent backscattering luminous intensity. The setup of the measurement is shown in Figure 5.2(a). In this measurement, the light source is an AlGaInP laser diode (HL6312G/13G). The beam is guided parallel to a projection plane. The distance between the camera and the backsheet is very short. At the right end of the projection plane the laser beam illuminates the backsheet. The backsheet is positioned orthogonally to the projection plane and the laser beam. The intensity distribution of the scattered light is mapped onto the projection plane, as

shown in Figure 5.2(b). It is assumed that the scattering property is independent of the azimuth angle, thus the projected normalized scattered light intensity is captured by a CCD camera at one azimuth angle and different polar angle. The angle distribution is calculated by dividing the measured light intensity at a certain angle by the largest measured light intensity. Figure 5.3(a) shows the measured and normalized angular dependent intensity for the wavelength of 632 nm and 785 nm.

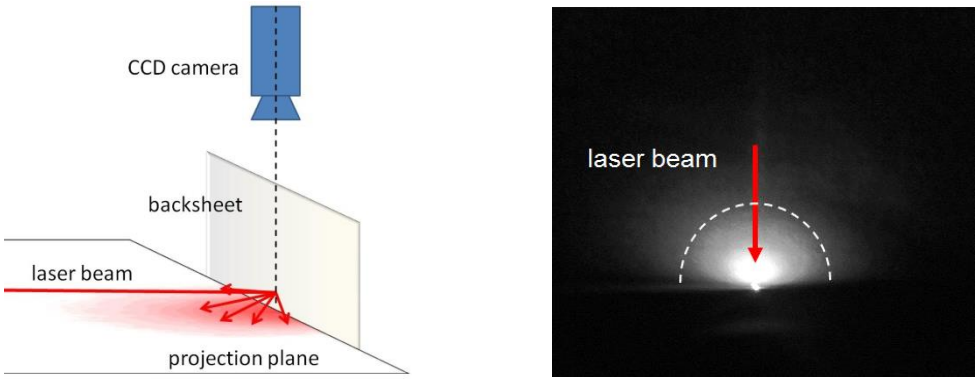

(a) (b)

Figure 5.2: (a) The measurement setup and (b) the camera image of the intensity distribution on the projection plane of laser light scattered at the backsheet. The dashed line shows the central axis of the CCD camera.

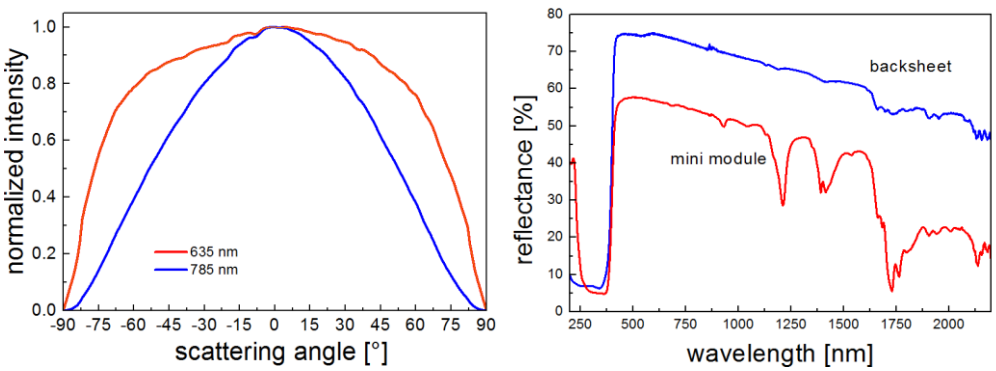

(a) (b)

Figure 5.3: (a) Normalized angular dependent intensity of the backsheet used in the experiment under two different wavelengths and (b) its spectral reflectance before (blue) and after (red) encapsulation in a mini-module.

5.1.2.2 LBIC measurements

The backscattering properties of the backsheet can also be tested indirectly by light beam induced current (LBIC) measurements. LBIC is a useful characterization method for solar cells [126, 127] and PV modules [128, 129] and can be used to investigate various aspects of PV devices. In an LBIC measurement, the optical beam scans the test sample and the generated short-circuit current is measured as a function of the illuminated position. In the present case, a test sample (mini-module) is prepared that involves all materials to be used in a large-area c-Si PV module. In the performed measurements, the laser beam is slightly convergent (the convergence angle is 2°), and the focus is in the solar cell/backsheet plane, with a diameter of less than 200 µm. Using the method introduced in the previous section, the short-circuit current contribution from the exposed backsheet area of any c-Si PV module with known geometry and layout can be determined for a given optical spectrum. In order to verify the proposed method, an LBIC measurement is performed on a mini-module and compared with the simulation results. The comparison will be shown in Section 5.1.3.

5.1.3 Results

5.1.3.1 Comparison of LBIC simulation and measurement results

The simulation method for calculating the backsheet-induced current gain has already been introduced in Section 3.3.3. In order to verify the method, LBIC measurements are performed and compared to the simulation results. The wavelength used in these LBIC measurements is 650 nm, which is very close to the wavelength used for the angle-dependent scattering intensity measurement (635 nm). The LBIC image of the measured mini-module is shown in Figure 5.4(a). The measured short-circuit currents were normalized by the maximum short-circuit current measured in the active cell area (i.e., semiconductor area between the front grid fingers), giving local LBIC

signals in the 0 - 1 range. [Remark: In Fig. 5.4(a) all currents above 0.4 are shown in one colour, to better reveal the current distribution in the periphery of the solar cell.]

$$I_{\mathrm{n}} = \frac{I_{\mathrm{meas}}}{I_{\mathrm{max}}}. \tag{5.1}$$

Here, I_{meas} is the measured LBIC current at a certain position of the PV module, while I_{max} is the maximum measured LBIC signal (measured in the active cell region between the front grid fingers).

The LBIC measurement is then repeated by simulation. The glass and encapsulant used in the PV module produced in the experiment are assumed to have a refractive index of 1.5 and no parasitic absorption in the spectral range of interest. The total internal reflection at the glass/air interface is a key factor for the light trapping effect of a solar module, and the critical angle is 41.8° [104] for a glass refractive index of 1.5. The thickness of the front glass pane is 3.0 mm, while the EVA layer is 0.5 mm thick. Since this part of the thesis only focuses on the influence of the exposed back-sheet area on the short-circuit current of the mini module, the cell's front metalli-zation is not considered in the simulation. Also, the influence from the ribbons in the backsheet area is ignored. The simulation results are shown in Figure 5.4(b).

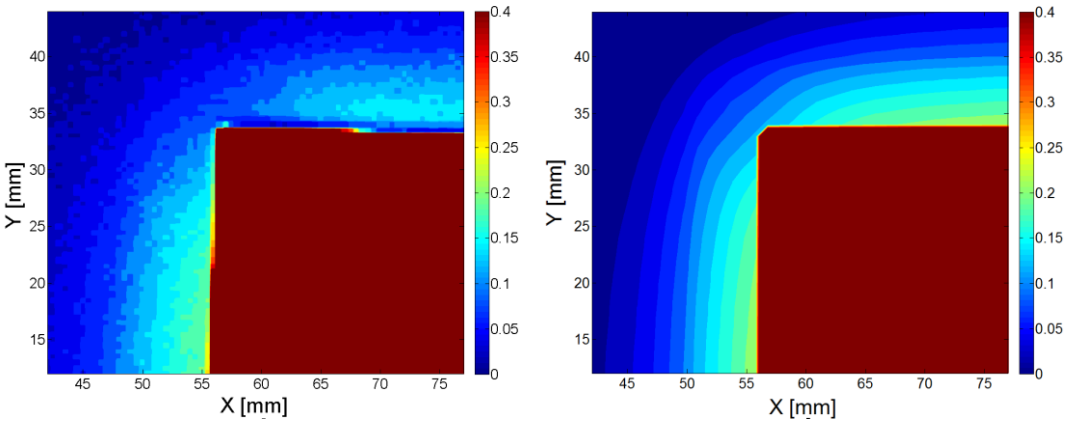

(a) (b)

Figure 5.4: (a) Measured and (b) simulated LBIC signals for one corner region of a c-Si mini-module. LBIC signals larger than 0.4 are shown in one colour (dark red), to better reveal the LBIC signal distribution in the cell periphery.

It can be seen that the simulation result generally agrees with the measurements. In the backsheet area along the edge of the solar cell, both simulation and measurement show about 20% collection efficiency for incident light. Furthermore, experiment and simulation both show that the collection efficiency decreases more rapidly near the corner region of the solar cell.

5.1.3.2 Spectral dependence of backscattering

In the previous LBIC measurement, only a single wavelength was considered. In order to investigate the spectral characteristics of the scattering properties of the backsheet, several LBIC measurements were performed, using three lasers with different wavelengths. In these measurements, the laser beam scans a straight line on a mini-module (shown in 5.5(a)). The collected short-circuit current is measured along this line. The normalized short-circuit currents for three different wavelengths are shown in Figure 5.5(b). It can be observed that the scattering properties of the backsheet depend on the wavelength of the incident light. The measured short-circuit current is largest for a wavelength of 650 nm, and drops for wavelengths of 405 nm and 960 nm. In order to better compare simulated and measured results, the simulation results for the three wavelengths are also shown in the figure (solid lines). From the simulations, it can be seen that mainly two factors influence the fraction of collected light coming from the backsheet:

- The backsheet reflectance at a certain wavelength.
- The shape of the angular scattering intensity.

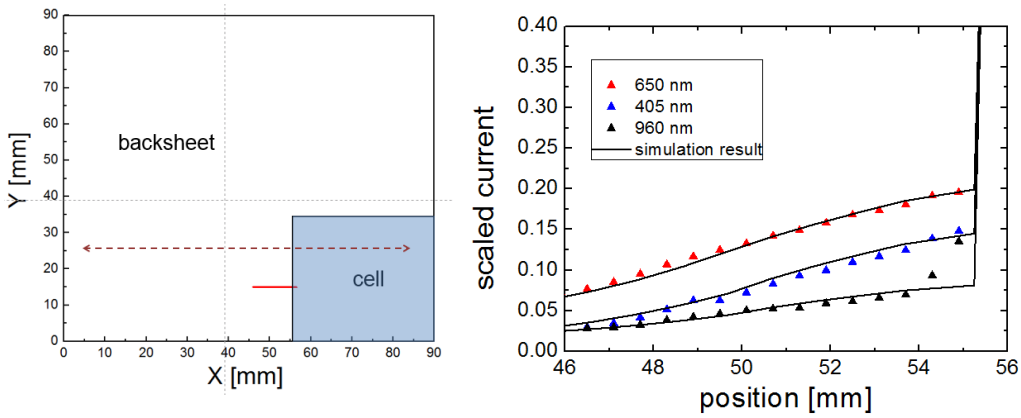

(a) (b)

Figure 5.5: (a) Sketch showing the measured line scan (red line) on the mini-module. (b) Comparison of the line-scan LBIC measurement result and the simulation result for three wavelengths. For the wavelengths of 650 nm and 960 nm, the reflectance of the exposed backsheet is used to fit the LBIC measurement results.

The main reason for the reduced collection of 405-nm light in the cell periphery is the low reflectance of the exposed backsheet region for short-wavelength light (as indicated in Figure 5.3(b). Also from Figure 5.3(b), for 960-nm light, the reflectance doesn't decrease by as much as the measured LBIC signal. Thus the difference is due to the angular signature of the backsheet, which can be deduced from Figure 5.3(a). In the presented simulation, this effect can be taken into account either by using the angle dependent back scattering data at this wavelength or by using an effective reflectance while using the same angular distribution as for the shorter wavelength in Equation 3.5 for long wavelengths. Since these wavelengths is not available in our angle-dependent scattering measurement, the second method is used in the simulation. For 405 nm and 960 nm, the effective reflectance used is 0.540 and 0.303. It can be observed that the experimental LBIC curves can be fitted well for 405 nm and 650 nm. For the wavelength of 960 nm, the simulation result still fits very well with the measured result, except for distances of less than 1 mm from the edge of the solar cell. The described effect might result in an overestimation of the simulated current. However, the affected area is small (~1 mm wide stripe along the cell edge), the EQE in the long-wavelength range is decreasing, and the number of solar photons in this

wavelength range is calculated to be within 1.6%, thus the overestimation can be ignored.

5.1.4 Conclusions for Section 5.1

In Section 5.1, different characterization methods were introduced and used to study the light trapping effect of the exposed backsheet region in a c-Si PV module based on the method introduced in Section 3.3.3. The developed method is an extended version of similar methods previously reported in the literature. The LBIC simulation and measurement results were shown and compared. Improvements of the developed model are: (1) the large-size PV module was considered in the model. (2) Instead of treating the exposed backsheet as a Lambertian surface and assuming that the back-scattering property is independent of the wavelength, the spectrum and angular back-scattering properties of the backsheet were taken into account by combining simulations with LBIC measurements. Using this method, the contribution from the backsheet area on the short-circuit current for any c-Si wafer based PV module with certain geometry and layout can be precisely determined, which can be very useful when optimizing the optical and electrical design of a c-Si PV module.

5.2 C-Si PV module using halved cells: a case study

5.2.1 PV module setup

It is already known from Chapter 4 that by using halved cells instead of standard full-size c-Si cells, the CTM resistive loss can be noticeably reduced. In this section, the investigation is extended towards the optical properties of two large-size c-Si PV modules: one with full-size cells and one with halved solar cells. PV modules are investigated theoretically but also experimentally fabricated and characterized for verification. In this part it will be shown that, in addition to an improved fill factor, c-Si PV modules using halved cells also generate a higher current under the following boundary conditions:

- The two kinds of PV module use the same number of full-size c-Si wafer solar cells.
- The two kinds of PV module have exactly the same module size.
- Due to practical reasons there is a minimum distance between neighbouring solar cells, which always results in a certain gap (at least 2-3 mm) between the cells within a c-Si PV module.

The setups of the investigated large-size c-Si PV modules are introduced in this part. Both PV modules using full-size cells and PV modules using halved cells are investigated. For the full-cell PV module, there are 72 full-size cells connected in series (the same as the type-b module shown in Figure 4.8). For the halved-cell PV module, there are 144 halved cells connected in both series and parallel. For the full-cell module, the spacing between two columns of the cells is 3 mm and the spacing between two rows is 5 mm, corresponding to state-of-the-art c-Si PV modules. It will be shown later that by optimizing these distances, the current in these modules can be significantly improved. The pattern of the full-cell module is shown in Figure 5.6(a). For the halved-cell module, two different types (type a and type b) are investigated. For the type-a module (Figure 5.6(b)), the spacing between the cells is exactly the same as in the full-cell module. For the type-b module (Figure 5.6(c)), the spacing between the cells is expanded in order to make better use of the spacing between the halved cells. Since there must be a certain distance from the cell edge to the module edge, the spacing between two columns of the cells is set to be 5 mm and the spacing between two rows is set to be 7 mm. As indicated in Figure 5.7, the edge backsheet area is the distance between the cell edge and the module edge, which is indicated as X1, X2, Y1, Y2 in the graph. For all these modules, the module sizes are exactly the same. Due to the different design of the modules, the four parameters are different, which are indicated in Table 5.1.

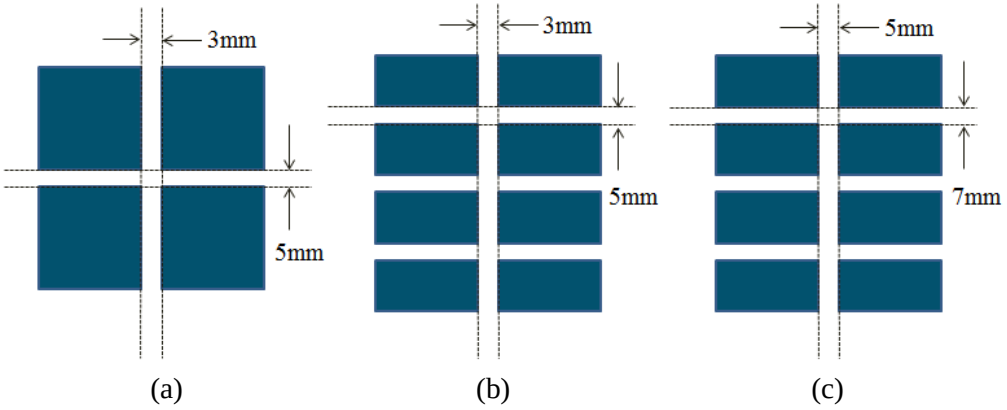

Figure 5.6: A symmetry part of the large-size modules investigated in this work. (a) Standard full-cell module, (b) Halved-cell module with the same spacing as the full-cell module (type a), (c) Halved-cell module with optimized cell spacing (type b).

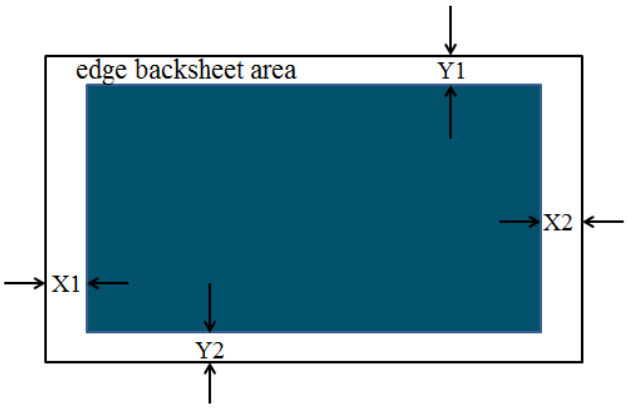

Figure 5.7: Sketch of a large-size c-Si PV module.

Table 5.1: Design parameters for different types of large-size c-Si PV modules.

Parameter	X1 (mm)	X2 (mm)	Y1 (mm)	Y2 (mm)
Full-cell module	30.0	65.0	69.5	69.5
Halved-cell module, type a	47.5	47.5	54.5	54.5
Halved-cell module, type b	36.5	36.5	54.5	54.5

5.2.2 Comparison between simulation and experimental results

In my simulation, the influence of all the factors mentioned in Section 5.2.1 are taken into consideration, including the gaps between the cells and the edge backsheet area.

The simulated current-voltage characteristics for each type of PV module are shown in Table 5.2.

Table 5.2: Simulation results for each type of large-size c-Si PV module investigated in this work.

Module type	I_{sc}[A]	V_{oc} [V]	FF	Power [W]
Full-cell	9.08	46.0	75.5 %	315.3
Type a	9.22	46.0	76.6 %	324.9
Type b	9.34	46.0	76.6 %	329.1
ΔType-a/Full	+1.56 %	+0	+1.46 %	+3.04 %
ΔType-b/Full	+2.88 %	+0	+1.46 %	+4.40 %

Further simulations also show that if the spacing between the cells of the full-cell module is expanded so that the full-cell module has exactly the same edge area as the halved-cell modules (the full-cell module has 5 mm gap in X direction and 7 mm×11/5 = 15.4 mm gap in Y direction), the short-circuit current of the module is still 0.9% lower than that of the halved-cell module.

Experimentally, the standard full-cell module and the type-b halved-cell module with the optimized design are fabricated and compared. The photos of the two modules are shown in Figure 5.8. Figure 5.9. and Table 5.3 show the measured I-V characteristics of the two modules.

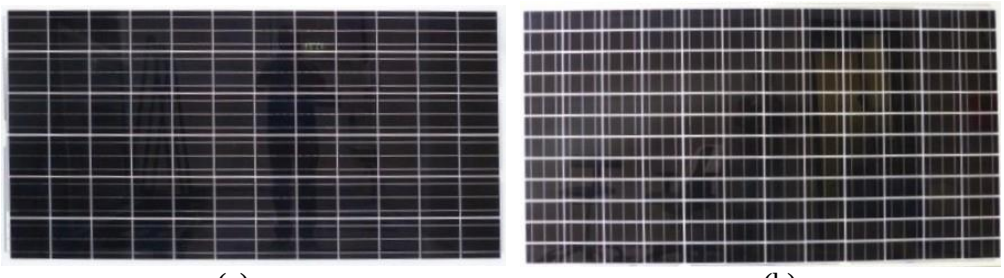

(a) (b)

Figure 5.8: Photographs of the two modules. (a) The PV module using standard full-size cells. (b) The PV module using halved cells with an optimized design.

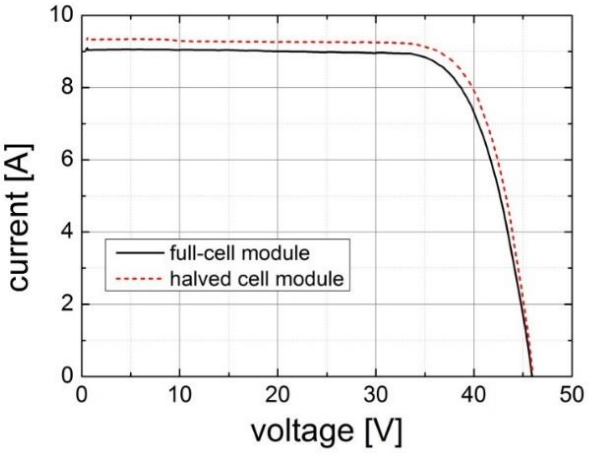

Figure 5.9: The measured one-Sun I-V curves of the two fabricated PV modules.

Table 5.3: The one-Sun I-V characteristics of both full-cell modules and type-b halved-cell modules from the measurement results.

Module type	I_{sc} [A]	V_{oc} [V]	FF	Power [W]
Full cell	9.08	46.0	75.5 %	315.3
Halved cell, type b	9.36	46.0	76.6 %	329.8
ΔHalf/Full	+3.08 %	+0	+1.46 %	+4.60 %

From Table 5.3, the total power gain of the halved-cell module compared to the full-cell large-size PV module is 4.60%. Around 32% of this gain comes from the reduced resistive losses of the halved-cell module, while about 68% of the increase results from the additional optical gain. The experimental short-circuit current increase is 3.08%, which is slightly larger than the simulation result (2.88%). The reason for this will be discussed in Section 5.2.3.

5.2.3 Spectrum influence and model accuracy

In order to take the light spectrum into account, the spectrum is divided into six wavelength intervals in the simulation. Wavelengths below 320 nm are ignored, since the reflectance of the backsheet is very low at these wavelengths, see Figure 5.3(b). For each wavelength interval, the LBIC measurement is done for the central wave-

length, and the spectral and angular dependent properties of the backsheet are considered by combining the simulation results with the LBIC measurement. The AM 1.5G solar spectrum [64] is used in the calculation. Optical absorption in the module's front glass sheet is ignored. The average relative short-circuit current increase for each wavelength is shown in Table 5.4. Also, the initial collected carrier density by the full-cell module at each wavelength and the increased amount induced by the backsheet area for the halved-cell module is shown in Figure 5.10. Taking the solar spectrum and the external quantum efficiency of the cells into account, the calculated difference in the short-circuit current between the two modules is 2.88% (0.28 A) [using Equation (3.10)]. Within the uncertainties of 6%, this value agrees with the experimental result of 3.08% (0.26 A). A part of the difference is attributed to the described overestimation of the collected current for long wavelengths (due to the angular signature of the backsheet). Another reason that may lead to the inaccuracy of the result is that in this simulation, the result is a weighted value by six single wavelengths, which cannot exactly represent the whole spectrum.

Table 5.4: The average simulated relative short-circuit current increase from full-cell module to halved-cell module for five wavelength intervals.

Wavelength interval [nm]	320-450	450-580	580-710	710-840	840-970	970-1110
Photon flux [$m^{-2}s^{-1}$]	2.34×10^{18}	4.272×10^{18}	4.435×10^{18}	4.209×10^{18}	4.197×10^{18}	3.402×10^{18}
EQE	84.9%	97.9%	98.2%	96.6%	95.7%	89.6%
I_{sc} increase	2.51%	3.36%	3.36%	3.25%	2.62%	1.65%

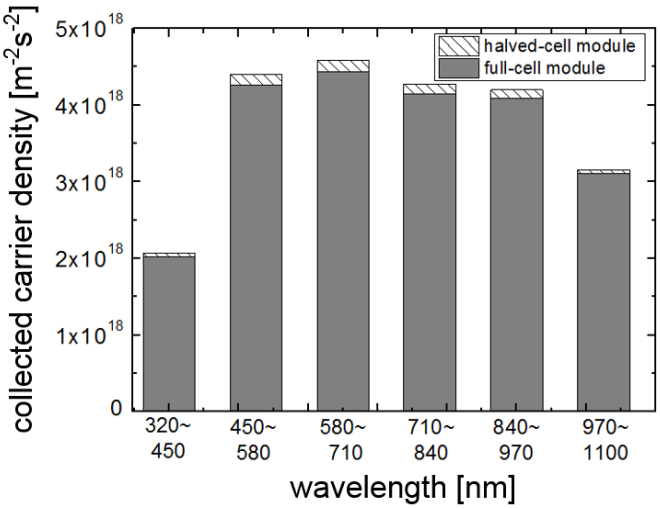

Figure 5.10: The simulated collected carrier density of a halved-cell module and a full-cell module, for the solar spectrum described in the main text.

5.2.4 Conclusions for Section 5.2

In Section 5.2, a study was presented to determine the influence of the exposed back-sheet region on the short-circuit current of a c-Si wafer based PV module theoretically and experimentally.

From the simulations it was found that, if the spacing between the cells is the same for the two investigated module types (halved cells vs. full cells), the current increases by 1.56% (relative) for the halved-cell module. If the spacing is further optimized for the halved-cell module, the current increase can reach up to 2.88%. Experimentally, a standard full-size cell module and a halved-cell module with optimized cell spacing were fabricated. The short-circuit current increased by 3.08% (from 9.08 to 9.36 A) when going from full-size cells to halved cells, which was well predicted by the simulation result of 2.88% (from 9.08 to 9.34 A). The PV module power output increased by 4.60% (315.3 W to 329.8 W). The additional output power increase came from the fill factor gain, which was discussed in Chapter 4.

Concerning costs, the only additional cost for the halved-cell PV module comes from the laser cutting process. However, it is easy to minimize this kind of cost during mass production. The number of standard solar cells, EVA, glass and backsheet size

are equal in both cases, which induces no additional cost for the halved-cell PV module. Thus, it is assumed that the cost increase for the production of halved cells will be insignificant and that the calculated gain of 4.60% will directly translate into an increased return of investment.

In this section it was experimentally confirmed that large-size c-Si PV modules using halved cells have higher electric power output than standard modules, due to an improved fill factor and an improved short-circuit current, whereby the majority of the power gain is due to the increased current resulting from the superior optical performance.

5.3 Area related optical loss analysis for c-Si PV modules

In Section 5.1, a method was introduced to quantitatively determine the light trapping effect induced by the exposed backsheet area of a c-Si PV module. In this section, the method is used to perform a full area-related loss analysis for a c-Si PV module. This is important since, besides the active solar cell (semiconductor) area, the entire area of a c-Si PV module also comprises nominally inactive areas (the metal fingers and ribbons, the exposed backsheet area and the frame) that contribute to some extent to the module's short-circuit current. Based on the results of Section 5.1, light reaching the exposed backsheet area can be scattered back and then reach the cell area. Thus these 'inactive areas' actually may not be totally inactive due to the light trapping effect. It is therefore necessary to look into the different areas of the PV module and perform a full area-related optical loss analysis for a c-Si PV module, so that its optical properties can be further optimized.

5.3.1 Method of calculating effective area coverage

The following analysis is based on a standard industrial-size c-Si PV module, the configuration of which is shown in Figure 5.11. In the analysis this PV module is divided into five areas: (1) active solar cell area; (2) area covered by the metal fingers;

(3) area covered by the ribbons; (4) area covered by the exposed backsheet; (5) area covered by the frame. If there is no light trapping effect, light reaching those inactive areas (2-5) is totally lost and the analysis can be done only according to the pure area of each component. However, due to the light trapping effect (as analysed for the exposed backsheet area in Section 5.1), the light losses of the inactive areas reduce and some of these photons reach the active area of the module. As a consequence, it is necessary to do an "effective area coverage" analysis of the whole module and evaluate the real optical effect for each component.

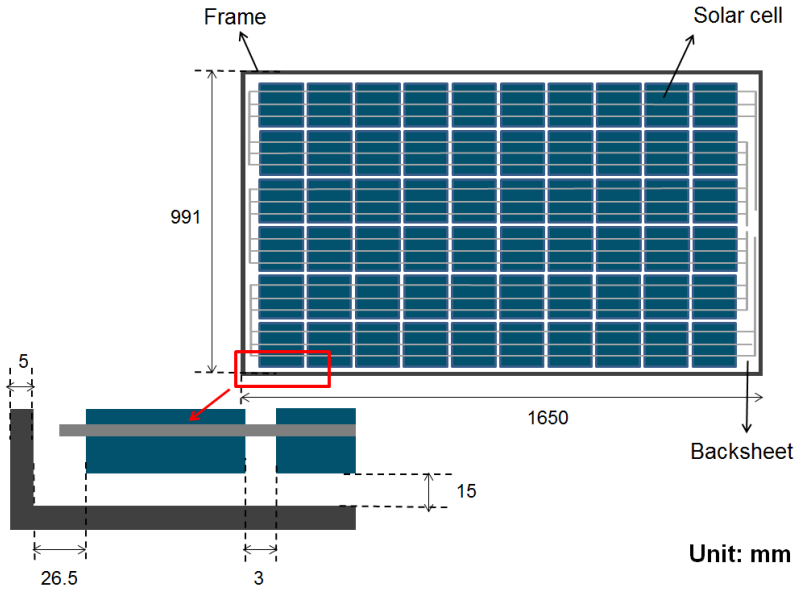

Figure 5.11: Sketch of a c-Si PV module. In this sketch the size of the different areas of the module is indicated. The active solar cell area (1) accounts for 83.7% of the total area. The active area is different from the total area covered with solar cells, as parts of the solar cell are covered by ribbons (2, 2.6% of total area) and metal fingers (3, 3% of total area). Additionally, the module has some exposed backsheet area (4, 9.1% of total area) and a frame (5, 1.6% of total area).

In this analysis, the effective area A_{eff} is used to represent the contribution to current loss for the inactive areas and current generation for the active area. Thus, due to light-trapping effect, A_{eff} should be smaller than the actual percentage area for those inactive areas and larger than the actual area for the active area. As a consequence, the effective area represents the fraction of a module that contributes to current

generation or current loss. Taking the exposed backsheet area as an example, the calculation is done as follows:

Based on Section 5.1, it is possible to calculate the percentage of photons that reaches any position of the exposed backsheet area and reflected to the cell area. Assuming this percentage is $f(x, y)$, which depends on the position of the backsheet within a PV module, the total percentage of the light that reaches the backsheet area and is then reflected to the cell area can be calculated by an integration over the whole exposed backsheet area within the PV module:

$$F = \frac{\int_0^A f(x,y)\mathrm{d}A}{A} \tag{5.2}$$

Here, A is defined as the total exposed backsheet area.

Let's assume the actual percentage area of the exposed backsheet is A_p, which is equal to 9.1% for the case shown in Figure 5.11. As a consequence, the effective percentage area is reduced to:

$$A_\mathrm{eff} = A_\mathrm{p} \times (1 - F) \tag{5.3}$$

In this analysis, white-painted ribbons are considered and Lambertian scattering is assumed on the ribbons. For the metal fingers, the effect of finger narrowing was investigated before [38, 130], and the results show that the finger narrowing is within the 45% to 55% range. Thus, in this study, the finger narrowing effect is assumed to be 50%.

5.3.2 Results

Based on the method and assumptions introduced in Section 5.3.1, the actual percentage area and effective percentage area are calculated for each part of the PV module. The results are shown in Table 5.5.

Table 5.5: Summary of the area related losses.

Components	Actual area coverage (%)	Effective area coverage (%)	Area ratio (%)
Active solar cell	83.7	87.7	105
Ribbons	2.6	1.5	56
Fingers	3.0	1.5	50
Exposed backsheet	9.1	7.7	85
Frame	1.6	1.6	100

From the results shown in Table 5.5, for the ribbons, fingers and the exposed backsheet, the effective area coverage reduces. In contrast, for the active solar cell area, the effective area coverage increases. The light intensity reaching the active area is increased by around 5% due to the light trapping effects occurring via the metal fingers, the ribbons and the exposed backsheet. For the exposed backsheet area, it is calculated that 15% of the light reaching this area will end up in the cell area. Thus the effective area of the exposed backsheet is reduced to 7.7% from 9.1% (actual area percentage). This means that, for the exposed backsheet area, around 15% of the total incident light is scattered and reflected to the active solar cell area, which is mainly contributed by the exposed backsheet in the cell gaps. For the fingers and ribbons, around 50% of the light incident in these areas will reach the active cell area.

It is calculated that the PV module investigated in this case contains 83.7% of active area and 16.3% of inactive area. However, due to light trapping effect, it is calculated that 87.7% of the incident light reaches the active area, and only 12.3% of the light is lost in the inactive area. These values indicate the effectiveness of a c-Si PV module to capture the light arriving in the inactive area. The light trapping properties of c-Si PV modules can probably be further improved according to this analysis.

5.3.3 Conclusions of Section 5.3

In this section, a detailed area-related optical loss analysis was performed for a c-Si PV module. The effective area coverage for different components of a c-Si PV module (active cell area, exposed backsheet area, metal area, and frame) was calculated. It was found that, due to a light trapping effect, the effective active solar cell area increases by around 5% compared to the actual solar cell area. The reason is a reduction of the effective coverage for ribbons, metal fingers and the exposed back-sheet. The results obtained from the analysis provide ideas for further improving the c-Si PV module power output. For the inactive parts (ribbons, fingers and exposed backsheet), it is necessary to enhance the light trapping effect. Possible methods can be improving the diffuse properties for these components and improve the light trapping effect. Also, the gap size between the cells within a c-Si PV module can be further optimized so that the cell area receives the most amount of scattered light from the exposed backsheet. As a consequence, by the area-related loss analysis presented in this section, the current loss of a c-Si PV module can be better under-stood and the optical properties of a c-Si PV module can be further optimized.

6 Mismatch analysis of c-Si wafer based PV modules

As already mentioned in Chapter 2, mismatch loss is an important factor affecting the performance of a c-Si PV module. In this chapter, two studies related to the mismatch problems of c-Si PV modules are presented. In Section 6.1, the mismatch effect caused by partial shading was investigated for a standard c-Si PV module. The influence of bypass diodes is included in the study. It was found that the bypass diode configuration strongly affects the output power of a c-Si PV module under a moving shadow. Based on this effect, a case study was performed for a virtual PV system in West Virginia, US, in which the relation between the row-to-row distance and the performance factor of the PV system is evaluated for c-Si PV modules with different bypass diode configurations. From the results, the yearly energy yield of the PV system was found to be strongly affected by the bypass diode configuration when considering the inter-row shading. In Section 6.2, the influence of the mismatch effect on the spectral response (SR) of a c-Si PV module as investigated. It was found that the spectral response of a c-Si PV module under SR measurement conditions can be very different from the SR under STC. Results show that both the shunt resistances of the individual solar cells and the bypass diode configuration have an influence on the measured SR of a c-Si PV module.

6.1 Partial shading analysis of c-Si PV modules[3]

Today's grid-connected PV systems are frequently mounted on building roofs, facades, or generally in urban environments, where partial shading can occur regularly [131]. Even for PV systems in the field, there is still a possibility of partial shading coming from clouds or inter-row shading [132, 133]. Under partial shading conditions, mismatch effects occur, which strongly affect the current generation of a

[3] Section 6.1 is based on the publication: S. Guo, T.M. Walsh, A.G. Aberle, M. Peters, *"Analysing partial shading of PV modules by circuit modelling"*, Proc. 38th IEEE Photovoltaic Specialists Conference, 2012, 002957-002960

c-Si PV module. To reduce losses due to partial shading, typically bypass diodes are used. However, the module behaviour will then be more complex because the bypass diode can introduce a second power peak in the lower voltage region. Thus, it is important to evaluate the module behaviour under these conditions.

Some work was already done on the investigation of partial shading effects on c-Si PV modules [134-137]. In Ref. [138], the electrical effects of partial shading of a PV array were analysed by a PV system design and simulation tool called PVsyst. This study showed that the electrical shading effect depends on both the number of cells in each string and the number of strings in parallel. In Ref. [139] the bypass diode configuration of c-Si PV modules was studied by constructing an equivalent circuit in the PSpice environment. In Ref. [131], a MATLAB-based model was used to study the effects of partial shading on the PV array characteristics. It was concluded that the array configuration significantly affects the maximum available power under partial shading conditions. However, past publications mainly focused on the partial shading effects under fixed shading conditions and didn't consider the movement of a shadow. However, in reality, the shadows caused by passing clouds, nearby buildings or trees usually move predominantly in a certain direction during a given period of time. This section introduces a reliable method to model the c-Si PV module behaviour under a moving shadow.

6.1.1 Modelling a c-Si PV module under shading condition

In this work, circuit modelling is used to model partial shading of a c-Si PV module. The model is constructed in LTSpice according to the method described in Section 3.3.2. In today's PV market, most of the c-Si wafer based PV modules consist of 60 solar cells connected in series. One common method to equip the PV module with bypass diodes (Figure 6.1(a)) employs a three bypass diode configuration. In this work this method is compared to another easily realizable method which employs

five bypass diodes (Figure 6.1(b)). Computer based models of PV modules with both bypass diode configurations are implemented and the corresponding PV module behaviour under partial shading conditions are compared. In order to model the module behaviour under a moving shadow, the current source of each cell in the simulation was set to be time-dependent. When a shadow passes across a solar cell, the shaded area of the cell changes with time, thus the photocurrent of this cell is calculated by:

$$I_{\mathrm{ph}}(t) = j_{\mathrm{ph}}\left(A_{\mathrm{cell}} - \int \dot{A}_{\mathrm{shade}}(t)dt\right) + T^{*}J_{\mathrm{L0}} \int \dot{A}_{\mathrm{shade}}(t)dt, \tag{6.1}$$

where I_{ph} is the photocurrent of a solar cell, A_{cell} is the total area of a solar cell, $\dot{A}_{\mathrm{shade}}(t)$ is the shading velocity at a certain time, which depends on the cell position and T^{*} is the shadow transmittance.

By using Equation 6.1, the relation between photocurrent and time for each solar cell in the module can be obtained and implemented into the time-dependent current source. Using this approach, the c-Si PV module behaviour depending on time can be calculated, using a nonlinear transient analysis provided by the software.

6.1.2 Results and analysis

6.1.2.1 Behaviour of c-Si PV modules with different bypass diode configurations

In this section, two modules with different bypass diode configurations (shown in Figure 6.1 (a) and (b)) are compared. While the module with three bypass diodes has 20 solar cells per string, the module with five bypass diodes consists of five strings and 12 solar cells in each string. One solar cell for a module of each type is completely shaded and the corresponding power-voltage curves are plotted in Figure 6.2. It is observed that, under these simplistic conditions, the power output of the PV module depends only on the number of bypass diodes. This is due to the fact that, if

one cell of a string is completely shaded, the whole string will be inactive and the output power is directly related to the number of shaded strings:

$$P = P_0 \times \frac{N_{\text{shade}}}{N_{\text{total}}} \tag{6.2}$$

Here, P_0 is the output power of the PV module when there is no shading effect. N_{shade} is the number of the shaded strings, and N_{total} is the total number of strings.

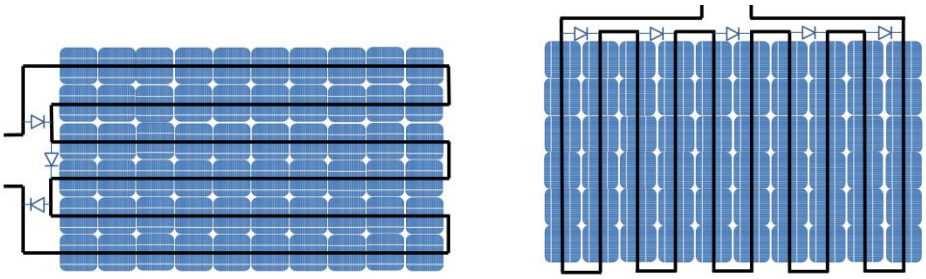

(a) (b)

Figure 6.1: The structure of (a) a c-Si PV module equipped with three bypass diodes and (b) a c-Si PV module equipped with five bypass diodes.

Since a module with five bypass diodes contains fewer solar cells per string, the output power is higher when there is only one cell shaded.

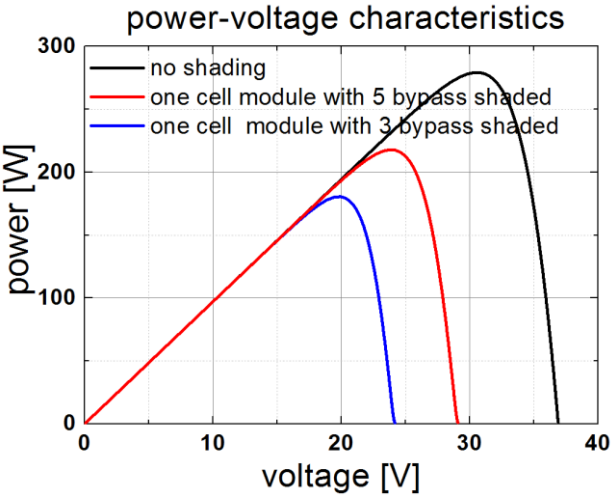

Figure 6.2: The power-voltage characteristics of c-Si PV modules with three or five bypass diodes under the condition that one cell in the module is completely shaded.

6.1.2.2 Influence of different grades of shading

In this section, the I-V characteristics of the PV module for different grades of shading is investigated. In this investigation only one cell of a module is shaded and

the transmittance of the shadow varies. The corresponding output power for a module with 60 cells and 3 bypass diodes is plotted in Figure 6.3.

As can be seen in Figure 6.3, two regions exist in the power-voltage curves. In the lower voltage region, the module power output is not affected by the grade of shading. In the higher voltage region, the grade of shading has an influence on the power characteristics. In the present example it is found that under this condition, for a shadow transmittance larger than 67%, the maximum power point (MPP) is in the higher voltage region, the power peak is proportional to the shadow transmittance where the bypass diodes are "off". For a shadow transmittance of less than 67%, the MPP is in the lower voltage region where the bypass diodes are "on". This effect can also be roughly generalized to a c-Si PV module with N_{total} strings and N_{shade} shaded strings. If the two peaks on the power-voltage curve are of the same value, we have:

$$P_0 \times T^* = P_0 \times \frac{N_{\text{total}} - N_{\text{shade}}}{N_{\text{total}}} \tag{6.3}$$

where P_0 is the MPP of a PV module without shading.

The calculated T^* from this equation is the shadow transmittance that leads to an equal value of the two peaks. The calculation based on Equation 6.3 is simple: for each shaded string, $1/N_{\text{total}}$ of the current is lost when the bypass diode is on. However, the position of the MPP is less obvious (as indicated in Figure 6.3) and needs to be calculated by the circuit model.

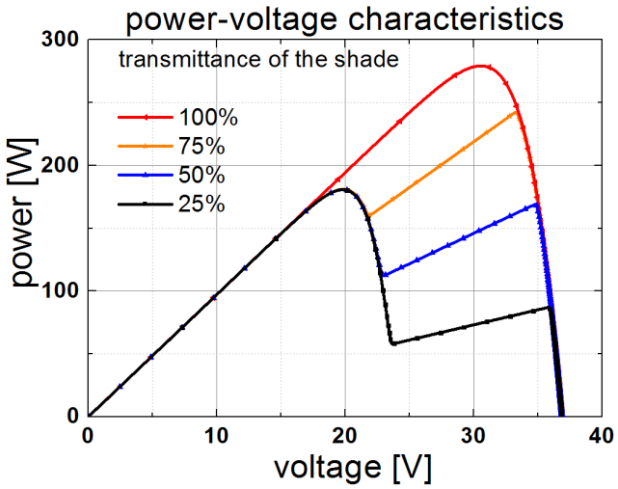

Figure 6.3: The power-voltage characteristics of the PV module with three bypass diodes and one cell shaded under different shadow transmittance.

6.1.2.3 Behaviour of a c-Si PV module under a moving shadow

In this section, a moving shadow is taken into consideration. Two different moving directions are considered, as shown in Figure 6.4 (a) and (b). The influence of the direction in which the shadow moves on the PV modules with different bypass diode configurations is evaluated. A time-dependent model using time-dependent current sources was implemented to investigate this problem. In the situation shown in Figure 6.4(a), the total passing time of the shadow is set to be five. The shadow moves one solar cell's length in each half hour, assuming that there is no space between two adjacent cells. In the situation of Figure 6.4(b), the time is set to be 3 hours. Thus the shadow speed is equal in both cases. The time-dependent maximum output power of a PV module with three bypass diodes and a PV module with five bypass diodes under the situation of Figure 6.4(a) and Figure 6.4(b) is evaluated (shown in Figure 6.5(a) and Figure 6.5(b)). In all the cases, the shadow transmittance is set to be 20%.

(a) (b)

Figure 6.4: (a) The shadow moves horizontally; (b) the shadow moves vertically.

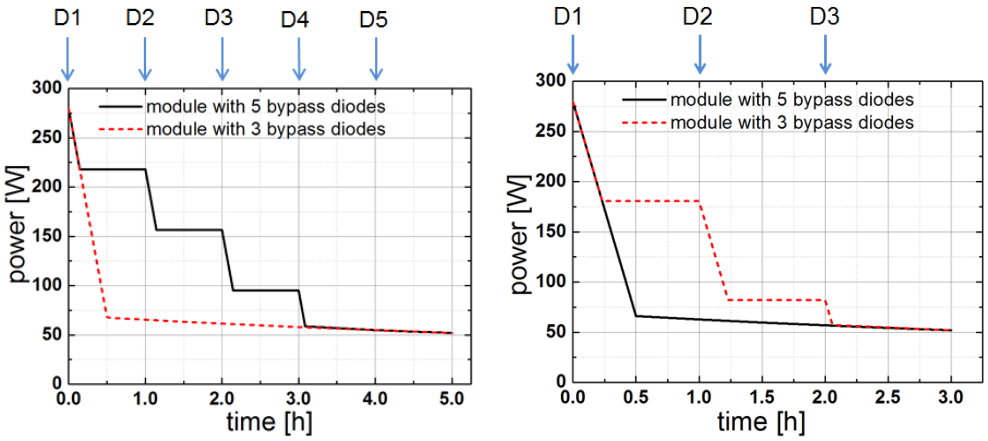

Figure 6.5: (a) The relationship between maximum power and time under the condition shown in Figure 6.4(a) for a shadow with 20% transmittance. (b) The relationship between maximum power and time under the condition shown in Figure 6.4(b) for a shadow with 20% transmittance. The figures also include the time point (shown as blue arrows) when the shadow reaches the string under each bypass diode (D1, D2, D3…).

Results show that the modules with different bypass diode configurations show different behaviour under the same moving shadow. For the situation shown in Figure 6.4(a), this three strings of the PV module with three bypass diodes are all shaded from the beginning. However, for the module with a five bypass diode configuration, the strings are shaded subsequently after 0, 1, 2, 3 and 4 h, respectively. With the incorporation of bypass diodes, a second peak of output power is created in the lower voltage region because of the remaining unshaded strings. It is calculated from Figure 6.5(a) that the energy output of the module with 5 bypass diodes is 50% larger than the energy output of the module with 3 bypass diodes. However due to the same reason, for the situation shown in Figure 6.4(b), the energy output of the module with

3 bypass diodes is calculated to be 27% larger than the energy output of the module with 5 bypass diodes (shown in Figure 5(b)). This simple example shows that for partial shading conditions the choice of the bypass configuration with respect to the moving direction of the shadow can be more important than the number of bypass diodes. The time range is not specific to the simulated time range, but can be generalized with any shadow passing time.

6.1.3 Case study: C-Si PV module configuration optimization for real condition

In Section 6.1.2, it was concluded that the bypass diode configuration has a strong influence on the PV module power output under partial shading condition. As a consequence, there is a need to evaluate the influence under actual operating condition. In this section, based on the simulations of Section 6.1.2, a specific case for a PV system suffering from inter-row shading is studied, and the influence of the bypass diode configuration on the c-Si PV module energy yield is evaluated.

Inter-row shading is a commonly happened effect for PV systems [133]. In principle, the inter-row shading of c-Si PV modules can be avoided by placing each row of PV modules to be very far from the next row. However in reality, the available land area is limited and the cable connection should be kept within a certain distance. Thus the distance between the PV arrays is usually limited, which leads to the inter-row shading of the PV system. This is especially the case for high-latitude places, where optimum operation requires a high tilt angle of the PV modules. Thus, methods introduced in Section 6.1.2 are used below to optimize the bypass diode configuration and reduce the shading loss.

For a typical PV system, the solar panels are usually tilted at an angle that is equal to the latitude and facing the equator in order to maximize the irradiance they receive each year. The row-to-row distance for the c-Si PV modules is usually around 2.5

times the module install height, but can vary greatly depending on the exact local conditions [140]. For many PV systems, the solar panels are configured in a way similar to that shown in Figure 6.6. Throughout the year the inter-row shading usually follows similar paths on the PV modules in early morning and late afternoon. From Section 6.1.2.3, the bypass diode configuration has a strong influence on the c-Si PV module power output when the shadow moves according to a certain path. Thus the bypass diode configuration can be optimized for a PV system suffering from inter-row shading.

Figure 6.6: Photograph of a typical PV system.

In order to investigate the problem, a simulated PV system in West Virginia, USA, is taken as an example. The setup of the system is shown in Figure 6.7. For this specific system, PV modules are tilted at an angle that is equal to the latitude (39^0) and facing the equator (south). The calculation is based on the method introduced in Sections 3.3.4 and 6.1.1. The efficiency of the PV modules is assumed to be independent of the illumination intensity. Two bypass diode configurations are investigated. Any shaded part of the PV module is assumed to receive no direct light. Measured irradiance data are used as input to calculate the irradiance received by the individual PV modules [141]. The data set includes the measured direct normal irradiance and diffuse irradiance data in West Virginia for a whole year (2001). Figure 6.8 shows the measured direct and diffuse irradiance for a certain period in the data set (from

2001.04.01 to 2001.04.20). During a very clear day, the direct light intensity is high and shows a perfect cosine profile. During a cloudy day or rainy day, the direct light is low and the diffuse light intensity is higher. It can be observed from Figure 6.8 that five days during that moth are very clear days.

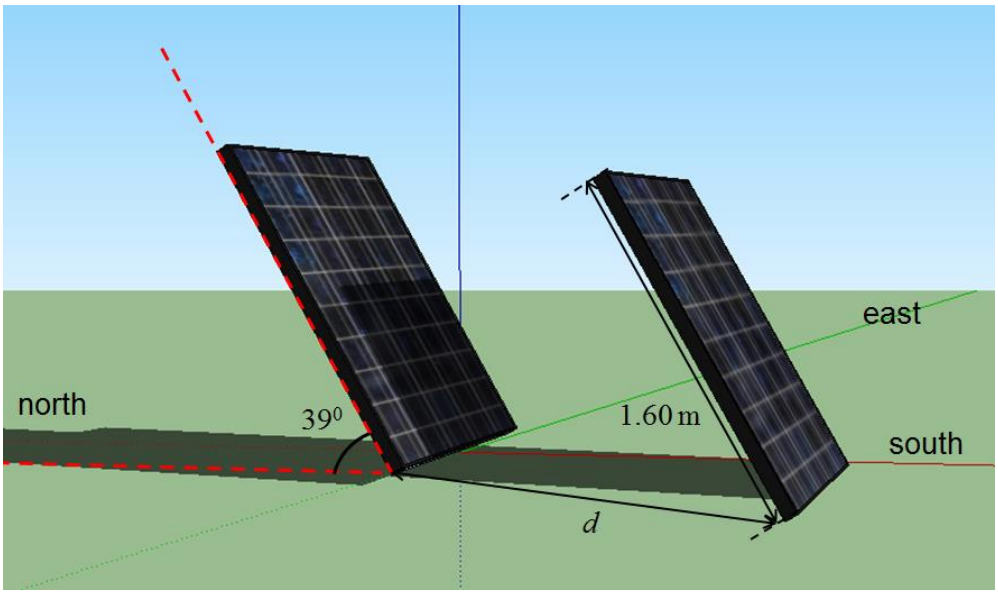

Figure 6.7: The setup of the c-Si PV modules in the investigated PV system. The figure shows two individual PV modules in two adjacent rows of the PV system. PV modules are tilted at an angle that is equal to the latitude (39^0) and facing the equator (south). The distance between two rows is represented as *d* in the graph. The length of the PV modules is 1.6 m in the simulation.

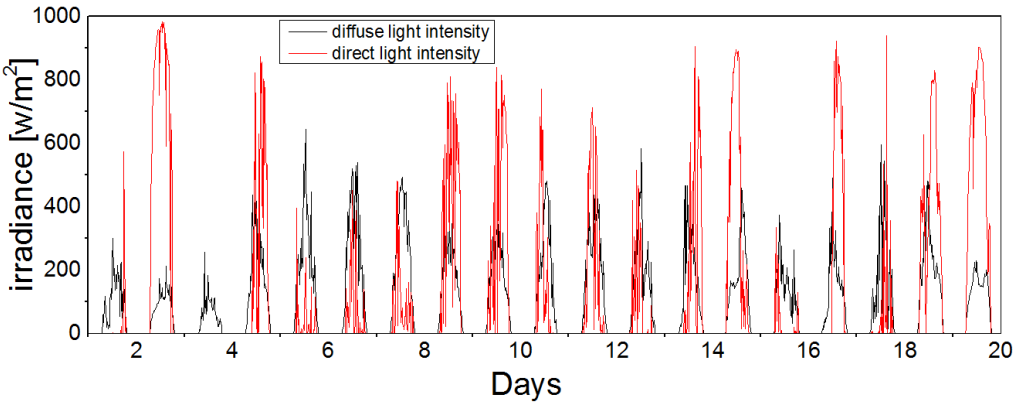

Figure 6.8: The measured diffuse light intensity and direct light from April 1st to April 20th, 2001 in West Virginia from CONFRRM data set [141].

Since the inter-row shading mainly affects the direct light received by the PV modules, here only direct irradiance is considered in the calculation. If a PV module is not affected by shading, the output power from direct light is assumed to be P_0. Consider shading effect, the PV module output changes to P_s. Here a performance factor R_p is defined in order to show the influence of the inter-row shading on the output power of a PV module:

$$R_p = \frac{P_s}{P_0} \tag{6.4}$$

Using this definition, the performance factor of a PV module is only affected by shading loss. For the module setup shown in Figure 6.7, the performance factor is compared between c-Si PV modules with two bypass diode configurations shown in Figure 6.1. The relationship between performance factor and the distance between two modules is calculated and shown in Figure 6.9(a).

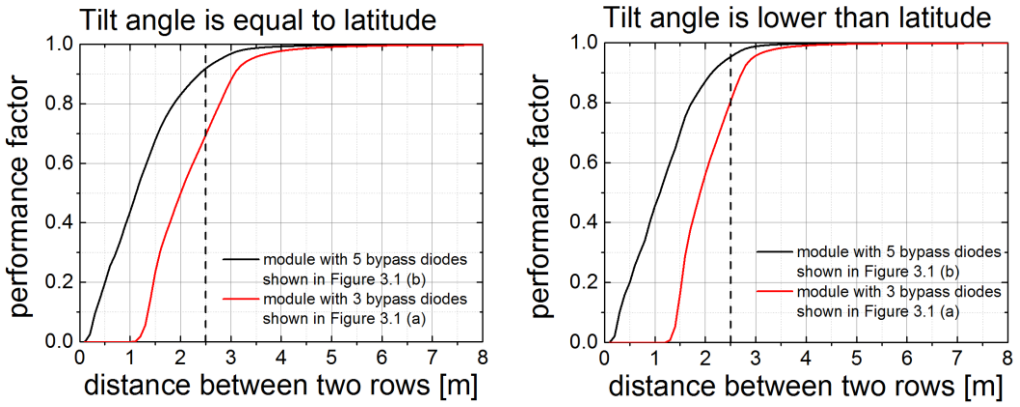

Figure 6.9: The relationship between the performance factor of the PV modules and the distance between two rows when the tilt angle of the modules is (a) equal to latitude (39^0) and (b) lower than latitude (29^0). Except for the tilt angles, the setups for PV modules in case (a) and (b) are all the same as what is shown in Figure 6.7.

It can be observed that when the distance between the two rows is very large (larger than 4 m), the bypass diode configuration nearly makes no difference on the PV module performance factor. This is because the inter-row shading effect is very small under this condition. However, the bypass diode configuration greatly affects the

performance factor when the distance between the two rows is very small (within 2 m). This is because that the shading effect happens frequently under high PV module install density. Since the inter-row shading always follows a similar path throughout a year, with the PV module setup in Figure 6.7, the shadow moving direction is very similar to what is shown in Figure 6.4(a). Under this condition, PV modules with 5 bypass diodes are more shading tolerant and generate a higher power output. Since the distance between two adjacent rows in a PV system is usually set to be around 2.5 times of the install height, it is calculated that under this condition, PV modules with 5 bypass diodes have around 32% more power output from direct light through the whole year. It is calculated from the measured irradiance data that direct light covers around 64 % of the total light received by a PV module when there is no shading effect. Thus the PV module with 5 bypass diodes has around 20% more power output per year than the PV module with 3 bypass diodes.

Furthermore, the results are compared with another case in which the modules are tilted at 29°, which is 10° lower than the latitude. This case is considered because in certain circumstances, the modules are tilted at lower angles to reduce shading loss [142]. The relationship between performance factor and the distance between two modules for this case is shown in Figure 6.9(b). When the install density is 2.5 times of the install height, PV module with 5 bypass diodes has around 19% more power output from direct light, which results in around 12% more annual power output from the total light. It can be observed that when the tilt angle gets lower, the bypass diode still has significant influence on the PV module power output. However, the influence gets smaller.

From this case study, it can be concluded that the bypass diode configuration has a strong influence on the c-Si PV module energy yield when daily inter-row shading. As a consequence, the bypass diode configuration should be seriously considered

during the installation of a PV system, especially for the high latitude places where the PV modules tilt at higher angles.

6.1.4 Conclusions for Section 6.1

In this section, a model of a c-Si PV module was constructed in LTSpice to investigate shading effects. First, the I-V characteristics of a c-Si PV module under different grades of shading were investigated. Two different bypass diode configurations were evaluated. Furthermore, a time-dependent model was developed to model the power output of a c-Si PV module for a shadow moving across the module. Some simple examples were investigated for shadows moving linearly over the module in different directions (6.1.2). These examples were used to show some basic features of moving shadows. It was found, especially, that the configurations of the bypass diodes have a strong influence on the power output of a c-Si PV module under partial shading conditions. PV modules with more bypass diodes were shown to perform better if only one string of a module is shaded. However, it was found that for shadows that move in a certain direction, the bypass configuration has a greater influence than the number of bypass diodes used.

Based on these simple examples, in Section 6.1.3 the model was extended to investigate the inter-row shading of a virtual PV system in West Virginia using measured irradiance data. It was found that the bypass diode configuration greatly affects the energy yield of the PV modules because of the daily inter-row shading. It was calculated that under normal install density, PV module with 5 bypass diodes has around 32% higher power output from direct light through the whole year. This effect should be seriously taken into account when installing c-Si PV modules in conditions for which known shadows occur, especially for the high-latitude places where the PV modules are required to tilt at higher angles.

6.2 Mismatch analysis for spectral response measurement of c-Si PV modules[4]

The mismatch effect is not only caused by partial shading. It is very common that the solar cells within a c-Si PV module have slightly different properties, e.g. one or several solar cells have a lower current than the others. Under normal operation condition, the c-Si PV module operating current is easy to be predicted, since the operating current is always limited by the cell with the lowest current. However, the author found via simulations that, under certain measurement conditions such as Spectral Response (SR) measurement condition, the operating current of a c-Si PV module is not simply limited by the cell with the lowest current. This section mainly focuses on the influence of cell mismatch on the SR measurement for c-Si wafer based PV modules.

SR measurements were already introduced in Section 3.2.2. On the solar cell level, SR measurements are well understood and there are numerous research works focusing on the SR measurement of solar cells [86, 143-148]. However, on the PV module level, the understanding of this measurement is still under development and needs to be further improved [147]. This is because a PV module is usually composed of a series connection of solar cells which have slightly different SRs. Also, in some cases, the cells are protected by the bypass diodes [139], which make the situation more complex.

Up to now, there is no steady-state monochromatic light source for full-area c-Si PV module illumination with high light intensity. The existing IEC standard 60904-8 [149] describes different SR measurement setups, but the impact of series inter-connection on the module SR is not discussed. Additional standards for an adequate

[4] This Section is based on the publication: J.Y. Ye, S. Guo, T.M. Walsh, Y. Hishikawa, R.A. Stangl, *"On the spectral response of PV modules"*, Measurement Science and Technology 25 (9), 095007. Among all the works presented in this paper, the circuit simulation work and the simulation result analysis were done by the author of this PhD thesis. The experimental works were done by other co-authors. This thesis only includes the simulation part of this paper.

measurement procedure to determine the SR of a c-Si PV module are still under evaluation [14-17]. Based on all these reasons, an investigation of the influence of the series connection of solar cells on the SR measurement of a c-Si PV module is required and an evaluation of different SR measurement methods is needed.

Under standard operating conditions, the operating current of a c-Si PV module is limited by the solar cell with the lowest short-circuit current, if bypass diodes are not considered. In the SR measurement of a c-Si PV module, the monochromatic light intensity is very low and varies with wavelength [150]. In this study it is found that, in most of the cases, the operating current of the c-Si PV module under low illumination conditions is not limited by the solar cell with the lowest short-circuit current. In this work, circuit modelling is used to study the influence of the variation of solar cell short-circuit currents on the SR of a c-Si PV module. The influence of the solar cells' shunt resistances and the bypass diodes are all studied. Based on the simulation result, two experimental methods used in the real measurement are compared.

6.2.1 Theory and method

For a standard c-Si PV module, if all the cells within the module have exactly the same short-circuit current, the SR of the PV module is the same as the SR of the individual solar cells under the same measurement condition. However, the short-circuit currents of the solar cells within a c-Si PV module usually vary from cell to cell, which has to be taken into account for the SR measurement. In this work, PC1D, a standard computer program for c-Si solar cell simulation [151], is combined with circuit modelling to investigate the influence of the variation of solar cell properties on the SR of a c-Si PV module. In the first step, PC1D is used to generate the SRs of 60 individual solar cells with randomly varied anti-reflection coating properties, including thickness (70-75 µm), texture angle (56-58 ^{0}) and refractive index (2.0-2.2).

Thus the SRs of the 60 cells have a distribution of short-circuit currents within a certain range. In the next step, the short-circuit currents of all solar cells are calculated under different wavelengths of the standard AM1.5G spectrum (with 50 nm band width and 10nm step). The calculated short-circuit currents are used as the input photocurrent for each solar cell in the circuit model. The 50-nm bandwidth corresponds to what is used in the measurement setup. The short-circuit current of the PV module for each wavelength can then be obtained. The relationship between wavelength and the short-circuit current of the 60 individual solar cells are shown in Figure 6.10.

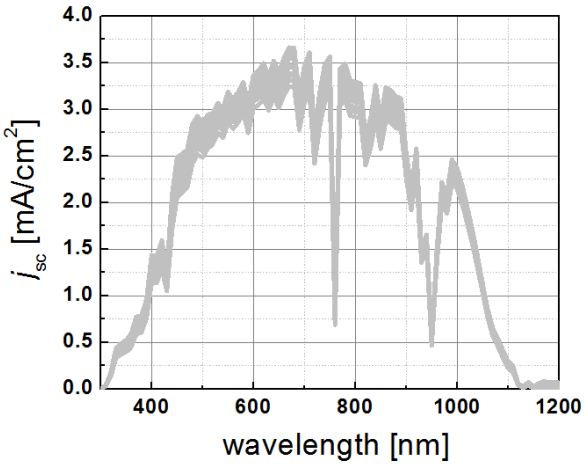

Figure 6.10: The simulated short-circuit current densities of 60 individual c-Si solar cells as a function of wavelength, assuming a bandwidth of 50 nm.

In the next step, the short-circuit current of the PV module can be calculated under each wavelength based on the circuit modelling method introduced in Section 3.3.2. The SR of the PV module can be calculated from the simulated short-circuit current $I_{sc}^{Test}(\lambda)$:

$$SR(\lambda)^{Test} = I_{sc}^{Test}(\lambda)/A_{\text{cell}}/\, G_{mono}^{ideal}(\lambda) \tag{6.5}$$

Here, $G_{mono}^{ideal}(\lambda)$ is the solar radiation at a single wavelength λ of the AM1.5G solar spectrum.

Since the simulated PV module is composed of solar cells connected in series, the series resistance of each solar cell adds to the total series resistance of the PV module. Thus the variation of series resistance of individual cells has no influence on the PV module SR. However, the shunt resistance of the individual cells can have an influence on the SR of the PV module, as will be shown in the following by simulation.

6.2.2 Simulation results and analysis

6.2.2.1 Ideal case: infinite shunt resistance

Figure 6.11 (black line) shows an ideal case for a c-Si wafer based PV module, where all the cells have infinite shunt resistance. It can be observed that, if there are no bypass diodes, the SR of the PV module is equal to the lowest SR of the individual cells. This is because the spectral response of the PV module is measured under zero bias. Since no bypass diodes are used in the simulated PV module, every cell must operate under the same current. Under zero bias, the cells operate under different voltages. Some of the cells are forward biased, while some of the cells are reverse biased. In this case, the cell with the lowest short-circuit current limits the current of the whole string and thus operates under reverse bias. Since the shunt resistance of the cells is infinite, the current-voltage curve of the cell under reverse bias is “flat” and does not change with the bias value until it reaches the breakdown voltage. As a consequence, at each single wavelength, the whole PV module operates at the lowest short-circuit current of all the solar cells, and the module SR is limited by the cell with the lowest SR.

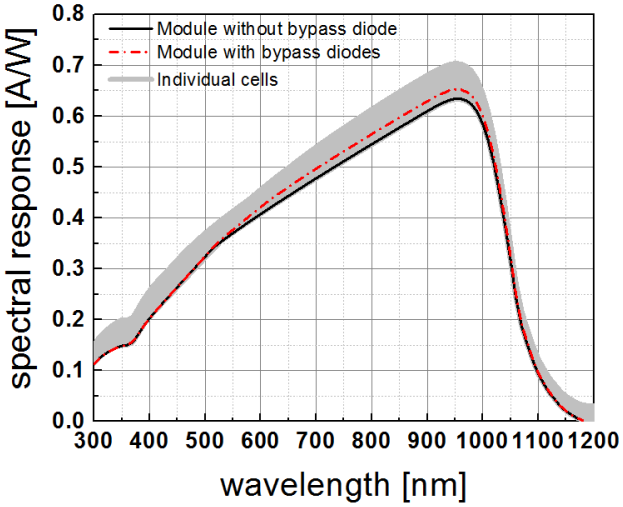

Figure 6.11: The simulated SR of a c-Si PV module composed of 60 solar cells connected in series. The shunt resistance of each solar cell is set to be infinite. The SR distribution of the individual cells is shown as the grey band.

When there are three bypass diodes connected in parallel with the solar cells, the SR of the PV module changes when the wavelength is larger than 550 nm. This indicates that the bypass diode is activated and transports current. The influence of bypass diodes on the module SR will be discussed further in Section 6.2.2.3.

6.2.2.2 Influence of finite shunt resistance

Figure 6.12 shows the current-voltage curves of two solar cells under different illumination conditions. One cell has an excellent shunt resistance of 250 kΩcm^2, and the other cell has a shunt resistance of 1.7 kΩcm^2, which is a typical value observed on many industrial 1-sun c-Si solar cells. It can be observed that the shunt effect for the solar cell with 1.7 kΩcm^2 shunt resistance is much more pronounced under low irradiance conditions, which corresponds to the illumination condition for SR measurement [84]. For the cell with excellent shunt resistance, the shunt effect can only be observed under low irradiance condition when the reverse bias value is very high.

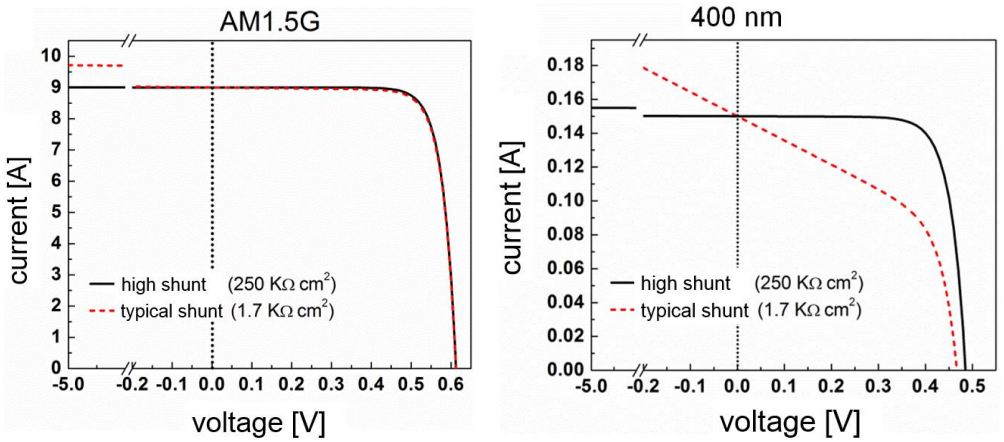

Figure 6.12: The simulated I-V curves of two solar cells under (a) one-sun condition and (b) 400 nm monochromatic light with an intensity of 50 W/m^2.

As a consequence, under standard operating condition (1.0 sun), the operating current of a c-Si PV module is always limited by the cell with the lowest current when the shunt resistance of the cells is within the normal range. However, under spectral response measurement conditions, even a typical shunt resistance value (1.7 kΩcm^2) has a large impact, and the operating current of the PV module is not necessarily limited by the cell with the lowest current but may be limited by the solar cell with the highest shunt resistance. In order to further study the influence of solar cell shunt resistance values on the c-Si PV module SR, four different cases are investigated:

(1) The shunt resistance of all solar cells is very high (250 kΩcm^2).

(2) The shunt resistance of all solar cells is relatively low (1.7 kΩcm^2).

(3) The shunt resistance of one cell is 250 kΩcm^2, and all the other cells have a shunt resistance of 1.7 kΩcm^2. The cell with 250 kΩcm^2 shunt resistance has the lowest SR.

(4) The shunt resistance of one cells is 250 kΩcm^2, and all the other cells have a shunt resistance of 1.7 kΩ cm^2. The cell with 250 kΩcm^2 shunt resistance has the highest SR.

The first two cases are used to study the influence of the shunt resistance on the c-Si PV module SR when the cells have relatively uniform shunt resistance values. The last two cases are used to study whether the cell with the highest shunt resistance determines the c-Si PV module SR. The simulation results for these four cases are shown in Figure 6.13.

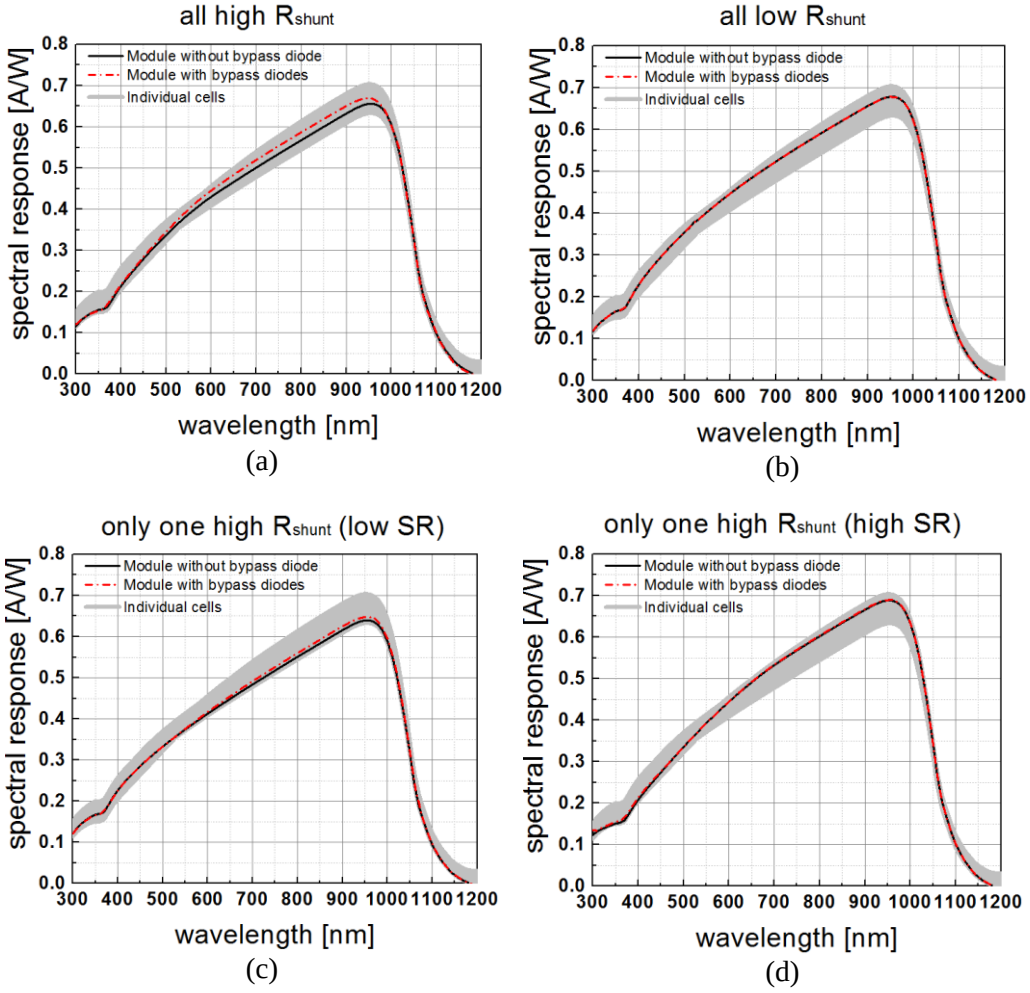

Figure 6.13: Simulated SR of a c-Si PV module composed of solar cells with finite shunt resistance. The simulation is performed under the AM1.5G spectrum with bandwidth of 50 nm (the intensity is in the range of 50 W/m^2). Four cases are studied: (1) the shunt resistance of all solar cells is very high (250 kΩcm^2); (2) the shunt resistance of all solar cells is relatively low (1.7 kΩcm^2); (3) the shunt resistance of one cell is 250 kΩcm^2, and all the other cells have a shunt resistance of 1.7 kΩcm^2. The cell with 250 kΩcm^2 shunt resistance has the lowest SR. (4) the shunt resistance of one cell is 250 kΩcm^2, and all the other cells have a shunt resistance of 1.7 kΩcm^2. The cell with 250 kΩcm^2 shunt resistance has the highest SR.

From Figure 6.13 it can be observed that for solar cells with finite shunt resistance, the SR of the PV module is no longer limited by the cell with the lowest SR. This is

because, as indicated in Figure 6.12, the I-V curve of this kind of cell is not flat but has a certain slope when the bias is close to zero. When the cells with different short-circuit currents are connected in series, some cells operate under forward bias and some cells operate under reverse bias. The slope of the I-V curve makes the whole string not operate at the short-circuit current of the cell with the lowest SR but at a current higher than the short-circuit current. As a consequence, if the cells within a c-Si PV module have finite shunt resistance, the SR of the PV module is not equal to the lowest SR of the cells but higher than this value. Comparing Figure 6.13(b) with Figure 6.13(a), it can be observed that the SR is higher for the PV module composed of solar cells with lower shunt resistance. This is because, as indicated in Figure 6.12(b), the solar cell with lower shunt resistance has a larger slope in the zero bias region, which allows the cell to transport a higher current under reverse bias.

From Figure 6.13(c) and Figure 6.13(d) it can be observed that, if the shunt resistance of one cell is much larger than the shunt resistance of other cells, the SR of this cell tends to dominate the SR of the PV module. If this cell has a lower SR than the other cells, it operates under reverse bias. If the cell has a higher SR than the other cells, it is forward biased. No matter whether it is reverse biased or forward biased, its operating current does not deviate much from its short-circuit current, since its I-V curve has a much smaller slope than that of the other cells. It can also be deduced that for the cases where a PV module has one or two shunted cells, the PV module SR will be determined by other cells with higher shunt resistance. However, this is only the case when the illumination intensity is not very low. Under very low intensity, due to the more pronounced shunt effect and the decreased open-circuit voltage, the SR is no longer determined by the cell with high shunt resistance. Furthermore, the measured SR for case (d) is higher for the PV module SR under outdoor conditions (within the wavelength range 550-1050 nm), since under outdoor conditions, the SR of the PV module is always limited by the PV module with the lowest short-circuit

current. This should result in an overestimation of the current for the PV module operating under 1 sun or equivalent condition.

In order to further investigate the influence of the shunt resistance, the I-V curves of two solar cells with different SRs are simulated. Under the 400 nm monochromatic light SR measurement condition (50 W/m^2), the SR of one cell is 10% higher than the other one. Figure 6.14 shows the operating current of the string under zero bias when the two solar cells are connected in series. In the simulation, several cases for different shunt resistance values are studied:

(1) Both solar cells have a high shunt resistance (250 $k\Omega cm^2$);

(2) Both solar cells have a low shunt resistance (1.7 $k\Omega cm^2$);

(3) The cell with the lower SR has a higher shunt resistance;

(4) The cell with the higher SR has a higher shunt resistance.

From Figure 6.14(a) it can be observed that if two solar cells with high shunt resistance are connected in series, the operating current of the string is equal to the short-circuit current of the cell with the lower SR. From Figure 6.14(b), if two solar cells with low shunt resistance are connected in series, the operating current of the string is between the short-circuit currents of the two solar cells, due to the different operating points of the two cells. Also, the bias on the cells in case (b) is much smaller than in case (a). From Figures 6.14(c) and (d), if the two solar cells have different shunt resistance values and this difference is large enough, the operating current of the series connected string is equal to the short-circuit current of the cell with higher shunt resistance. This also agrees with the results shown in Figures 6.13(c) and (d).

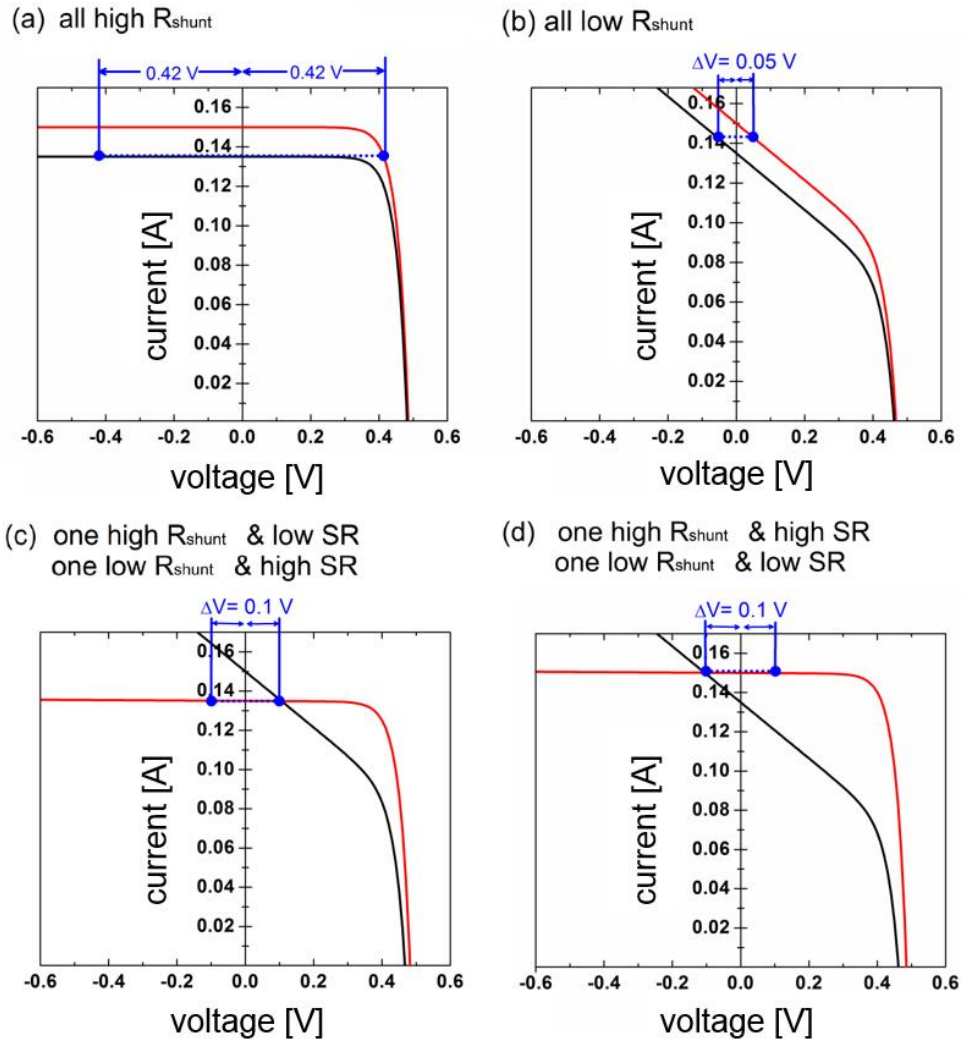

Figure 6.14: Simulated I-V curves for two solar cells with different SR under 400 nm monochromatic light (50 W/m^2) condition. Four different cases are studied: (1) Both of the two cells have high shunt resistance of 250 kΩcm^2; (2) Both of the cells have low shunt resistance of 1.7 kΩcm^2; (3) The cell with lower SR has shunt resistance of 250 kΩcm^2, and the cell with higher SR has shunt resistance of 1.7 kΩcm^2; (4) The cell with lower SR has shunt resistance of 1.7 kΩcm^2, and the cell with higher SR has shunt resistance of 250 kΩcm^2.

The cases discussed in Figure 6.14 are only for two cells connected in series. However, the results can be generalized to one string with any number of solar cells. Usually, a c-Si PV module contains three strings and each of them has 20 cells. First a case should be considered in which the cells in one string have slightly different SR but similar shunt resistance, which corresponds to case (a) and (b). For case (a), since all the cells have high shunt resistance, the operating current of all the cells is always equal to the current of the cells with lower current, no matter what the proportion of

the cells with lower current is. For case (b), if half of the cells have a higher SR and half of the cells have a lower SR, the bias and operating current of each solar cell would be the same as the case when there are only two cells. If the proportion of cells with lower SR is less than 50%, the operating current moves from the average of the two short-circuit currents to the short-circuit current of the cells with a higher SR. If the proportion of cells with lower SR is higher than 50%, the operating current moves from the middle of the two short-circuit currents to the short-circuit current of the cells with lower SR.

Also the case should be considered in which the cells have slightly different SRs and also different shunt resistance values, which corresponds to cases (c) and (d). Case (c) is similar to case (a), the operating current is always the current of the cells with the lowest SR because of the high shunt resistance of these cells. The only difference is the bias values for each cell is lower than case (a). For case (d), if the proportion of cells with lower current is lower than 50%, the operating current is always very close to the short-circuit current of the cells with higher SR. If the proportion of the cells with lower SR increases, the operating current point tends to move to the short-circuit current of the cells with lower SR.

It should be noted that the influence of bypass diodes is not considered in the discussions above. From the simulation results shown in Figure 6.11 and Figure 6.13(a), it can be observed that under certain conditions there is a difference between the SR of a PV module without bypass diodes and the SR of a PV module with bypass diodes. The operating principles of bypass diodes were introduced in Section 2.2.1. The main influence of bypass diodes on the spectral response measurement is that they make the operating current of the PV module not necessarily limited by the string with the lowest SR.

6.2.3 SR measurement method evaluation

As already shown in Section 6.2.2, the SR of a c-Si PV module depends very much on the measurement conditions. As discussed in Section 3.2.2, there are mainly two established methods to measure the spectral response of a c-Si PV module today, which are the partial illumination method and the full-area illumination method. In this section, these two methods are evaluated with respect to the described effect.

The partial illumination method calculates the PV module SR by averaging the SR of several target cells. However, the average SR of several individual cells may not exactly represent the real module SR. The full-area illumination method approaches the real module SR directly. However, the result can be influenced by the bandwidth of the filters and also the spatial inhomogeneity of the illumination. In order to compare the two different methods, the c-Si PV module SR is simulated based on the two different methods. In the simulation, all the cells have the same shunt resistance value of 1.7 $k\Omega cm^2$ and there is no bypass diode included in the module.

For the full-area illumination, the short-circuit current of individual cells are simulated using the actual measured quasi-monochromatic radiation value with certain bandwidth (50 nm). The properties of the individual cells have a certain variation so that the measured SRs have a certain distribution range. In the next step, the SR of the whole PV module is simulated by using the circuit model. This simulated “full-area illumination measured” SR is compared with the simulated SR under ideal AM1.5G monochromatic illumination. The results are shown in Figure 6.15.

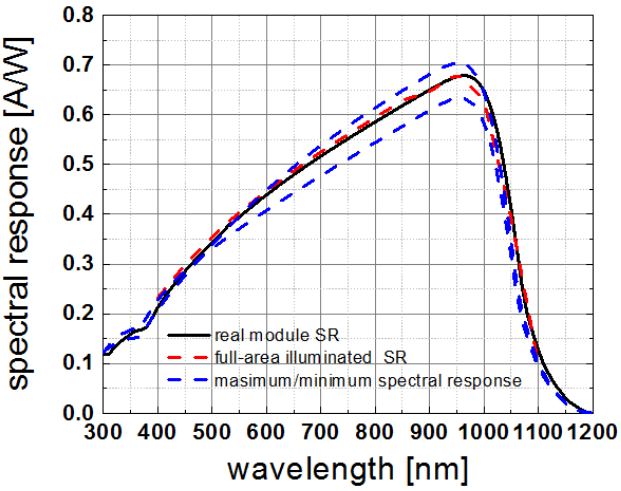

Figure 6.15: A comparison of the simulated "measured c-Si PV module SR" using two methods: partial-illumination method and full-area illumination method with filter bandwidth of 50 nm. The measured results using partial illumination method can be anywhere within the blue dashed line. The simulated ideal PV module SR under AM1.5G spectrum is also included for comparison.

For the partial illumination method, since it measures the average SR of several target cells, the measured PV module SR is located between the lowest and the highest SR of the individual cells and has a certain uncertainty. Thus the accuracy of this method depends on the variation of the SRs of the individual cells. If this variation range is very large, the partial-illumination method might result in a large uncertainty and deviate considerably from the real module SR. If the SRs of the cells within a PV module are quite uniform and have a small variation range, the partial-illumination method yields acceptable results. The result from full-area illumination method is very close to the PV module SR under AM1.5G spectrum. The difference is due to the bandwidth of the quasi-monochromatic radiation.

Based on the investigation in Section 6.2.2, when the cells within a PV module have lower or normal shunt resistance values, the PV module SR is close to the average value of the SRs of all the cells (Figure 6.13(b)). Since the partial illumination method generally measures the average SR of individual cells, in this case the result might also be close to the real PV module SR. However, under some special cases, if there is one current-limiting cell within a PV module and the shunt resistance of this

cell is large-enough, the SR of the PV module will be limited by this cell as shown in Figures 6.13(c) and (d). Since the partial illumination method takes the average SR values of several target cells, in this case the result may deviate from the actual module SR in operation, especially if the current-limiting cell is not included in the target cells. Also, the bypass diode effect cannot be taken into account by only taking the average value of several target cells. In general, the measurement result from full-area illumination method is more stable and close to the real module SR. For the partial-illumination method, it can have a larger uncertainty, but it can still approach the real module SR under certain cases.

6.2.4 Conclusions for Section 6.2

In Section 6.2, the influence of the mismatch effect on the spectral response of a c-Si PV module is investigated. It was generally believed that the operating current of a string of series connected solar cells is limited by the cell with the lowest current. However, it was found in this work that, due to the low illumination condition in SR measurements, the shunt effect of the solar cells is more pronounced, which makes the operating current of the PV module not limited by the cell with the lowest current. Even for the solar cells with moderate shunt resistance values (within the range of several thousand Ωcm^2), the pronounced shunt effect can obviously affect the SR measurement result for a c-Si PV module. From the investigation, it was found that the SR of a c-Si PV module is influenced by several factors, including: (1) the SRs of individual cells, (2) the shunt resistance of individual cells, and (3) the bypass diodes.

Also, two commonly used methods of measuring the c-Si PV module SR were simulated and compared. Based on the simulation results, it was found that the results obtained from one of the commonly used methods - the “partial illumination method” - can deviate strongly from the actual PV module SR under the AM1.5G measurement spectrum. In contrast, the full-area illumination method can better approach the real PV module SR and is therefore recommended.

7 A global comparison between vertically mounted bifacial PV modules and conventionally mounted monofacial PV modules[5]

In Chapter 6, the characteristics of a c-Si PV module were investigated under partial shading conditions and SR measurement conditions. In real PV applications, PV modules are integrated into a PV system to generate electricity. Thus, an estimation of the energy output for a PV module over a period of time is very important for the design of a PV system [152]. Also, the module configuration, install orientation, the climatic conditions, and the system ground cover ratio can all influence the power generation of the PV modules within a PV system. In this chapter, the irradiance received by a c-Si PV module is simulated based on the measured illumination conditions.

With the development of PV market, *bifacial* c-Si solar cells and PV modules become an attractive development direction of the PV industry. Yield calculations under different installation - or environmental conditions - are well established for conventional monofacial PV modules [153-155]. However, less attention was paid to the comparison of different module configurations. Especially for bifacial c-Si PV modules, most of the established work is based on experimental results. Theoretical models and simulation results are lacking for analysing this kind of PV module systematically. In this chapter, a detailed global comparison is made regarding one interesting aspect of bifacial c-Si PV modules, namely between the radiation received by vertically mounted bifacial modules (VMBM) and by conventionally mounted monofacial modules (CMMM). The motivation behind this study is to answer the question under which conditions do VMBMs generate as much or more power than CMMMs? For this purpose a MATLAB-based simulation was developed to

[5] Chapter 7 is based on the publication: S. Guo, M. Peters, T.M. Walsh, *"Vertically mounted bifacial photovoltaic modules: a global analysis"*, Energy **61**, 447-454, 2013.

investigate factors influencing the amount of energy received by a VMBM and a CMMM. It is found that the difference between the difference in radiation received by a VMBM and a CMMM mostly depend on i) latitude, ii) diffuse fraction and iii) albedo. Based on measured diffuse light fraction data, the minimum albedo required so that a VMBM receives more radiation than a CMMM is calculated for every position on earth's surface. Since the main goal of this work is to make comparisons between different technologies, the author assumes an ideal case in which the PV module power output is only affected by the received irradiance. The influence from other environmental factors (like humidity and temperature) are ignored in this study.

7.1 Introduction

Among different kinds of PV technologies, bifacial c-Si PV modules enjoy an increasing interest in recent years [156, 157]. There are several reasons for this:

- Glass-glass PV module construction technology has more benefits in terms of durability compared to the glass-backsheet module construction [158].
- Advanced solar cell manufacturing methods such as ion implantation and heterojunction technologies not only result in high-efficiency solar cells, but also naturally result in bifacial solar cells, unlike the aluminium back surface field (Al-BSF) c-Si solar cells which dominate the photovoltaic (PV) market today [159-162].
- VMBMs show a daily power generation that is significantly different from that of traditional solar systems and can solve some of the problems related to oversupply of solar energy around noon.

The structures of a monofacial and a bifacial p-type substrate c-Si solar cell are shown in Figure 7.1. The local contact on the back surface of bifacial solar cells allows them to absorb light from both the front side and the rear side. Their corresponding module structures are also included in Figure 7.1. Instead of having a sheet

on the back of the monofacial PV module, bifacial modules have glass on their back side which allows them to make use of the light coming from both sides.

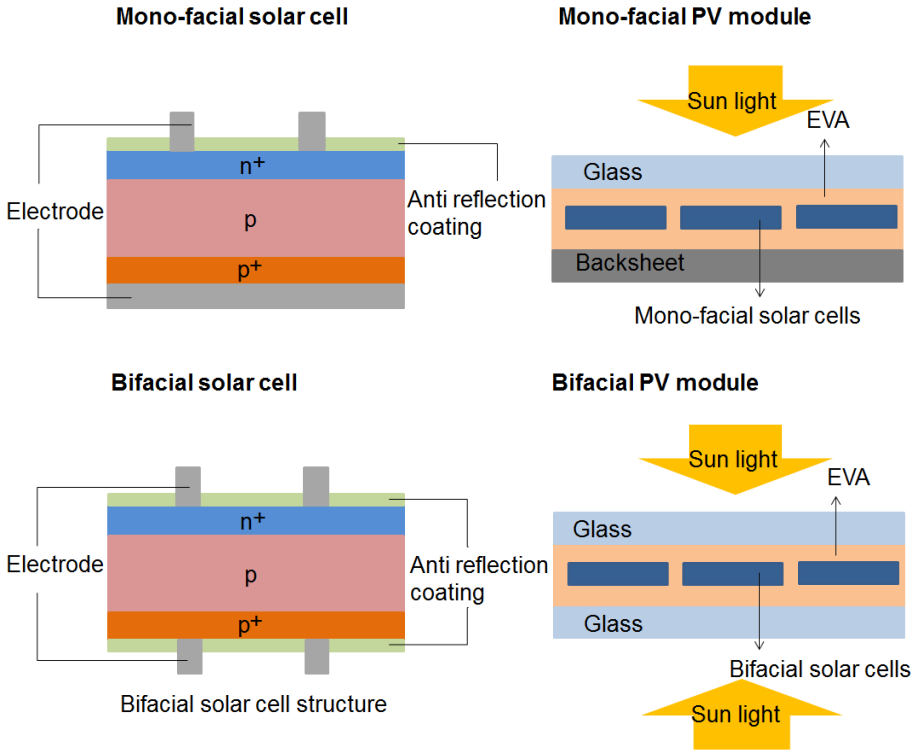

Figure 7.1: Structure of monofacial c-Si solar cells (upper left), monofacial c-Si PV modules (upper right), bifacial c-Si solar cells (lower left) and bifacial c-Si PV modules (lower right).

Depending on the installation, bifacial modules can produce up to 20% more energy per year in side-by-side comparisons than equivalent monofacial modules [163]. The cost of a bifacial PV module, however, is similar to the cost of a conventional mono-facial module with the same module size [164]. Bifacial modules can be installed vertically, facing East-West. This configuration not only saves space, but also has the probability to produce as much energy per Watt as CMMMs (tilted at latitude towards the equator) [165, 166]. The generation profile of such a VMBM is significantly different to that of a CMMM (see Figure 7.3). The VMBM produces more energy in the early morning and late afternoon than a CMMM. With increasing penetration of PV electricity generation in a grid (e.g. Germany), this “double peak” power output profile is more valuable, since most of today’s grid electricity comes from the

CMMM PV system and the VMBM offers a good compensation. VMBMs also have further advantages. They can, for example, be installed as sound barriers along roadsides and they are less prone to be covered by snow [132]. For these reasons it is necessary to investigate how the energy yield of VMBM is affected by the environmental factors and how it compares with CMMM.

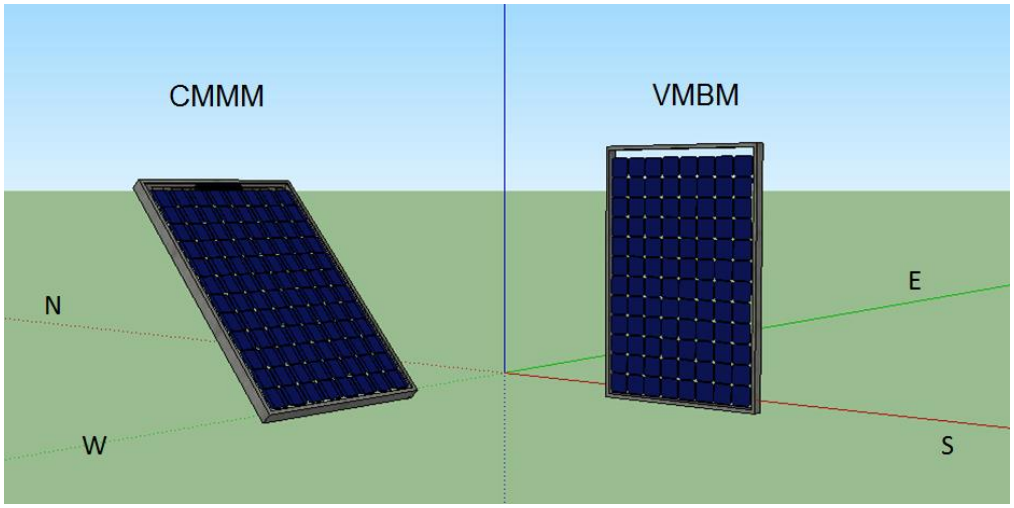

Figure 7.2: The setups of a VMBM and a CMMM. VMBM represents a vertically mounted bifacial module facing East-West, and CMMM represents a conventionally mounted monofacial module. The CMMM shown in the figure is in the northern hemisphere, and the tilting angle of the CMMM is equal to the latitude of its location, which is assumed to be close to the optimum tilt angle for this kind of PV system.

7.2 Simulation results and analysis

7.2.1 Daily radiation received by a VMBM and a CMMM

For bifacial modules, tilting at 90° and facing East-West (VMBM) is one of the most commonly used configurations, since it is easy to realize and also allows a relatively high power output for the modules. For monofacial modules, many investigations were done to find the angle that results in maximum energy output over a long period of time [152, 167-169], and it is found that a monofacial module will generate the maximum output when it is tilted at an angle which is almost equal to the latitude and faces the equator (CMMM) [170-172].

From the theory described in Section 2.3.2 and the method described in Section 3.3.4, the total radiation incident on a surface with arbitrary orientation during a certain period of time can be calculated. As an example, Figure 7.3 shows the simulated radiation received by a VMBM and a CMMM during a certain day in Singapore. It illustrates the two peaks in the profile for VMBM, which is due to the two situations in which the bifacial module receives most light. Curves like these are well known and have been shown for bifacial modules in different locations [156, 166].

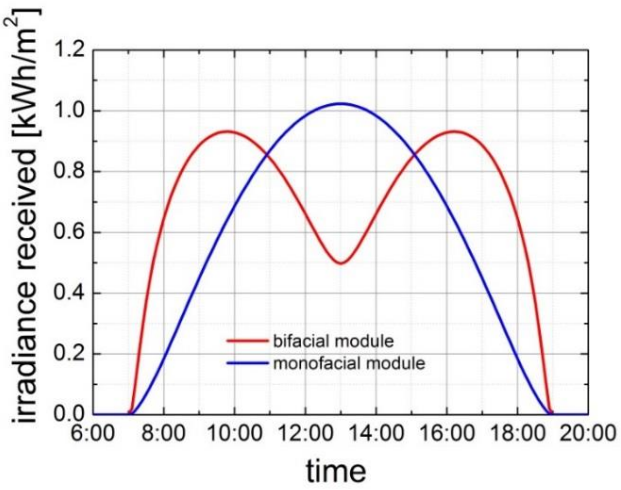

Figure 7.3: Simulated radiation received by a VMBM and a CMMM on a certain day in Singapore. The diffuse fraction is set to be 0.18, and albedo is set to be 0.35, which are practical values for clear-sky conditions in Singapore. From the two curves, it is calculated that the radiation received by the VMBM in the whole day is 8.54 kWh, which is larger than the radiation received by the CMMM (7.38 kWh).

7.2.2 Relation between diffuse fraction and radiation received

In order to compare VMBM with CMMM, radiation received by these two kinds of modules is calculated as a function of diffuse fraction. The calculation is carried out according to the theory and method described in Sections 2.3.2 and 3.3.4. From this first-step simulation it is found that the difference between the received irradiance of the two modules depends largely on latitude, diffuse fraction and albedo. The reason for this is that monofacial modules only accept diffuse light on one side. In contrast, bifacial modules accept diffuse light on both sides and have, therefore, an advantage in making use of the diffuse radiation.

In order to further compare VMBM with CMMM systematically, radiation received by these two kinds of modules is calculated as a function of diffuse fraction. In the calculation, an average annual transmittance coefficient is assumed. By changing this coefficient from 0 to 1, total H_{dir} and H_{diff} (direct and diffuse horizontal radiation) is integrated over the time of a year, and the average diffuse fraction can be calculated corresponding to certain average transmittance coefficient from Equation 2.26. After that, radiation received by a bifacial/monofacial module for a year can be calculated under different average diffuse fraction.

Figure 7.4(a) shows the radiation received by a CMMM facing the equator and a CMBM for a whole year in (a) Singapore (1^0 N) and (b) Berlin (52^0 N). Today's bifacial and monofacial modules have nearly the same single-side efficiency [173]. Also, the efficiency for a modern bifacial module is almost equal, no matter from which side it is illuminated [173]. In this work, it is assumed that both sides of the VMBM have the same conversion efficiency and that the conversion efficiency is equal to that of the CMMM. It is further assumed that the spectral composition of the light received by each side of a module is the same in all cases and doesn't depend on the diffuse fraction, albedo and light intensity. Using these assumptions, energy output of the two modules is calculated, using a module efficiency of 16% under AM1.5 condition in all cases. As the energy output of the two modules is proportional to the radiation that they received, the calculated output power follows the same trend as the received illumination. The yearly energy output of each kind of module is shown in Figure 7.4(b). Here the PV modules made with c-Si solar cells are just taken as an example. Since this analysis is quite general and not specific to any kind of solar cell, the energy output of any kind of bifacial solar cell can be obtained by multiplying the incoming power with the conversion efficiency.

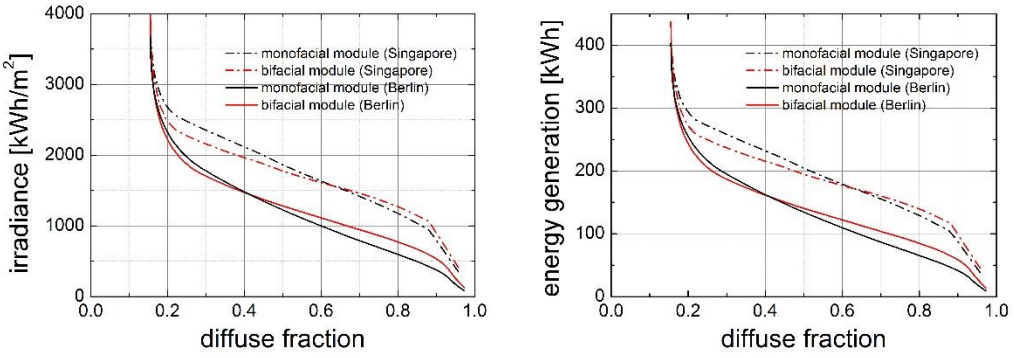

(a) (b)

Figure 7.4: (a) Radiation received and (b) energy generation by a CMMM and a VMBM calculated for a period of one year under different diffuse fractions in Singapore (1^o N) and Berlin (52^o N). The albedo is set to be 0.2 for both cases. The bifaciality of the bifacial module is assumed to be one.

From Figure 7.4, it can be observed that for a low diffuse fraction, the radiation received by the VMBM is less than the radiation received by the CMMM for both places (Berlin and Singapore). This is because the VMBM receives less direct radiation than the CMMM. As the diffuse fraction increases, the amount of radiation received by the VMBM increases and for a certain diffuse fraction exceeds the amount of radiation received by the CMMM. Thus there must be an intersection of the two curves, which marks the diffuse fraction required under which VMBM and CMMM receive the same amount of radiation and generate the same amount of energy in one year. From the simulation results, this required diffuse fraction is different for Singapore and Berlin. The reason is that the tilt angle for a CMMM in Singapore is close to zero degree, which is much smaller than the tilt angle for CMMM in Berlin (52^0). Thus it can be concluded that the diffuse fraction required for equal power output of a VMBM and a CMMM is specific to latitude. Since the back surface of the monofacial modules cannot receive diffuse light, a CMMM in Singapore receives almost 100% of the total diffuse light from the sky and nearly no diffuse light from the ground. However, a CMMM in Germany only receives about 71% diffuse light from the sky and 29 % diffuse light from the ground. Since under normal condition, diffuse light from the sky has a much higher intensity than diffuse

light from the ground, a CMMM in Singapore receives a much larger fraction of diffuse light than a CMMM in Berlin. Consequently, a higher diffuse fraction is needed to have a VMBM in Singapore receive an equal amount of radiation as a CMMM.

Using this approach, it is found that the crossing point of the two curves defined in Figure 7.4 can be expressed as a function of latitude only. If the relation between latitude and the crossing point can be calculated, it can provide an overview of how much diffuse fraction is needed for a certain place to make the output of a VMBM equal to a CMMM. If the real diffuse fraction of that place is equal or larger than this value, a VMBM generates a higher power output. On the other hand, if the actual diffuse fraction is lower than this value, a CMMM generates a higher power output.

The result of this calculation is shown in Figure 7.5. For numerical reasons, calculating the exact intersection point (as shown in Figure 7.4) can be difficult. The result shown in Figure 7.5 gives the condition for which a VMBM receives 1% more radiation than a CMMM. As already mentioned in Section 2.3.2, the simulation under various diffuse fraction is achieved by changing the transmittance coefficient. The relation between the diffuse fraction and transmittance coefficient, which is required in the calculation, is described based on existing meteorological models. In order to verify the results, three different meteorological models are used for comparison (also shown in Figure 7.5). All three models were introduced in Section 2.3.2. Among the models, Compbell and Norman's model is shown in Equation 2.17, which is more suitable for clear-sky condition. Rendl's model and Ogill's model are described in Table 2.2, which are suitable for both clear-sky and overcast condition. It is observed that the curves obtained from different models agree quite well. This is reasonable, since no matter which model is used, the difference of radiation received by the two kinds of modules only depends on the diffuse fraction. Their absolute values may change, but the crossing point of the two lines is only a function of diffuse fraction

and doesn't change much. Since the albedo also plays a role in the irradiance received by the two kinds of module, in Figure 7.5, a constant albedo value of 0.2 is assumed first and the influence of the albedo values will be investigated in the next step. The data are obtained from NASA surface meteorology and solar energy: global data sets [39].

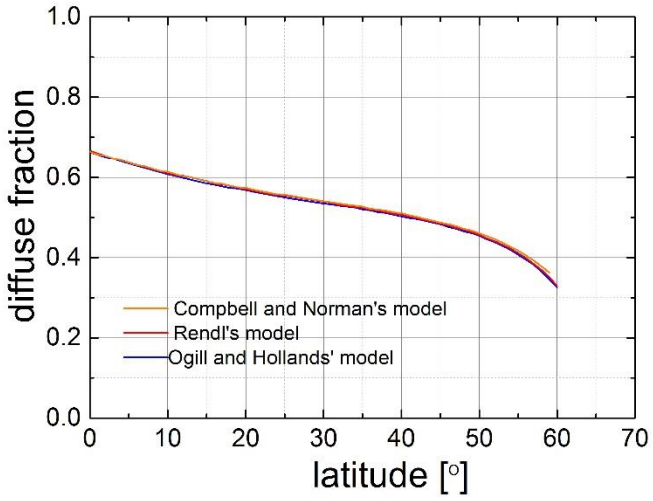

Figure 7.5: Calculated diffuse fraction for which a VMBM receives 1% more radiation than a CMMM. The calculations were performed using three different meteorological models. The albedo of the ground is set to 0.2. If the actual diffuse fraction of a certain place is above the line, it is preferable to use VMBM instead of CMMM. Also given are the actual diffuse fractions for some cities [39].

As mentioned, the albedo used for Figure 7.5 was 0.2. In reality, the albedo for different places is different. Since Albedo is the fraction of the radiation reflected from the ground into space, it has an influence on the curve shown in Figure 7.5. Therefore, the same calculation as shown in Figure 7.5 has been repeated for different albedo values. The results are shown in Figure 7.6. From Figure 7.6 it can be seen that, as the albedo increases, a smaller diffuse fraction is required to make the VMBM and CMMM receive the same amount of radiation, and more cities move above the line. The reason is that as albedo increase, there is more diffuse light coming from the ground, which is more favourable for VMBMs. When albedo increases to more than 0.35, the diffuse fraction that makes a VMBM receives 1%

more radiation than a CMMM does not exist for a large range of latitudes. This means that for these places, even if the diffuse fraction reaches the minimum value, a VMBM can still receive more irradiance than a CMMM, since the tilt angle for a CMMM, which is equal to the latitude, is small for low-latitude places. Thus the CMMM can receive only a very small fraction of diffuse radiation from the ground. Bifacial modules, however, receive all diffuse radiation from the ground. As the albedo value increases, diffuse radiation from the ground also increases, thus bifacial modules tend to receive more radiation for these places. When the albedo reaches a certain value, even a very low diffuse fraction can still results in higher collected irradiance for VMBM in these places.

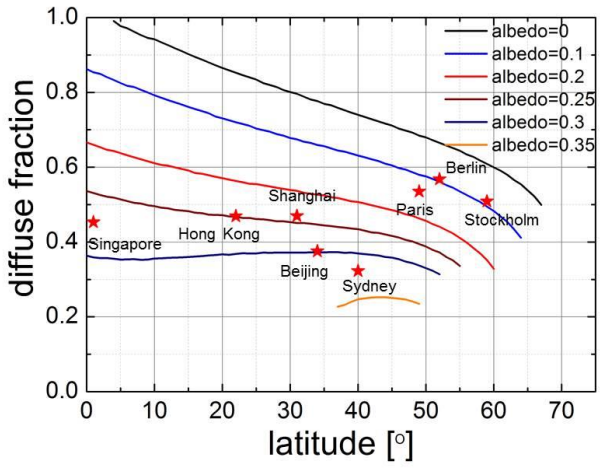

Figure 7.6: Diffuse fraction for which a VMBM receives 1% more radiation than a CMMM, calculated as a function of latitude and for different albedo values. The stars in the figure indicate data for actual cities.

7.2.3 A global comparison of VMBM and CMMM

Finally, the author would like to answer the following question: if the diffuse fraction of a certain place is already known, what is the minimum albedo value needed to make the VMBM have more power output than the CMMM at this place? In order to solve this problem, the albedo required for a VMBM to receive 1% more radiation than a CMMM is calculated based on the actual diffuse fraction data of every position

on the earth's surface. The global data of the diffuse fraction of light are obtained from NASA surface meteorology and solar energy: global data sets [39]. The results are shown in Figure 7.7. If the albedo of a place is larger than the value shown on this map, the VMBM of that place receives and converts more power than the CMMM. Subsequently, the average albedo data for one year is calculated from the data set ISLSCP II MODIS (Collection 4) Albedo, 2002 [40]. By comparing the calculated albedo values that results in a higher power output of VMBM with the actual average albedo value, a decision can be made whether VMBM or CMMM is more suitable for a certain place in the world. The results are shown in Figure 7.8.

From Figure 7.8, for a large part of the high latitude places in the northern hemisphere, including Russia, Canada, Greenland and North and Central Europe, VMBMs have higher power output and this configuration is preferable to CMMMs. The main reason is that only a small albedo value (less than 0.2) is required to result in a higher power output of VMBM in these places, and the real albedo value is relatively high. For places like North Africa and Middle East, the albedo required to make a VMBM have higher power output than a CMMM is relatively high; however, the actual albedo value is higher (sand cover). Thus for these places, it is also better to use VMBMs instead of CMMMs. In places like the United States, South America, Central and South Africa, India, East and South Asia and Australia, albedo values above 0.3 are required to make a VMBM have higher power output. Since the real albedo value for these places is lower than the required values, CMMMs have higher power output in these places. It should be noted that, since the data used in this work are obtained from satellite pictures, the results should generally be true for large-scale PV power plants in countryside. In urban areas, because of the surrounding buildings and some other factors, the diffuse fraction and albedo might be very different from the data obtained from the satellite pictures. The method introduced in this section is still valid for urban areas, but it must be analysed case-by-case based on the real

albedo and diffuse fraction data of the specific location where PV modules are installed.

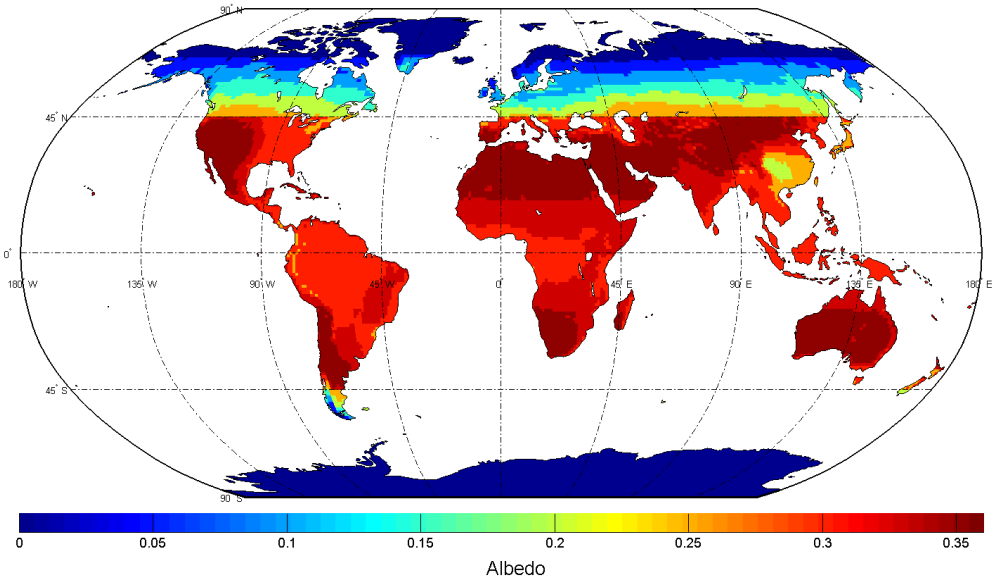

Figure 7.7: The minimum albedo value corresponding to each place in the world above which the energy yield generated of a VMBM is higher than the energy yield of a CMMM there.

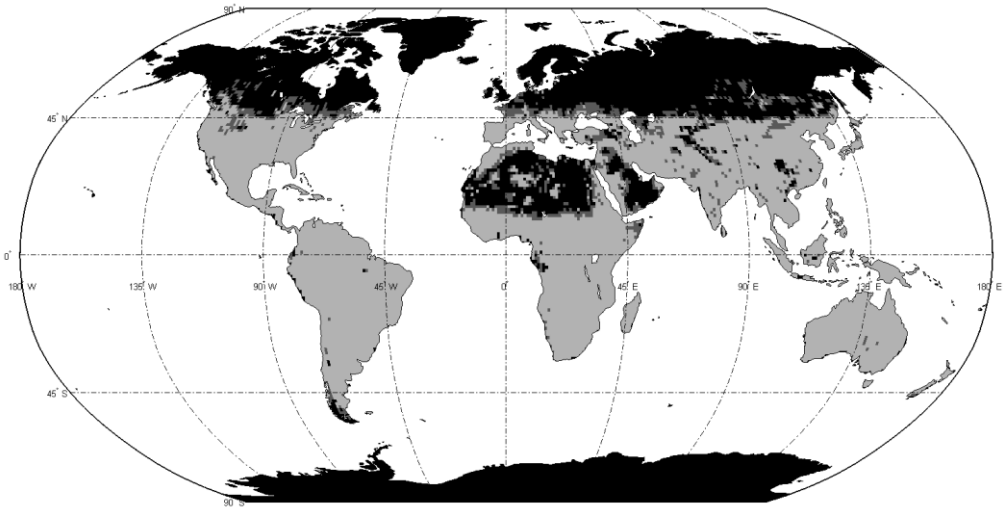

Figure 7.8: Global map that representing which kind of module configuration results in higher yield generation in a certain place. Black: VMBM. Light grey: CMMM. Dark grey: the two kinds of modules have very similar yield generation.

7.3 Conclusions for Chapter 7

Vertical mounting is a unique install configuration for bifacial c-Si PV modules which has many advantages. In order to evaluate the potential of this VMBM, in this chapter it was compared with a conventional PV system. It was found that the answer to the question "which of these module configurations generates more power" depends mainly on three factors: the latitude, the diffuse fraction and the albedo.

In the first step, the relation between diffuse fraction and radiation received by a module was investigated, and the diffuse fraction required to result in higher power output or the VMBM was calculated as a function of latitude. It was found that the calculated required diffuse fraction agrees well for all used models. After that, the minimum albedo value required to make a VMBM have more power output than a CMMM was calculated based on real-measured diffuse fraction data for every place in the world. Comparing the required albedo with the real albedo distribution, the question "which module configuration has more power output" could be answered for every place in the world. Different regions in the world were analysed based on these results.

From an economic point of view, the cost of the two kinds of module is almost the same, which is proved by scientific reports and literatures [142] [164]. Therefore it is assumed that the return of investment for these two kinds of module only depends on the total radiation they receive during their whole lifetime. As a result, Figure 7.8 is also a graph that shows which kind of module is better from an economic point of view.

In conclusion, the influence of latitude, diffuse fraction and albedo on two PV module configurations were investigated in this chapter. This investigation provides an over-view of which of these configurations generates more output in a certain location. Also, the method used in this work is not limited to this specific topic, but can also be

applied to solving various problems related to the energy yield evaluation of PV modules under real operating condition.

8 Summary and future work

8.1 Summary of the thesis

In this thesis, various c-Si PV module-related problems were investigated. The problems and hypotheses investigated in this thesis were introduced in Chapter 1. In the present section, the answers to these PV module related questions will be listed and the main contributions to the field will be summarized.

Chapter 2 provided background knowledge and introduced the most important theoretical concepts used in this work. This included a basic introduction to c-Si wafer solar cells and PV modules. Fundamentals of sunlight and how different irradiance compositions (direct/diffuse light) depend on the environmental conditions were also introduced, which were needed in the thesis to understand the analysis for irradiance received by PV modules in different locations and under different environmental conditions.

Chapter 3 introduced the theoretical and experimental methods used in this thesis. The theoretical methods included various models for investigating PV modules, including the network model for interconnected solar cells, the electrical circuit model for PV modules, the optical model quantifying the light trapping effect of the exposed backsheet region and the optical model for calculating the irradiance received by a tilted surface. The experimental methods were the PV module fabrication methods. The characterization methods were the SR measurement and the I-V measurement for PV modules.

Chapters 4-7 described the main results of this thesis. In Chapter 4, interconnection resistive losses or c-Si PV modules were analysed from two aspects:

(1) Interconnection resistive losses were compared for c-Si PV modules using monofacial and bifacial solar cells. Established analyses used a 1D approach and could not accurately describe the 2D transport of current in the metal rear side of a

monofacial solar cell. The 2D current flow pattern in the metal sheet was investigated using circuit simulation, which was found to have significant deviations to the 1D model. The calculated resistive power loss for the ribbons on the full-area metal sheet is only 67% of the result from 1D model. Also, the resistive loss on the metal sheet is around 50% of the rear ribbons for monofacial cells, which is often ignored. These deviations result in an error of 10% for the total interconnection resistive loss. To account for these deviations, correction factors were introduced for the analytical equations for c-Si PV modules using monofacial cells.

(2) Interconnection resistive losses were compared for c-Si PV modules using full-size cells and halved cells. From a theoretical derivation it was found that using cut cells in c-Si PV modules reduces the resistance loss of the ribbons by a factor 1/n (where n is the number of pieces into which the cell is cut). Simulations and experiments were carried out for c-Si PV modules using monofacial/bifacial full-size and halved cells. Experimentally, for monofacial cells, the halved-cell module was found to have a 1.7% fill factor increase and a 1.8% power increase. For bifacial cells, the halved-cell module had a 2.0% fill factor increase and a 2.2% power increase. All these results were accurately predicted by simulation, which validated the theory and the methods used in this work.

The c-Si PV module power output is also affected by its optical properties. One property concerns the light trapping via electrically inactive, scattering surfaces in a PV module. Examples for such areas are the metal fingers or the exposed backsheet region. Light incident in these areas is scattered, partially internally reflected at the glass-air interface, and then has a second chance to reach the active solar cell regions and be absorbed there. This effect was investigated in Chapter 5. In the presented analysis, the amount of light scattered by the exposed backsheet and reaching the solar cell was quantified theoretically by ray-tracing. Both specular and angular dependent scattering properties of the backsheet were taken into account, which had

not been done in previous studies. The developed ray-tracing method was used first to study the short-circuit current increase obtained by replacing full-size solar cells in a c-Si PV module with halved cells. Experimentally 3.1% relative increase in short-circuit current and a 4.8% relative increase on output power were achieved for an optimized module layout. This result was well predicted by simulation. After that, the analysis was extended to other inactive areas and a full area-related loss analysis of a c-Si PV module was presented. It was found that for a standard industrial size c-Si PV module, the light intensity reaching the active area is increased by around 5% due to the light trapping effect occurring on fingers, ribbons and backsheet. For the backsheet area, this provides guidelines for a potential optimization of c-Si PV modules using the light-trapping effect.

Both Chapter 4 and Chapter 5 analysed c-Si PV modules under standard test conditions. In actual applications, PV modules are installed in a PV system and operate under outdoor condition. Even under the measurement conditions, different kinds of measurements may require different conditions. Like SR measurement, it requires monochromatic illumination with very low intensity. These conditions can be very different from STC and introduce various problems. Chapter 6 and Chapter 7 were dedicated to investigate the behaviour of c-Si PV modules under various conditions.

In Chapter 6, two studies relating to the mismatch effect in c-Si PV modules were presented. In the first study, the mismatch effect caused by partial shading was investigated. Shading effects had been investigated before for stationary shadows. The study presented here considered the movement of shadows and investigated its influence on c-Si PV modules with different bypass diode configurations. Investigations were then extended to simulations of the irradiance received by c-Si PV modules within a PV system. Based on measured irradiance data, it was calculated

that different bypass diode configurations affects the energy yield of a PV system by 20% under inter-row shading condition.

In the second study, the mismatch effect of c-Si PV modules under SR measurement conditions was investigated. Influence of the shunt resistance and SRs of individual cells on the SR of a c-Si PV module were investigated by simulation. Different SR measurement methods were compared. It was found in this work that the SR of a c-Si PV module strongly depends on the light intensity of the operating condition and the shunt resistance of the individual cells. This work breaks the established concept that the operating current of a c-Si PV module is limited by the cell with the lowest current. It was found that this assumption can lead to an error as large as the spectral response variation range of the individual cells (around 10% in the simulated PV module).

In Chapter 7, a global comparison was made between conventionally mounted monofacial c-Si PV modules and vertically mounted bifacial c-Si PV modules. Established works mainly focused on yield calculations for CMMMs. However, given the fast development of the different PV module technologies like bifacial PV modules, it is necessary to take different PV module configurations into account and make comparisons. It was found in this study that the geographic location, diffuse fraction and albedo can all affect the difference on the energy yield for the two module configurations. The results give the guideline of choosing the appropriate PV module configurations based on the real-measured diffuse faction and albedo data for every place in the world. It was found in this study that in the following regions the VMBMs can generate significantly more power output than CMMMs: Russia, Canada, Greenland, North and Central Europe, North Africa, Middle East and the South Pole.

8.2 Main contributions of this thesis

1. The influence from two-dimensional current flow on the CTM resistive loss was investigated for the first time. Based on the correction factors proposed in this thesis, researchers are now able to perform a more accurate calculation of the CTM resistive loss for PV modules using monofacial cells.

2. An enhanced light-trapping effect for PV modules using halved cells was found. Both the specular and the angle dependent scattering properties of the backsheet were considered in the study, which leads to more accurate calculation results compared with earlier works. A 5% power output gain was achieved for halved-cell PV modules, which is a big improvement.

3. It was found that, under SR measurement conditions, the short-circuit current of the PV module is not necessarily limited by the cell with the lowest current and thus needs to be studied case-by-case. This effect had not been considered in earlier works.

4. A global comparison was made between conventionally mounted monofacial PV modules and vertically mounted bifacial PV modules. Rather than investigating the performance of bifacial PV modules in a specific place, the results give a guideline for how to choose the appropriate PV module configuration for any location on Earth.

8.3 Future work

In this thesis, different aspects and losses were investigated concerning c-Si wafer based PV modules. The main contribution of this thesis is that it offers a holistic analysis of c-Si PV modules. In the studies, individual cell properties and other PV module components (ribbons, backsheet, etc) were considered and analysed as a whole. The resistive loss analysis and light trapping analysis give researchers the direction for optimizing the design of c-Si PV modules. The PV module mismatch analysis and yield analysis allows people to choose the optimum PV module and

bypass diode configurations. All these studies help minimize the different kinds of PV module related losses and improve c-Si PV module power output under STC condition and also in the real-word condition. Thus, the initial goals of this thesis as introduced in Chapter 1 have been achieved. In addition, the different theoretical models built in these studies can all be applied and extended to solving more problems related to c-Si PV modules. Based on the methods and results shown in this thesis, possible future works are proposed below.

8.3.1 Full loss analysis for different kinds of c-Si PV modules

Chapter 4 and 5 presented a resistive loss analysis and a light trapping analysis for different kinds of c-Si PV modules separately. In the future, the presented methodology can be extended to a full loss analysis and comparison of halved cell/full cell c-Si PV modules using monofacial/bifacial solar cells, both under STC and outdoor conditions. By this way the design can be further optimized for different c-Si PV modules.

The optical loss analysis presented in Chapter 5 was limited to the light trapping effect of the inactive areas. To perform the full optical gain/loss analysis, the method can be combined with the methods described in [38, 41] to quantify the optical loss in each layer and interface. Bifacial solar cells can be either applied in monofacial PV modules and bifacial PV modules. For monofacial PV modules, light reflected by the backsheet area and reaching the rear surface of the solar cell can also be utilized by bifacial cells. For bifacial PV modules, there is no backsheet in the PV module and no light trapping happens in the backsheet area. Some of these problems were recently addressed by the author and her colleagues in a recent publication [174]. From the optical analysis, the loss of short-circuit current can be quantified. A resistive loss analysis can be carried out using the methods introduced in Chapter 4. Taking the calculated short-circuit current into account, the fill factor loss can be quantified. As a consequence, the power loss on each element can be calculated and a pie chart can be

obtained. This analysis can help researchers compare the losses for different kinds of c-Si wafer based PV modules, make decisions and apply potential optimization methods.

8.3.2 Real-time PV system simulation

In this thesis, long-term energy yield calculations were done for different kinds of c-Si PV modules in Section 6.1.3 and Chapter 7. This long-term energy yield is useful in evaluating a PV module. However, in some applications, the real-time power generation is required to ensure the system operates healthily – a stand-alone PV system is an example. This kind of system is usually composed of a PV unit, a battery, power electronics and a load. The size of each component must be designed properly in order to ensure the healthy operation of the system under extreme conditions like extended periods of rainy or cloudy weather. This cannot be achieved by only looking at the long-period energy yield of the PV modules, thus real-time transient simulation is required. The system simulation can be done as follows: (1) Since the circuit modelling of c-Si PV modules has already been performed in this thesis, the system model can also be constructed by adding the battery model and the load. Existing battery models can be found in [175-177]. (2) Using real-measured irradiance data as input, the real-time irradiance received by PV modules can be calculated according to the method described in Section 3.3.4. (3) By using the calculated irradiance in the system circuit model, the real-time simulation can be achieved. The battery state of charge can then be obtained to estimate whether the system can operate smoothly. The size of the PV units and batteries can then be optimized. In all, this real-time PV system simulation allows people to optimize the size of system components based on the real environmental condition, which can be very useful for PV system design.

9 Publications arising from this work

Journal publications

1. **S. Guo**, J. Schneider, F. Lu, H. Hanifi, M. Turek, M. Dyrba, I.M. Peters, "*Investigation on short circuit current increase for PV module using halved cells*," Solar Energy Materials and Solar Cells **133**, 240-247 (2015).
2. I.M. Peters, **S. Guo**, Z. Liu, "*Full loss analysis for a multicrystalline silicon wafer solar cell PV module at short circuit conditions*," Progress in Photovoltaics *(2015, in press).*
3. J.P. Singh, **S. Guo**, A.G. Aberle, I.M. Peters, T.M. Walsh *"Comparison of glass/glass and glass/backsheet PV modules using bifacial silicon solar cells,"* IEEE Journal of Photovoltaics **5**, 783-791 (2014).
4. J. Ye, **S. Guo**, T. M. Walsh, Y. Hishikawa and R.A. Stangl, "*On the spectral response of PV modules*," Measurement Science and Technology **25**, 095007 (2014).
5. **S. Guo**, J.P. Singh, T. M. Walsh, A.G. Aberle, I.M. Peters, "*A quantitative analysis for PV modules using halved cells*," International Journal of Photoenergy **2013**, 739374 (2013).
6. **S. Guo**, I.M. Peters, T.M. Walsh, "*Vertically mounted bifacial PV modules: a global analysis*," Energy **61**, 447-454 (2013).
7. I.M. Peters, F. Ma, **S. Guo**, B. Hoex, B. Blaesi, S. Glunz, A.G. Aberle, J. Luther, "*Advanced modelling of silicon wafer solar cells*," Japanese Journal of Applied Physics **51**, 10NA06 (2012).
8. **S. Guo**, J.P. Singh, M. Peters, A.G. Aberle, J. Wong, "*Two dimensional current flow for stringed PV cells and its influence on the cell-to-module resistive losses*," (under review, Solar Energy).
9. Z. Liu, M. Peters, V. Shanmugam, Y. S. Khoo, **S. Guo**, R. Stangl. A. G. Aberle, J. Wong, "*Luminescence Imaging analysis of light harvesting from inactive area in crystalline silicon PV modules*," Solar Energy Materials and Solar Cells **144**, 523-531 (2015).

Conference papers

1. **S. Guo**, C. Wu, M. Danner, A. Nobre, A.G. Aberle, M. Peters, "*Modelling of an Integrated Standalone PV System*," 42th IEEE Photovoltaic Specialists Conference (New Orleans, USA, 2015).
2. **S. Guo**, A.G. Aberle, M. Peters, "*Investigating local inhomogeneity effects of silicon solar cells by circuit modelling*," 2012 Photovoltaic Asia Pacific Conference, Singapore (Energy Procedia, 2013).
3. L. Fei, **S. Guo**, T.M. Walsh and A.G. Aberle, "*Improved PV module performance under partial shading conditions*," 2012 Photovoltaic Asia Pacific Conference, Singapore (Energy Procedia, 2013).

4. M. Peters, F. Ma, C. Ke, **S. Guo**, N. Sahraei, B. Hoex, A.G. Aberle, "*Advanced Solar Cell Modelling*," 2012 Photovoltaic Asia Pacific Conference, Singapore (Energy Procedia, 2013)
5. **S. Guo**, T.M. Walsh, A.G. Aberle, M. Peters, "*Analysing partial shading of PV modules by circuit modelling*," 38th IEEE Photovoltaic Specialists Conference (Austin, USA, 2012).
6. **S. Guo**, F. Ma, B. Hoex, A.G. Aberle, M. Peters, "*Analysing solar cells by circuit modelling*," 2011 Photovoltaic Asia Pacific Conference, Singapore (Energy Procedia, 2012).
7. M. Peters, F. Ma, **S. Guo**, N. Sahraei, T. Walsh, B. Hoex, A.G. Aberle, B. Bläsi, S. Glunz, "*Advanced modelling of silicon wafer solar cells*," 27th European Photovoltaic Solar Energy Conference and Exhibition (Frankfurt, Germany, 2012).

Bibliography

[1] R. M. Swanson, "A vision for crystalline silicon photovoltaics," *Progress in Photovoltaics: Research and Applications*, vol. 14, pp. 443-453, 2006.

[2] N. Solarbuzz. *Multicrystalline silicon modules to dominate solar PV industry in 2014*. Available: http://www.solarbuzz.com/news/recent-findings/multicrystalline-silicon-modules-dominate-solar-pv-industry-2014, (2015).

[3] *Silicon*. Available: http://en.wikipedia.org/wiki/Silicon, (2015).

[4] M. A. Green, "Silicon solar-cells - evolution, high-efficiency design and efficiency enhancements," *Semiconductor Science and Technology*, vol. 8, pp. 1-12, 1993.

[5] M. A. Green, K. Emery, Y. Hishikawa, W. Warta, and E. D. Dunlop, "Solar cell efficiency tables (version 39)," *Progress in Photovoltaics: Research and Applications*, vol. 20, pp. 12-20, 2013.

[6] M. A. Green, K. Emery, Y. Hishikawa, W. Warta, and E. D. Dunlop, "Solar cell efficiency tables (Version 45)," *Progress in Photovoltaics: Research and Applications*, vol. 23, pp. 1-9, 2015.

[7] *PVX spot market price index solar PV modules.* Available: http://www.solarserver.com/service/pvx-spot-market-price-index-solar-pv-modules.html, (2015).

[8] D. M. Powell, M. T. Winkler, A. Goodrich, and T. Buonassisi, "Modeling the cost and minimum sustainable price of crystalline silicon photovoltaic manufacturing in the United States," *IEEE Journal of Photovoltaics*, vol. 3, pp. 662-668, 2012.

[9] F. J. Ma, "Advanced numerical modelling and simulation of silicon wafer solar cells," PhD thesis, National University of Singapore, 2013.

[10] M. A. Green, "Silicon photovoltaic modules: A brief history of the first 50 years," Progress in Photovoltaics, vol. 13, pp. 447-455, 2005.

[11] *Mitsubishi Photovoltaic Modules.* Available: http://www.mitsubishielectric.com/bu/solar/pv_modules/pdf/L-175-0-B8719-C.pdf, (2015).

[12] *Trina Solar Sets 21.25% Multicrystalline Cell Efficiency Record.* Available: http://www.pv-tech.org/news/trina-solar-sets-new-21.25-multicrystalline-cell-efficiency-record, (2015).

[13] P. P. T. Söderström, Y. Yao, J. Ufheil, "Smart Wire Technology," Available: http://www.meyerburger.com/fileadmin/user_upload/meyerburger.com/Downloads/Publikationen/Dokumente/WhitePaper_SWCT_140519a.pdf, (2015).

[14] L. Kreinin, N. Bordin, A. Karsenty, A. Drori, D. Grobgeld, and Y. Eisenberg, "PV module power gain due to bifacial design. Preliminary experimental and simulation data," *Proc. 35th IEEE Photovoltaic Specialists Conference*, Hawaii, USA, pp. 002171-002175.

[15] *White Solar Modules: A Revolution for Building Integration.* Available: http://www.csem.ch/site/card.asp?pId=28474#.Vk9GTnarS00, (2015).

[16] H. Wirth, "Crystalline silicon PV module technology," *Advances in Photovoltaics*, Pt. 2, vol. 89, pp. 135-197, 2013.

[17] I. Haedrich, U. Eitner, M. Wiese, and H. Wirth, "Unified methodology for determining CTM ratios: Systematic prediction of module power," *Solar Energy Materials and Solar Cells*, vol. 131, pp. 14-23, 2014.

[18] D. Buemi, *Understanding photovoltaic cell and module level efficiency*. Available: http://davebuemi.com/2011/11/02/understanding-photovoltaic-cell-and-module-level-efficiency/, (2013).

[19] R. Hezel, "Novel applications of bifacial solar cells," *Progress in Photovoltaics: Research and Applications*, vol. 11, pp. 549-556, 2003.
[20] *Mismatch effects*. Available: http://www.pveducation.org/pvcdrom/modules/mismatch-effects, (2015).
[21] M. A. Green, *Solar cells : operating principles, technology, and system applications*. Englewood Cliffs, NJ: Prentice-Hall, 1982.
[22] M. A. Green, *Power to the people : sunlight to electricity using solar cells*. Sydney: University of New South Wales Press, 2000.
[23] M. D. Archer and M. A. Green, *Clean electricity from photovoltaics*, 2nd edition, World Scientific, 2001.
[24] Y. Umeo, "Collecting solar-energy - the principle of the solar-Cell and its prospects towards the 21st-Century," *Denki Kagaku*, vol. 54, pp. 646-652, 1986.
[25] J. Nelson, *The physics of solar cells*. London River Edge, NJ: Imperial College Press ; Distributed by World Scientific Pub. Co., 2003.
[26] P. Würfel and U. Würfel, *Physics of solar cells : from basic principles to advanced concepts*, 2nd, updated and expanded ed. Weinheim: Wiley-VCH, 2009.
[27] P. Würfel, *Physics of solar cells : from principles to new concepts*. Weinheim: Wiley-VCH, 2005.
[28] K. Ken-ichi and M. Hiroyuki, "New two-diode model for detailed analysis of multicrystalline silicon solar cells," *Japanese Journal of Applied Physics*, vol. 44, p. 8314, 2005.
[29] A. N. Celik and N. Acikgoz, "Modelling and experimental verification of the operating current of mono-crystalline photovoltaic modules using four- and five-parameter models," *Applied Energy*, vol. 84, pp. 1-15, 2007.
[30] W. Kim and W. Choi, "A novel parameter extraction method for the one-diode solar cell model," *Solar Energy*, vol. 84, pp. 1008-1019, 2010.
[31] D. S. H. Chan and J. C. H. Phang, "Analytical methods for the extraction of solar-cell single-diode and double-diode model parameters from IV characteristics," *IEEE Transactions on Electron Devices*, vol. 34, pp. 286-293, 1987.
[32] *Series Resistance*. Available: http://www.pveducation.org/pvcdrom/design/series-resistance (2015).
[33] S. A. Correia, J. Lossen, and M. Bähr, "Eliminating shunts from industrial silicon solar cells by spatially resolved analysis,"*Proc. 21st European Photovoltaic Solar Energy Conference*, Dresden, Germany, 2006.
[34] *Solar cells and module diagnostics by infared themography*. Available: http://www.ese.iitb.ac.in/~rajeshgupta/SOLAR_CELLS_and_%20MODULES.html (2015).
[35] B. C. Babu and S. Gurjar, "Novel simplified two-diode model of photovoltaic (PV) module," *IEEE Journal of Photovoltaics*, vol. 4, pp. 1156-1161, Jul 2014.
[36] E. L. Meyer and E. Ernest van Dyk, "The effect of reduced shunt resistance and shading on photovoltaic module performance," *Proc. 31th IEEE Photovoltaic Specialists Conference*, Orlando, USA, pp. 1331-1334, 2005.
[37] T. Yamada, H. Nakamura, T. Sugiura, K. Sakuta, and K. Kurokawa, "Reflection loss analysis by optical modeling of PV module," *Solar Energy Materials and Solar Cells*, vol. 67, pp. 405-413, 2001.
[38] I. M. Peters, Y. S. Khoo, and T. M. Walsh, "Detailed current loss analysis for a PV module made with textured multicrystalline silicon wafer solar cells," *IEEE Journal of Photovoltaics*, vol. 4, pp. 585-593, 2014.
[39] P. J. Sánchez-Illescas, P. Carpena, P. Bernaola-Galván, M. Sidrach-de-Cardona, A. V. Coronado, and J. L. Álvarez, "An analysis of geometrical

shapes for PV module glass encapsulation," *Solar Energy Materials and Solar Cells*, vol. 92, pp. 323-331, 2008.
[40] K. R. McIntosh, G. Lau, J. N. Cotsell, K. Hanton, D. L. Bätzner, F. Bettiol, *et al.*, "Increase in external quantum efficiency of encapsulated silicon solar cells from a luminescent down-shifting layer," *Progress in Photovoltaics: Research and Applications*, vol. 17, pp. 191-197, 2009.
[41] K. R. McIntosh, J. N. Cotsell, J. S. Cumpston, A. W. Norris, N. E. Powell, and B. M. Ketola, "An optical comparison of silicone and EVA encapsulants for conventional silicon PV modules: A ray-tracing study,"*Proc. 34th Photovoltaic Specialists Conference*, Philadelphia, USA, pp. 000544-000549, 2009.
[42] I. M. Peters, Y. S. Khoo, and T. M. Walsh, "Detailed current loss analysis for a PV module made with textured multicrystalline silicon wafer solar cells," *IEEE Journal of Photovoltaics*, vol. 4, pp. 585-593, 2014.
[43] C. Carrero, J. Amador, and S. Arnaltes, "A single procedure for helping PV designers to select silicon PV modules and evaluate the loss resistances," *Renewable Energy*, vol. 32, pp. 2579-2589, 2007.
[44] H. Field and A. M. Gabor, "Cell binning method analysis to minimize mismatch losses and performance variation in Si-based modules,"*Proc. 29 th Photovoltaic Specialists Conference*, New Orleans, Louisiana, pp. 418-421, 2002.
[45] K. Ding, X. G. Bian, H. H. Liu, and T. Peng, "A MATLAB-Simulink-based PV module model and its application under conditions of nonuniform irradiance," *IEEE Transactions on Energy Conversion*, vol. 27, pp. 864-872, 2012.
[46] J. F. Randall and J. Jacot, "Is AM1.5 applicable in practice? Modelling eight photovoltaic materials with respect to light intensity and two spectra," *Renewable Energy*, vol. 28, pp. 1851-1864, 2003.
[47] A. Fantoni, M. Vieira, and R. Martins, "Transport properties in microcrystalline silicon solar cells under AM1.5 illumination analysed by two-dimensional numerical simulation," *Solid-State Electronics*, vol. 43, pp. 1709-1714, 1999.
[48] D. P. Singh and P. S. Basak, "Carrier generation rates in important photovoltaic materials for AM1.5 solar spectrum," *Indian Journal of Pure & Applied Physics*, vol. 30, pp. 295-298, 1992.
[49] R. Santbergen, J. M. Goud, M. Zeman, J. A. M. van Roosmalen, and R. J. C. van Zolingen, "The AM1.5 absorption factor of thin-film solar cells," *Solar Energy Materials and Solar Cells*, vol. 94, pp. 715-723, 2010.
[50] M. L. Wesely and R. C. Lipschutz, "Experimental-study of effects of aerosols on diffuse and direct solar-radiation received during summer near Chicago," *Atmospheric Environment*, vol. 10, pp. 981-987, 1976.
[51] *Direct, Diffuse and Reflected Radiation*. Available: http://www.ftexploring.com/solar-energy/direct-and-diffuse-radiation.html (2015).
[52] M. R. Sharma and R. S. Pal, "Total direct and diffuse solar radiation in tropics," *Solar Energy*, vol. 9, pp. 183-189, 1965.
[53] J. S. Schafer, B. N. Holben, T. F. Eck, M. A. Yamasoe, and P. Artaxo, "Atmospheric effects on insolation in the Brazilian Amazon: Observed modification of solar radiation by clouds and smoke and derived single scattering albedo of fire aerosols," *Journal of Geophysical Research-Atmospheres*, vol. 107, 2002.
[54] L. Liu, M. I. Mishchenkoa, S. Menon, A. Macke, and A. A. Lacis, "The effect of black carbon on scattering and absorption of solar radiation by cloud droplets," *Journal of Quantitative Spectroscopy & Radiative Transfer*, vol. 74, pp. 195-204, 2002.

[55] R. R. Meier, "The scattering rate of solar 834-a radiation by magnetospheric O+ and O++," *Geophysical Research Letters,* vol. 17, pp. 1613-1616, 1990.
[56] I. N. Mel'nikova, P. I. Domnin, and V. F. Radionov, "Determining the optical thickness and single-scattering albedo of a stratiform cloud from reflected and transmitted solar radiation measurements," *Izvestiya Akademii Nauk Fizika Atmosfery I Okeana,* vol. 34, pp. 669-676, 1998.
[57] B. E. Psiloglou, M. Santamouris, and D. N. Asimakopoulos, "On broad-band rayleigh-scattering in the atmosphere for solar-eadiation modeling," *Renewable Energy,* vol. 6, pp. 429-433, 1995.
[58] C. C. Lam, P. T. Leung, and K. Young, "Explicit asymptotic formulas for the positions, widths, and strengths of resonances in Mie scattering," *Journal of the Optical Society of America B,* vol. 9, pp. 1585-1592, 1992.
[59] S. Rehman and M. Mohandes, "Splitting global solar radiation into diffuse and direct normal fractions using artificial neural networks," *Energy Sources Part a-Recovery Utilization and Environmental Effects,* vol. 34, pp. 1326-1336, 2012.
[60] J. C. Lam and D. H. W. Li, "Correlation between global solar radiation and its direct and diffuse components," *Building and Environment,* vol. 31, pp. 527-535, 1996.
[61] W. P. Lowry, "Clear sky, direct and diffuse solar-radiation related to atmospheric turbidity and altitude," *Bulletin of the American Meteorological Society,* vol. 61, pp. 426-426, 1980.
[62] G. Manier and H. Fuchs, "Calculations of direct solar-radiation and diffuse radiation from synoptic weather observations," *Meteorologische Rundschau,* vol. 31, pp. 120-127, 1978.
[63] A. Marki and O. Antonic, "Annual models of monthly mean hourly direct, diffuse, and global solar radiation at ground," *Meteorologische Zeitschrift,* vol. 8, pp. 91-95, 1999.
[64] D. Pisimanis, V. Notaridou, and D. P. Lalas, "Estimating direct, diffuse and global solar-radiation on an arbitrarily inclined plane in greece," *Solar Energy,* vol. 39, pp. 159-172, 1987.
[65] M. H. Safaripour and M. A. Mehrabian, "Predicting the direct, diffuse, and global solar radiation on a horizontal surface and comparing with real data," *Heat and Mass Transfer,* vol. 47, pp. 1537-1551, 2011.
[66] R. D. Sears, R. G. Flocchini, and J. L. Hatfield, "Correlations of total, diffuse and direct solar-radiation with the percentage of possible sunshine for Davis, California," *Solar Energy,* vol. 27, pp. 357-360, 1981.
[67] A. Weiss and J. M. Norman, "Partitioning solar-radiation into direct and diffuse, visible and near-infrared components," *Agricultural and Forest Meteorology,* vol. 34, pp. 205-213, 1985.
[68] M. L. Wesely and R. C. Lipschutz, "Method for estimating hourly averages of siffuse and sirect solar-radiation under a layer of scattered clouds," *Solar Energy,* vol. 18, pp. 467-473, 1976.
[69] J. A. Duffie and W. A. Beckman, *Solar engineering of thermal processes*, 2nd ed. New York: Wiley, 1991.
[70] F. A. Dimas, S. I. Gilani, and M. S. Aris, "Hourly solar radiation estimation from limited meteorological data to complete missing solar radiation data," *Proc. International Conference on Environment Science and Engineering*, Singapore, 2011.
[71] B. Y. H. Liu and R. C. Jordan, "The interrelationship and characteristic distribution of direct, diffuse and total solar radiation," *Solar Energy,* vol. 4, pp. 1-19, 1960.
[72] G. S. Campbell and J. M. Norman, *Introduction to environmental biophysics*, 2nd ed. New York: Springer, 1998.

[73] S. Armstrong and W. G. Hurley, "A new methodology to optimise solar energy extraction under cloudy conditions," *Renewable Energy,* vol. 35, pp. 780-787, 2010.
[74] L. T. Wong and W. K. Chow, "Solar radiation model," *Applied Energy,* vol. 69, pp. 191-224, 2001.
[75] D. T. Reindl, W. A. Beckman, and J. A. Duffie, "Diffuse fraction correlations," *Solar Energy,* vol. 45, pp. 1-7, 1990.
[76] J. F. Orgill and K. G. T. Hollands, "Correlation equation for hourly diffuse radiation on a horizontal surface," *Solar Energy,* vol. 19, pp. 357-359, 1977.
[77] J. Wong, "Griddler: Intelligent computer aided design of complex solar cell metallization patterns," *Proc. 39th IEEE Photovoltaic Specialists Conference*,Tampa, Florida, pp. 0933-0938, 2013.
[78] U. Blieske, T. Doege, P. Gayout, M. Neander, D. Neumann, and A. Prat, "Light-trapping in solar modules using extra-white textured glass," *Proc. 3rd World Conference on Photovoltaic Energy Conversion*, vol.1, pp. 188-191, 2003
[79] R. F. M. Lange, Y. Luo, R. Polo, and J. Zahnd, "The lamination of (multi)crystalline and thin film based photovoltaic modules," *Progress in Photovoltaics: Research and Applications,* vol. 19, pp. 127-133, 2011.
[80] "Measurement principles for terrestrial photovoltaic solar devices with reference spectral irradiance data," vol. IEC-Norm 904-3, ed: IEC Geneva, 1987.
[81] K Emery, D. Dunlavy, H. Field and T. Moriaty., "Photovoltaic spectral responsivity measurements" National Renewable Energy Laboratory1998.
[82] J. S. Hartman and M. A. Lind, "Spectral respnse measurements for solar cells," *Solar Cells,* vol. 7, pp. 147-157, 1983.
[83] J. Y. Ye, S. Guo, T. M. Walsh, Y. Hishikawa, and R. A. Stangl, "On the spectral response of PV modules," *Measurement Science & Technology,* vol. 25, 2014.
[84] Y. Tsuno, Y. Hishikawa, and K. Kurokawa, "A method for spectral response measurements of various PV modules," *Proc. 23rd European Photovoltaic Solar Energy Conference*, Valencia, Spain, pp. 2723 - 2727, 2008.
[85] Y. Hishikawa, Y. Tsuno, and K. Kurokawa, "Spectral response measurements of PV modules and Multi-junction devices," *Proc. 22nd European Photovoltaic Solar Energy Conference*, Milan, Italy, pp. 2765-2769, 2007.
[86] H. Field, "Solar cell spectral response measurement errors related to spectral band width and chopped light waveform," *Proc. 26th IEEE Photovoltaic Specialists Conference*, Anaheim, California, 1997.
[87] K. Emery, D. Dunlavy, H. Field, and T. Moriarty, "Photovoltaic spectral responsivity measurements," *Proc. 2nd World Conference and Exhibition on Photovoltaic Solar Energy Conversion*, Vienna, Austria, pp. 1-5, 1998.
[88] S. Guo, F.-J. Ma, B. Hoex, A. G. Aberle, and M. Peters, "Analysing solar cells by circuit modelling," *Energy Procedia,* vol. 25, pp. 28-33, 2012.
[89] D. Grote, "Analyses of silicon solar cells and their measurement methods by distributed, circuit simulations and by experiment," PhD thesis, University of Konstanz, Germany, 2010.
[90] A. Zekry and A. Y. Al-Mazroo, "A distributed SPICE-model of a solar cell," *IEEE Transactions on Electron Devices,* vol. 43, pp. 691-700, 1996.
[91] T. Ikegami, T. Maezono, F. Nakanishi, Y. Yamagata, and K. Ebihara, "Estimation of equivalent circuit parameters of PV module and its application to optimal operation of PV system," *Solar Energy Materials and Solar Cells,* vol. 67, pp. 389-395, 2001.
[92] B. Marion, "A method for modeling the current-voltage curve of a PV module for outdoor conditions," *Progress in Photovoltaics,* vol. 10, pp. 205-214, 2002.

[93] J. Rosell and M. Ibanez, "Modelling power output in photovoltaic modules for outdoor operating conditions," *Energy Conversion and Management,* vol. 47, pp. 2424-2430, 2006.
[94] A. Mermoud and T. Lejeune, "Partial shading on PV arrays: by-pass diode benefits analysis,"*Proc. 25th European Photovoltaic Solar Energy Conference*, Valenica, Spain, 2010, pp. 4654-4658.
[95] H. Patel and V. Agarwal, "MATLAB-based modeling to study the effects of partial shading on PV array characteristics," *IEEE Transactions on Energy Conversion,* vol. 23, pp. 302-310, 2008.
[96] L. S. IV, ed: Linear Technology Corp. , 2011.
[97] S. Silvestre, A. Boronat, and A. Chouder, "Study of bypass diodes configuration on PV modules," *Applied Energy,* vol. 86, pp. 1632-1640, 2009.
[98] L. Castaner and S. Silvestre, *Modelling photovoltaic systems using PSpice*. John Wiley & Sons, Ltd., 2002.
[99] A. Zekry and A. Y. AlMazroo, "A distributed SPICE-model of a solar cell," *IEEETransactions on Electron Devices,* vol. 43, pp. 691-700,1996.
[100] T. M. MATLAB and Statistics Toolbox Release 2012b, Inc., Natick, Massachusetts, United States.
[101] P. J. Sanchez-Illescas, P. Carpena, P. Bernaola-Galván, M. P. Rocha, J. E. C. Rubio, M. Sidrach-de-Cardona, *et al.*, "Performance of photovoltaic modules with white reflective back sheets"*Proc. 23rd European Photovoltaic Solar Energy Conference and Exhibition*, Valencia, Spain, 2008, pp. 346 - 349.
[102] W.-S. Su, Y.-C. Chen, W.-H. Liao, C.-H. Huang, D.-C. Liu, M.-Y. Huang, *et al.*, "Optimization of the output power by effect of backsheet reflectance and spacing between cell strings,"*Proc. 37th IEEE Photovoltaic Specialists Conference*, Seattle, USA, 2011, pp. 3218–3220.
[103] K. R. McIntosh, R. M. Swanson, and J. E. Cotter, "A simple ray tracer to compute the optical concentration of photovoltaic modules," *Progress in Photovoltaics,* vol. 14, pp. 167-177, 2006.
[104] B. Max and E. Wolf, *Principles of optics: electromagnetic theory of propagation, interference and diffraction of light*: CUP Archive, 1999.
[105] Y. K. Chieng and M. A. Green, "Computer simulation of enhanced output from bifacial photovoltaic modules," *Progress in Photovoltaics: Research and Applications*, vol. 1, pp. 293-299, 1993.
[106] R. Dong, "Optimizing reflection and orientation for bifacial photovoltaic modules," The Ohio State University, 2009.
[107] H. Zhong, G. H. Li, R. S. Tang, and W. L. Dong, "Optical performance of inclined south-north axis three-positions tracked solar panels," *Energy,* vol. 36, pp. 1171-1179, 2011.
[108] Z. M. Li, X. Y. Liu, and R. S. Tang, "Optical performance of inclined south-north single-axis tracked solar panels," *Energy,* vol. 35, pp. 2511-2516, 2010.
[109] N. Martin and J. M. Ruiz, "Annual angular reflection losses in PV modules," *Progress in Photovoltaics,* vol. 13, pp. 75-84, 2005.
[110] Y. Q. Tian, R. J. Davies-Colley, P. Gong, and B. W. Thorrold, "Estimating solar radiation on slopes of arbitrary aspect," *Agricultural and Forest Meteorology,* vol. 109, pp. 67-74, 2001.
[111] N. D. Kumar, C. Mounika, T. Sailaja, and D. Mounika, "Design and reduction of wattage losses in solar module using AR coating, cell-to-cell gap and thickness," *Proc. 3rd International Conference on* in *Electronics Computer Technology*, pp. 42-47,2011.
[112] E. E. van Dyk and E. L. Meyer, "Analysis of the effect of parasitic resistances on the performance of photovoltaic modules," *Renewable Energy,* vol. 29, pp. 333-344, 2004.

[113] L. J. Caballero, P. Sanchez-Friera, B. Lalaguna, J. Alonso, Va, x, *et al.*, "Series resistance modelling of industrial screen-printed monocrystalline silicon solar cells and modules including the effect of spot soldering," *Proc. IEEE 4th World Conference on Photovoltaic Energy Conversion*, Waiskoloa, USA, pp. 1388-1391.

[114] S. M. Dasari, P. Srivastav, R. Shaw, S. Saravanan, and P. Suratkar, "Optimization of cell to module conversion loss by reducing the resistive losses," *Renewable Energy*, vol. 50, pp. 82-85, 2013.

[115] S. Guo, J. P. Singh, I. M. Peters, A. G. Aberle, and T. M. Walsh, "A quantitative analysis of photovoltaic modules using halved cells," *International Journal of Photoenergy*, vol. 2013, p. 8, 2013.

[116] H. Ingrid, W. Harry, S. Michael, and K. Gerhard, "PV module efficiency analysis and optimization," *Proc. PV Rollout Conference*, Boston, USA, 2011.

[117] J. Muller, D. Hinken, S. Blankemeyer, H. Kohlenberg, U. Sonntag, K. Bothe, *et al.*, "Resistive power loss analysis of PV modules made from halved 15.6×15.6 cm^2 silicon PERC solar cells with efficiencies up to 20.0%," *Photovoltaics, IEEE Journal of*, vol. 5, pp. 1-7, 2014.

[118] J. H. Wohlgemuth, R. F. Clark, J. P. Posbic, J. M. Zahler, M. Gleaton, D. E. Carlson, *et al.*, "Reaching grid parity using bp solar crystalline silicon technology," *Proc. 34th IEEE Photovoltaic Specialists Conference*, Philadelphia, USA, pp. 001361-001366, 2009.

[119] S. Guo, J. Schneider, F. Lu, H. Hanifi, M. Turek, M. Dyrba, *et al.*, "Investigation of the short-circuit current increase for PV modules using halved silicon wafer solar cells," *Solar Energy Materials and Solar Cells*, vol. 133, pp. 240-247, 2015.

[120] S. Krauter and P. Grunow, "Optical modelling and simulation of PV module encapsulation to improve structure and material properties for maximum energy yield,"*Proc. IEEE 4th World Conference on Photovoltaic Energy Conversion*, Waikoloa, USA, vols 1 and 2, pp. 2133-2137, 2006.

[121] P. Grunow and S. Krauter, "Modelling of the encapsulation factors for photovoltaic modules,"*Proc. IEEE 4th World Conference on Photovoltaic Energy Conversion*, Waikoloa, USA , vols 1 and 2, pp. 2152-2155, 2006.

[122] M. B. Koentopp, M. Schutze, D. Buss, and R. Seguin, "Optimized module design: A study of encapsulation losses and the influence of design parameters on module performance,"*Proc. 38th IEEE Photovoltaic Specialists Conference*, Austin,USA, pp. 3178-3182, 2012.

[123] M. B. Koentopp, M. Schutze, D. Buss, and R. Seguin, "Optimized module design: A study of encapsulation losses and the influence of design parameters on module performance," *IEEE Journal of Photovoltaics*, vol. 3, pp. 138-142, 2013.

[124] K. R. McIntosh, J. N. Cotsell, J. S. Cumpston, A. W. Norris, N. E. Powell, and B. M. Ketola, "An optical comparison of silicone and EVA encapsulants for conventional silicon PV modules: A ray-tracing study,"*Proc. 34th IEEE Photovoltaic Specialists Conference*, Philadelphia, USA, Vols 1-3, pp. 1649-1654, 2009.

[125] F. L. Pedrotti and L. S. Pedrotti, *Introduction to optics*, 2nd ed. Englewood Cliffs, N.J.: Prentice Hall, 1993.

[126] M. Rinio, H. J. Moller, and M. Werner, "LBIC investigations of the lifetime degradation by extended defects in multicrystalline solar silicon," *Solid State Phenomena*, vol. 63-4, pp. 115-122, 1998.

[127] J. Carstensen, G. Popkirov, J. Bahr, and H. Foll, "CELLO: an advanced LBIC measurement technique for solar cell local characterization," *Solar Energy Materials and Solar Cells*, vol. 76, pp. 599-611, 2003.

[128] P. Vorasayan, T. R. Betts, and R. Gottschalg, "Spatially distributed model for the analysis of laser beam induced current (LBIC) measurements of thin film silicon solar modules," *Solar Energy Materials and Solar Cells*, vol. 95, pp. 111-114, 2011.
[129] P. Vorasayan, T. R. Betts, A. N. Tiwari, and R. Gottschag, "Multi-laser LBIC system for thin film PV module characterisation," *Solar Energy Materials and Solar Cells*, vol. 93, pp. 917-921, 2009.
[130] A. W. Blakers, "Shading losses of solar-cell metal grids," *Journal of Applied Physics*, vol. 71, pp. 5237-5241, 1992.
[131] H. Patel and V. Agarwal, "MATLAB-based modeling to study the effects of partial shading on PV array characteristics," *IEEE Transactions on Energy Conversion*, vol. 23, pp. 302-310, 2008.
[132] E. C. Kern, E. M. Gulachenski, and G. A. Kern, "Cloud effects on distributed photovoltaic generation: slow transients at the Gardner, Massachusetts photovoltaic experiment," *IEEE Transactions on Energy Conversion*, vol. 4, pp. 184-190, 1989.
[133] L. Narvarte and E. Lorenzo, "Tracking and ground cover ratio," *Progress in Photovoltaics: Research and Applications*, vol. 16, pp. 703-714, 2008.
[134] T. Hiyama, "Neural network based estimation of maximum power generation from PV module using environmental information - Discussion," *IEEE Transactions on Energy Conversion*, vol. 12, pp. 247-247, 1997.
[135] T. H. Jung, J. W. Ko, G. H. Kang, and H. K. Ahn, "Output characteristics of PV module considering partially reverse biased conditions," *Solar Energy*, vol. 92, pp. 214-220, 2013.
[136] H. Kawamura, K. Naka, N. Yonekura, S. Yamanaka, H. Kawamura, H. Ohno, *et al.*, "Simulation of I-V characteristics of a PV module with shaded PV cells," *Solar Energy Materials and Solar Cells*, vol. 75, pp. 613-621, 2003.
[137] H. Kawamura, K. Naka, N. Yonekura, S. Yamanaka, H. Kawamura, H. Ohno, *et al.*, "Simulation of I–V characteristics of a PV module with shaded PV cells," *Solar Energy Materials and Solar Cells*, vol. 75, pp. 613-621, 2003.
[138] A. Mermoud and T. Lejeune, "Partial shading on PV arrays: by-pass diode benefits analysis," *Proc. 25th European Photovoltaic Solar Energy Conference*, Valencia, Spain, pp. 4654-4658, 2010.
[139] S. Silvestre, A. Boronat, and A. Chouder, "Study of bypass diodes configuration on PV modules," *Applied Energy*, vol. 86, pp. 1632-1640, 2009.
[140] M. Culligan and J. Botkin, "Impact of tilt angle on system economics for area constrained rooftops," 2007.
[141] C. N. F. R. R. Measurements, "Solar Energy Resource Data,". Available: http://rredc.nrel.gov/solar/new_data/confrrm/, 2015.
[142] Deutsche Gesellschaft für Sonnenenergie., *Planning and installing photovoltaic systems : a guide for installers, architects and engineers*, 2nd ed. London ; Sterling, VA: Earthscan, 2008.
[143] J. Metzdorf, "Calibration of solar cells. 1: The differential spectral responsivity method," *Applied Optics*, vol. 26, 1987.
[144] S. Winter, T. Wittchen, and J. Metzdorf, "Primary reference cell calibration at the PTB absed on an improved DSR facility," *Proc. 16th European Photovoltaic Solar Energy Conference*, Glasgow, Scotland, 2000.
[145] J. Hohl-Ebinger, G. Siefer, and W. Warta, "Non-linearity of solar cells in spectral response measurements," *Proc. 22nd European Photovoltaic Solar Energy Conference*, Milan, Italy, 2007.
[146] H. Müllejans, T. Wagner, F. Merli, A. Jäger-Waldau, and E. D. Dunlop, "Changes in spectral response with temperature and irradiance intensity," *Thin Solid Films*, vol. 451-452, pp. 145-151, 2004.

[147] M. Pravettoni, R. Galleano, A. Virtuani, H. Müllejans, and E. D. Dunlop, "Spectral response measurement of double-junction thin-film photovoltaic devices: the impact of shunt resistance and bias voltage," *Measurement Science and Technology*, vol. 22, p. 045902, 2011.
[148] J. Burdick and T. Glatfelter, "Spectral response and I–V measurements of tandem amorphous-silicon alloy solar cells," *Solar Cells*, vol. 18, pp. 301-314, 1986.
[149] J. M. Pearce, "Expanding photovoltaic penetration with residential distributed generation from hybrid solar photovoltaic and combined heat and power systems," *Energy*, vol. 34, pp. 1947-1954, 2009.
[150] *Spectral characterisation of photovoltaic devices*. Available: http://www.bentham.co.uk/pdf/PV_Technical_Note.pdf, (2014).
[151] D. A. Clugston and P. A. Basore, "PC1D version 5: 32-bit solar cell modeling on personal computers,"*Proc. 29th IEEE Photovoltaic Specialists Conference*, New Orleans, Louisiana, pp. 207-210, 1997.
[152] A. N. Celik, "Long-term energy output estimation for photovoltaic energy systems using synthetic solar irradiation data," *Energy*, vol. 28, pp. 479-493, 2003.
[153] E. Koutroulis, D. Kolokotsa, A. Potirakis, and K. Kalaitzakis, "Methodology for optimal sizing of stand-alone photovoltaic/wind-generator systems using genetic algorithms," *Solar Energy*, vol. 80, pp. 1072-1088, 2006.
[154] H. M. S. Hussein, G. E. Ahmad, and H. H. El-Ghetany, "Performance evaluation of photovoltaic modules at different tilt angles and orientations," *Energy Conversion and Management*, vol. 45, pp. 2441-2452, 2004.
[155] M. Kacira, M. Simsek, Y. Babur, and S. Demirkol, "Determining optimum tilt angles and orientations of photovoltaic panels in Sanliurfa, Turkey," *Renewable Energy*, vol. 29, pp. 1265-1275, 2004.
[156] T. Uematsu, K. Tsutsui, Y. Yazawa, T. Warabisako, I. Araki, Y. Eguchi, T, Joge,"Development of bifacial PV cells for new applications of flat-plate modules," *Solar Energy Materials and Solar Cells*, vol. 75, pp. 557-566, 2003.
[157] *Bifi PV workshop*. Available: http://bifipv-workshop.com/index.php?id=bifipv-start, (2015)
[158] G. J. Jorgensen, K. M. Terwilliger, M. D. Kempe, and T. J. McMahon, "Testing of packaging materials for improved PV module reliability," *Proc. 31th IEEE Photovoltaic Specialists Conference*, Orlando, USA, pp. 499-502, 2005.
[159] Y. W. Ok, A. D. Upadhyaya, Y. G. Tao, F. Zimbardi, S. Ning, and A. Rohatgi, "Ion-implanted and screen-printed large area 19.6% efficient N-type bifacial Si solar cell,"*Proc. 38th IEEE Photovoltaic Specialists Conference*, Austin, USA, pp. 2240-2243, 2012.
[160] J. Eguren, J. Delalamo, and A. Luque, "Optimization of P+ doping level of N+-P-P+ bifacial BSF solar-cells by ion-implantation," *Electronics Letters*, vol. 16, pp. 633-634, 1980.
[161] C. Voz, D. Munoz, M. Fonrodona, I. Martin, J. Puigdollers, R. Alcubilla, J. Escarreb, J. Bertomeub, J. Andreub , "Bifacial heterojunction silicon solar cells by hot-wire CVD with open-circuit voltages exceeding 600 mV," *Thin Solid Films*, vol. 511, pp. 415-419, 2006.
[162] L. Zhao, C. L. Zhou, H. L. Li, H. W. Diao, and W. J. Wang, "Design optimization of bifacial HIT solar cells on p-type silicon substrates by simulation," *Solar Energy Materials and Solar Cells*, vol. 92, pp. 673-681, 2008.
[163] T. Joge, Y. Eguchi, Y. Imazu, I. Araki, T. Uematsu, and K. Matsukuma, "Applications and field tests of bifacial solar modules," *Proc. 29th IEEE*

Photovoltaic Specialists Conference, New Orleans, Louisiana, pp. 1549-1552, 2002.

[164] B. Robles-Ocampo, E. Ruiz-Vasquez, H. Canseco-Sanchez, R. C. Cornejo-Meza, G. Trapaga-Martinez, F. J. Garcia-Rodriguez, *et al.*, "Photovoltaic/thermal solar hybrid system with bifacial PV module and transparent plane collector," *Solar Energy Materials and Solar Cells*, vol. 91, pp. 1966-1971, 2007.

[165] T. Joge, Y. Eguchi, Y. Imazu, I. Araki, T. Uematsu, and K. Matsukuma, "Basic application technologies of bifacial photovoltaic solar modules," *Electrical Engineering in Japan*, vol. 149, pp. 32-42, 2004.

[166] T. Nordmann, T. Vontobel, and L. Clavadetscher, "15 years of experience in construction and operation of two bifacial photovoltaic systems on Swiss roads and railways," Bifacial Workshop Konstanz, 2012.

[167] J. Kaldellis and D. Zafirakis, "Experimental investigation of the optimum photovoltaic panels' tilt angle during the summer period," *Energy*, vol. 38, pp. 305-314, 2012.

[168] Y. P. Chang, "Optimal the tilt angles for photovoltaic modules using PSO method with nonlinear time-varying evolution," *Energy*, vol. 35, pp. 1954-1963, May 2010.

[169] T. P. Chang, "Performance evaluation for solar collectors in Taiwan," *Energy*, vol. 34, pp. 32-40, 2009.

[170] K. K. Gopinathan, "Solar-radiation on variously oriented sloping surfaces," *solar energy*, vol. 47, pp. 173-179, 1991.

[171] A. Shariah, M. A. Al-Akhras, and I. A. Al-Omari, "Optimizing the tilt angle of solar collectors," *Renewable Energy*, vol. 26, pp. 587-598, 2002.

[172] H. Gunerhan and A. Hepbasli, "Determination of the optimum tilt angle of solar collectors for building applications," *Building and Environment*, vol. 42, pp. 779-783, Feb 2007.

[173] S. Gonsui, S. Goda, K. Sugibuchi, N. Ishikawa, K. Honda, and H. Zama, "n-type high efficiency bifacial silicon solar cell with theextremely high bifaciality of 96% in average fabricated by using conventional diffusion method," *Proc. 28th European Photovoltaic Solar Energy Conference and Exhibition*, Paris, France, 2013, pp. 718 - 721.

[174] J. P. Singh, S. GUO, I. M. Peters, A. G. Aberle, and T. M. Walsh, "Comparison of glass&glass and glass&backsheet PV Modules using bifacial silicon solar cells," *IEEE Journal of Photovoltaics*, vol. 5, pp. 783-791, 2015.

[175] L. Jianwei, M. Mazzola, J. Gafford, and N. Younan, "A new parameter estimation algorithm for an electrical analogue battery model," *Proc. 27th* IEEE *Applied Power Electronics Conference and Exposition*, pp. 427-433, 2012.

[176] C. Min and G. A. Rincon-Mora, "Accurate electrical battery model capable of predicting runtime and I-V performance," *Energy Conversion, IEEE Transactions on*, vol. 21, pp. 504-511, 2006.

[177] K. Taesic and Q. Wei, "A hybrid battery model capable of capturing dynamic circuit characteristics and nonlinear capacity effects," *Energy Conversion, IEEE Transactions on*, vol. 26, pp. 1172-1180, 2011.